Radiation Damage from Heavy Ion Bombardment in High Purity Aluminum

Stephen Keith McLaurin

December 1984

UWFDM-569

Ph.D. thesis.

Radiation Damage from Heavy Ion Bombardment in High Purity Aluminum

Stephen Keith McLaurin

Fusion Technology Institute
University of Wisconsin
1500 Engineering Drive
Madison, WI 53706

http://fti.neep.wisc.edu

December 1984

UWFDM-569

Ph.D. thesis.

RADIATION DAMAGE FROM HEAVY ION BOMBARDMENT IN HIGH PURITY ALUMINUM

by

Stephen Keith McLaurin

A thesis submitted in partial fulfillment of the
requirements for the degree of

DOCTOR OF PHILOSOPHY

(Nuclear Engineering)

at the

UNIVERSITY OF WISCONSIN-MADISON

1984

RADIATION DAMAGE FROM HEAVY ION BOMBARDMENT IN HIGH PURITY ALUMINUM

Stephen Keith McLaurin

Under the supervision of Professor Gerald L. Kulcinski

Aluminum is used as a structural material in research reactors and experimental facilities for high energy physics. The most abundant of all metals, aluminum has many potential applications in energy technology even with aluminum's low strength and low temperature properties. The objective of this thesis is to demonstrate the effect of injected copper ions on aluminum and the effect inert helium gas has on the nucleation of voids in aluminum. Irradiations of aluminum were performed with copper ions, and aluminum with helium, were bombarded with aluminum ions. Copper is a common alloying material in aluminum and heavy ion beams from copper are readily available. The use of helium as an inert gas was chosen by the common production of helium in aluminum by n,(α) reactions and the chemical reactivity of aluminum for other gases. The results of these irradiations with and without helium are compared to other related studies with heavy ions and neutron irradiations.

The irradiations were performed in the University of Wisconsin Heavy Ion Facility using a temperature controller and sample holder designed to minimize the effects of ion beam heating. This facility produces an intense source of damage energy useful for simulating energetic particle environments for comparison with neutron produced damage.

Well annealed samples of high purity aluminum containing 0.1, 1.0, 10 at.ppm of helium and without helium were bombarded with copper ions and aluminum ions to doses between 0.2 dpa to greater than 20 dpa at temperatures ranging from 25C to 200C. The displacement rates were 5×10^{-4} to 1×10^{-3} dpa/sec.

Copper ion irradiations produced θ precipitation at the ion end of range and heterogeneous concentrations of vacancy loops. Self ion bombardments produced lower concentrations of microstructural defects and essentially all observed loops were vacancy. When helium was preinjected by a radioactive alpha source, ion bombardment produced voids. No voids were ever observed in helium free ion bombarded aluminum samples after doses of more than 20 dpa. The temperature effect on void formation followed theoretical trends of decreasing the void density with increasing temperature and increasing the void size with increasing temperature. A depression of void formation at 100°C was observed and voids formed at temperatures greater than 100°C were truncated and occasionally supervoids were observed. There was no indication of an incubation dose for void formation in aluminum. A comparison with neutron produced data showed the same production level of void swelling in high purity aluminum which is one third the comparable swelling rate in stainless steels.

APPROVED:

Date

Professor Gerald L. Kulcinski
Nuclear Engineering Department

TABLE OF CONTENTS

Faith is a fine invention

For gentlemen who see;

But microscopes are prudent

In an emergency!

- Emily Dickinson

ACKNOWLEDGEMENTS

A decade of friendships was forged in the time span of this study and a few of them are mentioned here. Foremost was the enduring support and encouragement from my thesis advisor, Jerry Kulcinski.

Professors Art Dodd, Bill Wolfer and Peter Wilkes whose teaching, guidance and helpful discussions made understanding as important as doing. The postdocs whose technical expertise was invaluable as support and teachers of hands on knowledge -- Vernon Smith, Jim Billen, Walter Yang, Ian Saunderson, and Eddy Tjhia. A special thanks is given to Rich Casper for his practical teaching. Those graduate students that blazed the trails, Bill Weber, Randy Lott, Eric Opperman, Max Sherman, John Whitley, Ralph Zee, Bob Knoll, Gus O'Donnell and Hosny Attaya. Those graduate students who are discovering most of the easy things have already been done - Dan Bullen, Bob Sindelar, Kai, Larry Seitzman, Steve Zinkle, Don Plumton, and Dave Plantz.

The encouragement from Mike Rosing and David McCarthy with our common burdens and a belief from my parents that I would finish. My wife Mary Boyle whose support, encouragement, and love made this work a reality.

I am grateful to Beth Brown for preparation of this manuscript and the masterful coordination of all the pieces from an electronic jungle.

This work was supported in part by DOE BES and DMFE. Support to finish was made possible by Eddy Tjhia and Seamus Coyle at National Semiconductor.

CHAPTER 1: INTRODUCTION

A. Origin of the Problem

The study of radiation effects in metals began in the 1950's with the study of point defects at low temperatures. In the 1960's, the phenomenon of embrittlement was discovered and the effect of transmutation impurities on the mechanical properties of structural materials was investigated. The higher neutron energies characteristic of fast reactors were expected to increase the embrittlement problems and gas bubble formation, but the large number of cavities found in the Dounreay Fast Reactor fuel cladding in 1966 exceeded all expectations.(1.1)

Cawthorne and Fulton found the cavities they observed in the cladding were not gas filled bubbles and they postulated that the physical displacement of lattice atoms produced vacant lattice sites which precipitated into cavities. (The term cavity refers to a three-dimensional hollow space in a material including bubbles and voids. A cavity described as a bubble implies an internal pressure from a gas while a void is a cavity containing very little gas.) The associated void induced swelling is sensitive to flux and temperature gradients inside a nuclear reactor core and results in bowing and bending of structural components in the reactor. Such dimensional changes in the reactor components can reduce the life of core components, increase the cost, and decrease the performance of a reactor system. A major research effort has been in progress to find or develop a metal alloy that is resistant to swelling and to understand the fundamental theory of void swelling. There have been many review articles(1.2,1.3) and conferences(1.4-1.19) describing the experimental and theoretical aspects of void swelling.

B. Method of Investigation

One method of investigation is to insert an alloy into a fission test reactor and expose it to a desired level of damage using high energy neutrons. A high flux of energetic neutrons is needed to obtain a damage level equivalent to years of reactor operation. If a high level fluence cannot be obtained in a reasonable time, then other methods of producing damage will have to be used, such as simulation of neutron damage with charged particles. There are two primary advantages to using charged particles to produce damage similar to energetic neutron irradiation: first, is the time reduction for accumulating significant dose levels and second, is the control of experimental parameters important to void formation.

In the present fast reactors and fast neutron test facilities, the time required to accumulate fluences of 1×10^{27} neutrons per meter squared (n/m^2) is three to four years.(1.20) Charged particles, however, can produce the equivalent number of displaced atoms in a matter of hours since the effective displacement rate of ions is 1000 to 10,000 times that of neutrons. In 1969 Nelson and Mazey(1.21) demonstrated that heavy ion bombardment could greatly reduce the time required to produce damage levels of interest to reactor designers. Since then, a multitude of ions at various energies have been used to irradiate numerous metals to form voids.(1.22-1.34) It is difficult to control the irradiation environment in a nuclear reactor where the specimens are subjected to complex thermal histories and irradiation times, while charged particle irradiations are performed in a vacuum system at constant temperature and dose rates.

Although the advantages of charged particle simulation are clear, it has its limitations and a number of questions about its validity as a simulation technique remain to be answered. Questions concerning dose rates, PKA spectrum, gas generation, surface effects, induced swelling stress, and injected impurities or interstitials are significant for charged particle simulation. The problem of sample preparation and its effects on the resulting microstructure is a factor for any transmission electron microscope study regardless of how the experimental sample was irradiated. A brief discussion of each of these areas will provide a perspective for this study.

The most fundamental problem in charged particle simulation is how to compare two experiments where the total number of displaced atoms is the same but the production rate of displaced atoms differs by 1000 to 10,000 times. One theoretical effect of the dose rate problem that has been observed experimentally is the shift of temperature. Measurements of void growth made in charged particle simulations are similar to void growth in neutron irradiations made at a lower temperature. Other problems with charged particle simulation concern the method of correlation of the production of point defects. This correlation should include the effects of primary knock on atom

(PKA) spectra, the atom displacement rate (dpa/sec), and the interaction of cascades. The total number of displaced atoms is an inadequate basis to compare radiation damage studies since there presently is not a satisfactory method to measure the percentage of defects that survive the collision cascade. In electron irradiations, the electron produces individual vacancy-interstitial pairs (Frenkel pairs) and the concept of a cascade does not exist.

The function of transmutation produced gases from (n,p) and (n,alpha) reactions in neutron irradiated metals is recognized as important in the nucleation of voids, and this gas must either be injected before the irradiation or, more desirably, during the irradiation. Several authors(1.22-1.31) have performed studies using preinjected gases while other studies utilizing simultaneous injection of gases are in progress.(1.32) Charged particle simulation allows the controlled introduction of the transmuted impurities to investigate their effects on the metal system of interest.

The choice of the bombarding ion influences the nature of the target material by becoming either an impurity element or, for the case of self ion irradiations, an excess interstitial. The effect of the injection ion species can be limited by examination of the damaged area removed from the zone where the bombarding ions come to rest and far enough away from the surface to avoid surface effects. Macroscopic parameters of tensile strength and ductility are not easily determined in charged particle simulation since the limited range of the energetic ion in solids produces a thin layer of damaged material near the surface. If voids are formed in the thin surface area, significant stress can be developed as the material swells outward with respect to the bulk material of the specimen.(1.34-1.36) The surface of the irradiated material is at most a few micrometers from the region of analysis and a residual effect of the surface may exist as a source of impurities and stress.

The analysis by transmission electron microscopy requires a procedure of surface removal, measurement of the amount removed to fractions of a micrometer and finally, backthinning to the area of interest. The generation of free surfaces near the damage zone influences mobile microstructural defects by providing image forces and the concentration of any residual stress in the material. The concentration of the residual stress can easily exceed the yield stress in the material since the stress is concentrated more than 10,000 times.

Simulation of neutron damage by charged particles is, regardless of its difficulties, a desirable method of producing results for the development of metal alloys and a theoretical understanding of void swelling without the complicating features of neutron transmutation products and handling of radioactive materials. Until the difficulties of charged particle irradiations are resolved, the prediction of quantitative results from charged particle irradiations will probably be viewed with some suspicion.

C. Reason for Studying Aluminum

Aluminum has been chosen for this ion simulation study for a number of reasons. Aluminum is used for core components and core structure in several experimental or test reactors including the High Flux Isotope Reactor (HFIR), Savannah River Reactors (SRL) and the Oak Ridge Research Reactor (ORR). From these reactors and others there is an extensive amount of neutron irradiated data available for analysis and comparison to ion simulation studies.

There have been very few heavy ion irradiations of aluminum to date. The first reported studies are a 400 keV aluminum self ion study by Mazey et al.(1.27) and a 2 MeV aluminum self ion study of pure aluminum by Sundquist.(1.29) These were followed by the work of Engman and Homlqvist(1.30) who irradiated aluminum (containing pre-injected helium) with Al ions and Green(1.31) who irradiated pure aluminum with 600 MeV protons to simulate radiation damage and the production of transmuted hydrogen and helium from spallation reactions. All of these studies found void formation in the Al. A few electron irradiations have been done(1.37-1.47) but more information is needed in the heavy ion simulation area to complement the neutron data.

Aluminum is a possible fusion reactor material in the form of sintered aluminum product (SAP) and alloys of aluminum are suggested to be used in some fusion reactors as proposed.(1.48) The fusion environment will generate significant quantities of hydrogen and helium(1.49) in aluminum and the complex role of these gases is known to be important for influencing material properties. Aluminum is also well known in terms of its physical properties and extensively studied from a theoretical and experimental perspective. One of the notable properties of aluminum is its oxide layer which is believed to be an effective barrier layer to gas contamination and corrosion of TEM foils.

High purity (actually ultra pure) aluminum was chosen for a number of reasons. Previous studies(1.50,1.51) have revealed the onset of void formation at lower fluences in high purity aluminum and other pure metals than in alloys. The high purity of the aluminum allows one to inject controlled amounts of impurities and observe their effect upon a pure metal system. Studies using neutrons for irradiations have to contend with the effects of transmuted impurity products which include known nucleation agents as helium and hydrogen and the role of relatively insoluble silicon which is generated in significant amounts. The results of studying a high purity material may be more readily interpreted and perhaps they possess broader implication than results developed from using a particular alloy.

D. Objectives

The basic theme investigated in this study of high purity aluminum is the nucleation of defect clusters and the experimental factors that influence the nucleation of voids and dislocation loops in pure aluminum metal.

In this study, high purity aluminum samples containing nominal concentrations of 0.1, 1.0, and 10 at.ppm of helium were irradiated by aluminum ions. Samples of aluminum containing no helium were also irradiated by copper ions, aluminum ions, and electrons for comparison to the helium containing samples.

All of the heavy ion irradiations were performed in the University of Wisconsin Heavy Ion Irradiation Facility using 14 MeV copper ions and 10 MeV aluminum ions. The electron irradiations were performed in the University of Wisconsin High Voltage 1 MeV Electron Microscope. The post irradiation analysis was based on microstructural observations in a JEOL 100 B and AEI EM7 transmission electron microscopes.

M. L. Sundquist completed, in 1974, a preliminary study of cavity formation in the same high purity aluminum using 2 MeV aluminum ions and preinjection of helium gas.[1.29] This work in this thesis was an extension of that study to a broader temperature range and higher fluences. The fluence level was increased by a factor of 10 and the energy of the irradiating ion was increased by a factor of 5 to extend the damage zone. Irradiations of high purity aluminum were performed at a temperature of 100°C with doses of 0.2, 0.6, 2.0, 6.0 and 20 dpa and another series irradiated to 2.0 dpa from temperatures of 25°C to 200°C in 25°C increments.

REFERENCES CHAPTER 1

1.1 C. Cawthorne and E.J. Fulton, Nature 216, 575 (1967).

1.2 D.I.R. Norris, Rad. Eff. 14, 1; and Rad. Eff. 15, 1 (1972).

1.3 B.L. Eyre, Conference on Fundamental Aspects of Radiation Damage in Metals, Gatlinburg, Tenn., p. 729 (1975).

1.4 Radiation Damage in Reactor Materials, II, IAEA Symposium Proceedings, Vienna, June 1969, STI-PUB-230 (1969).

1.5 Proceedings of BNES European Conf. on Voids Formed by Irradiation of Reactor Materials, ed. S.F. Pugh, N.H. Loretto, and D.I.R. Norris, Reading, U.K., March 1971.

1.6 Proceedings of the International Conference on Radiation Induced Voids in Metals, ed. J.W. Corbett and L.C. Ianniello, Albany, N.Y., June 1971, CONF-710601 (1972).

1.7 Proceedings of ASTM Conference on Irradiation Effects on Structural Alloys or Nuclear Reactor Applications, Niagara Falls, N.Y., June 1970, ASTM-STP-484 (1971).

1.8 Proceedings of ASTM Conference on Effects of Radiation on Substructural and Mechanical Properties of Metals and Alloys, Los Angeles, Calif., June 1972, ASTM-STP-529 (1973).

1.9 Proceedings of Eighth International ASTM Symposium on the Effects of Radiation on Structural Materials, St. Louis, MO, May 1976.

1.10 Proceedings of 1975 International Conference on Defects and Defect Clusters in BCC Metals and Their Alloys, ed. R.J. Arsenault, Gaithersburg, MD (1973).

1.11 Consultant Symposium on the Physics of Irradiation Produced Voids, ed. R.S. Nelson, Harwell, Oxfordshire, U.K., Sept. 1974, AERE-R7934 (1975).

1.12 Proceedings of the International Conference on Radiation Effects and Tritium Technology for Fusion Reactors, Gatlinburg, Tenn., Oct. 1975, CONF-750989 (1976).

1.13 Proceedings of International Conference on Fundamental Aspects of Radiation Damage in Metals, Gatlinburg, Tenn., Oct. 1975, CONF-751006 (1976).

1.14 Proceedings of Applications of Ion Beams to Metals, ed. by Picraux, Eerllisse, and Vook, Plenum Press, N.Y. (1974).

1.15 Proceedings of the International Conference on Applications of Ion Beams to Materials, 1975, ed. by Carter, Colligan, and Grant, Univ. of Warwick, Sept. 1975, CONF Series No. 28.

1.16 International Conference on Radiation Effects in Breeder Reactor Structural Materials, AIME, Scottsdale, AZ, June 1977.

1.17 Consultant Symposium on the Physics of Irradiation Produced Voids, ed. R. S. Nelson, Harwell, Oxfordshire U.K., Sept. 1974, AERE-R7934 (1975).

1.18 Proceedings of the First Topical Meeting on Fusion Reactor Materials, Miami Beach, Florida, January 1979, J. of Nuclear Materials 69&70.

1.19 Proceedings of Second Topical Meeting on Fusion Reactor Materials, Seattle, Washington, August 1981, J. of Nuclear Materials 103&104, (1981).

1.20 P.R. Huebotter and T. Bumo, International Conference on Radiation Induced Voids in Metals, ed. Corbett and Ianniello, Albany, N.Y., 1971, CONF-710601, p. 84 (1972).

1.21 R.S. Nelson, J.A. Hudson, D.J. Mazey, and J.A. Hudson, J. Nucl. Materials 37, 1 (1970).

1.22 J.S. Arnijo and T. Lauritzen, "Deutron-Generated Void Formation in Austenitic Stainless Steels," Proc. Of the Intl. Conf. on Radiation Induced Voids in Metals, ed. J.W. Corbett and L.C. Ianniello, Albany, N.Y. (1971), CONF-710601.

1.23 D. Kramer, H.R. Brager, G.C. Rhodes and A.G. Pard, "Helium Embrittlement in Type 304 Stainless Steel," J. of Nuc. Mat. 25, 121-131 (1968).

1.24 J.H. Worth, A.E.R.E.-R-5704, 1968.

1.25 K. Farrell, A. Wolfenden and R.T. King, "The Effects of Irradiation Temperature and Preinjected Gases on Voids in Aluminum," Rad. Eff. 8, 107 (1971).

1.26 J.M. Lanore, L. Glowinski, A. Risbet, P. Regnier, J.L. Flament, V. Levy and Y. Adda, "Studies of Void Formation in Pure Metals," Proc. of Intl. Conf. on Fundamental Aspects of Radiation Damage in Metals, Gatlinburg, Tenn., 1975, CONF-751006 (1976).

1.27 D.J. Mazey, S. Francis and J.A. Hudson, "Observation of a Partially-Ordered Void Lattice in Aluminum Irradiated with 400 keV Al Ions," J. of Nuc. Mat. 47, 137-142 (1973).

1.28 W.G. Johnston, J.H. Rosolowski and A.M. Turkalo, "An Experimental Survey of Swelling in Commercial Fe-Cr-Ni Alloys Bombarded with 5 MeV Ni Ions," J. of Nuc. Mat 54, 24-40 (1974).

1.29 M.L. Sundquist, Cavity Formation in Aluminum Irradiated with Aluminum Ions, PhD. Thesis, Univ. of Wisconsin (1974).

1.30 U. Engman and B. Holmquist, "Electron Microscopy Studies of Void Swelling and Annealing of Voids in Aluminum Irradiated with Aluminum Ions," Rad. Eff. 47, 189 (1980).

1.31 W.V. Green, S.L. Green, B.N. Singh, and T. Leffers, "Effects of High Helium Production RAte on Microstructural Evolution in Aluminum During 600 MeV Proton Irradiation. J. Nucl. Mat. 103&104, (1981) 1221.(1.16c).

1.32 S.M. Wolf, W.G. Wolfer, L.K. Mansur and G.R. Odette, "Workshop on Use of Dual-Ion Beams in Basic Radiation Effects Research," DOE Training and Conference Center, Oak Ridge, Tenn., (1978).

1.33 G.L. Kulcinski, J.J. Laidler and D. G. Doran, "Simulation of High Fluence Fast Neutron Damage with Heavy Ion Bombardment," Rad. Effects 7, 195-202 (1971).

1.34 W.G. Johnston, J.H. Rosolowski, A.M. Turkalo and K.D. Challenger, "Surface Observations on Nickel Ion-Bombarded Stainless Steels," Scripta Met. 6, 999 (1972).

1.35 W.G. Johnston, J.H. Rosolowski and A.M. Turkalo, Proc. of ASTM Conf. on Effects of Radiation on Substructure and Mechanical Properties of Metals and Alloys, Los Angeles, Calif. (1972), ASTM-STP-529.

1.36 W.G. Johnston, J.H. Rosolowski, A.M. Turkalo and T. Lauritzen, "A Direct Measurement of Gross Swelling in Nickel-Ion-Bombarded Stainless Steel," J. of Nuc. Mat. 46, 272 (1973).

1.37 A. Wolfenden, Micron 4, 295 (1973).

1.38 H. Fischer, C. Gomez, M. Ruhle, and J. Diehl, "Insitu Electron Irradiation of Aluminum in a 200 KV Electron Microscope," Fundamental Aspects of Radiation Damage in Metals, Vol. II p. 715, CONF-751005-P2 (1975).

1.39 W.J. Yang, R.A. Dodd and G.L. Kulcinski, "Electron Irradiation Damage in High Purity Aluminum," J. of Nuclear Material 64, 157-166 (1977).

1.40 D.J. Mazey, S. Francis, and J.A. Hudson, Op. Cit. (10).

1.41 M.J. Makin, Phil Mag. 18, 637 (1968).

1.42 K. Shiraishi, A. Hishinuma, Y. Katano and T. Tacka, J. Phys. Soc. Japan 30, 295 (1971).

1.43 K. Shiraishi, A. Hishinuma, Y. Katano and T. Tacka, J. Phys. Soc. Japan 32, 114 (1972).

1.44 A. Wolfenden, J. Nucl. Mat. 38, 114 (1971).

1.45 A. Wolfenden, Op. Cit. (56).

1.46 M. Kiritani, N. Yoshida and H. Takata, J. Phys. Soc. Japan 36, 720 (1974).

1.47 J. O. Stiegler and K. Farrell, High Voltage Electron Microscopy, Proceedings of the 3rd International Conference, eds. P.R. Swann, C.J. Humphreys and M.J. Goringe (Academic Press, N.Y., 1974) p. 341.

1.48 International Tokamak Reactor Zero Phase, IAEA, Vienna (1979) p.318, STI/PUB/556.

1.49 G.L. Kulcinski, D.G. Doran and M.A. Abdon, "Comparison of Displacement and Gas Production Rates in Current Fission and Future Fusion Reactors," Special Tech. Publ. 570, A.S.T.M., (1976), pp. 329-351.

1.50 J.L. Brimhall and B. Mastell, "Voids in Neutron Irradiated Face Centered Cubic Metals," J. of Nuc. Mat. 46, 273 (1973).

1.51 J.O. Stiegler, K. Farrell, C.K.H. DuBose and R.T. King, "High Fluence Neutron Irradiation Damage in Reactor Materials," Symp. Proc., Vol. 2, p. 215, IAEA, Vienna 1969 (STI/PUB/230).

CHAPTER 2: REVIEW OF RADIATION DAMAGE IN ALUMINUM

A. Neutron and Quenching Studies

Radiation damage effects in aluminum are visible in the transmission electron microscope (TEM) as individual defect artifacts such as interstitial loops, vacancy loops, voids, gas bubbles, dislocation tangles, and (in neutron irradiated samples) transmuted silicon precipitates. The formation and stability of these defects are determined in part by the homologous temperature of aluminum.

Interstitial and vacancy loops are produced below 0.3 T_m (T_m is the absolute melting point) while voids and dislocation loops are generated between 0.3 T_m and 0.5 T_m and gas bubbles are stable above 0.5 T_m. The defect cluster studies in aluminum have been predominately conducted on neutron irradiated samples and there are significant quenching studies. Some of the early work produced defects by quenching in vacancies which later precipitated into loops and voids. Several of these studies are useful since they employ high purity aluminum and investigate the effects of gases on void formation. Table 2.1 is a list of the important points of some of the quenching studies.

Defect clusters of vacancy and interstitial loops, voids, and transmuted silicon precipitates have been observed in neutron irradiated aluminum. The results of the neutron irradiations are listed in Table 2.2. The fluence given should be integrated with the spectrum (or energy dependence) to reflect the actual dpa (displacements per

TABLE 2.1. SURVEY OF IMPORTANT RESULTS FROM ALUMINUM QUENCHING STUDIES

Defects Observed	Material[a]	Reference
Loops [110] a/2 <110> prismatic and hexagonal	4-9's	2.1
Few loops, mostly helical dislocations	4% Cu	2.2
Loops [110], [100], [111] prismatic	5-9's	2.3
Established annealing stage for loops 150-175°C	4-9's	2.4
Frank sessile loops and impurity effects from dilute Si, Mg, and Cu	Si, Mg, Cu	2.5
Double faulted loops [111] <110> 200 nm diameter loops	6-9's	2.6
90% faulted loops	4-9's	2.7
Double faulted loops	5-9's	2.8
2 to 10 nm diameter voids at 10^{18} to 10^{22} per m^3	5-9's	2.9
Fast quench favors loop over void formation	5-9's	2.10
High temp. quench favors loops over void formation while low temperature quench favors void formation		2.11
Void morphology - octahedrons (111), edges <110>	5-9's	2.12
Hydrogen increases void density		2.13
4 and 3 layer loops up to 400 nm diameter		2.14
Void annealing surface energy σ = 995 to 1385 ergs/cm^2		2.15
Void annealing surface energy σ = 1140 ergs/cm^2		2.16

(a) 4-9's stands for 0.9999 or 99.99% purity.

TABLE 2.2. SURVEY OF NEUTRON IRRADIATED ALUMINUM MICROSTRUCTURAL PARAMETERS

T/T_m	Neutron Fluence n/m^2 > 0.1 MeV	Dpa 4.5 E24 @ 16 EV (Note 1)	Void Pop per $(\text{meter})^3$	Void Dia. nm	Void % $\frac{\Delta V}{V}$	Material(a)	Discussion	Ref.
0.35	3.2 E23	0.07		27		5-9's	Void annealing, no gas	2.17
0.35	1.5 E26	33				1100	Silicon produced	2.18
0.36	1.0 E26	22				8001 CW	Silicon produced	2.18
0.35	1.6 E24	0.36		30		5-9's	Hydrogen in voids	2.19
0.35	3.5 E24	0.78	1.3 E20	40	0.39*			2.20
0.35	3.5 E24	0.78	no voids	----		1100	Loops (I&V)	2.20
0.34	1.5 E26	33		80		1100	Cubic Voids	2.20
0.35	1.0 E23	0.02	no voids	----		1100		2.20
0.35	7.0 E23	0.16	2.2 E18			6-9's	Voids have aspect ratios with 3 at.ppm gas at irradiation start	2.21
0.35	2.5 E24	0.56	1.0 E19	32.5	0.016*	6-9's		2.21
0.35	9.0 E24	2.0	4.0 E19	51.5	0.26*	6-9's		2.21
0.35	2.5 E24	0.56	4.6 E19	32.5	0.074*	0.04% In	Dilute oversized impurity increased the swelling	2.21
0.35	9.0 E24	2.0	1.7 E20	27.5	0.17*	0.04% In		2.21
0.35	2.5 E24	0.56	5.6 E19	22	0.028*	0.1% In		2.21
0.35	9.0 E24	2.0	1.6 E20	38	0.41*	0.1% In		2.21

TABLE 2.2 (continued)

0.35	2.5 E24	0.56	3.6 E18	37	0.009*	0.004% Si	Silicon content at the	2.21
0.35	9.0 E24	2.0	1.6 E19	47	0.078*	0.004% Si	start of the irradiation	2.21
0.35	2.5 E24	0.56	1.0 E18	30	0.001*	0.01% Si	Silicon content increased	2.21
0.35	9.0 E24	2.0	5.8 E18	57	0.05*	0.01% Si	with irradiation of all	2.21
0.35	9.0 E24	2.0	1.8 E18			0.03% Si	samples	2.21
0.35	9.0 E24	2.0	1.0 E18	44	0.004*	0.08% Si	Void swelling suppressed	2.21
0.35	9.0 E24	2.0	no voids	----		0.4% Si	in 0.4% Silicon	2.21
0.43	4.0 E24	0.89	irregular	3000		5-9's	0.3 to 3 micron supervoids	2.22
0.45	4.0 E24	0.89	irregular	3000		5-9's	Aspect ratios very large	2.22
0.36	1.0 E26	22	2.0 E26	21	0.8	8001 CW	30% CW 55 nm max. void dia	2.23
0.36	1.0 E26	22	2.0 E21	15	0.4	8001 CW		2.23
0.35	2.9 E24	0.64	1.1 E20		0.19	6-9's	Reirradiated sample and	2.24
0.35	2.9 E24	0.64	2.6 E20		0.17	6-9's	Conc. of voids 2 times	2.24
0.35	1.5 E23	0.03	1.0 E18	16.1	0.0002*	6-9's	Packan Thesis Dose Scan	2.25
0.35	7.7 E23	0.17	2.1 E19	20.1	0.01	6-9's		2.25
0.35	1.6 E24	0.36	3.8 E19	24.4	0.03	6-9's		2.25
0.35	5.2 E24	1.2	1.1 E20	29.9	0.19	6-9's		2.25
0.35	1.6 E25	36	3.9 E20	32.9	0.86	6-9's		2.25
0.35	1.6 E26	36	5.9 E20	49.5	7.4	6-9's		2.25
0.35	1.3 E24	0.29	1.9 E19	32.3	0.04	6-9's		2.25
0.35	5.3 E24	1.2	1.0 E20	27.9	0.15	6-9's		2.25
0.35	1.4 E27	312					Hetergeneous void conc.	2.26
0.35	1.8 E27	401	5.0 E19	52	0.34	6061 T6	T6 Heat Treatment	2.27
0.35	1.2 E27	267	5.0 E19	69	0.8	6061 T0	T0 Heat Treatment	2.27
0.35	1.4 E27	312				1100	Silicon Coated Cavities	2.28

TABLE 2.2 (continued)

0.35	2.2 E26	49	2.6 E19	48	0.14*	1100	ORR core component	2.29
0.35	3.2 E26	71	4.7 E19	55	0.37*	1100	ORR core component tray	2.29
0.36	2.8 E26	62	1.0 E19	20	0.01	6061	HFIR Target Sleeve	2.30
0.36	6.0 E26	133	1.4 E20	31	0.24	6061	Mg_2Si Precipitate stable	2.30
0.36	9.2 E26	205	1.9 E20	37	0.68	6061	throughout irradiation	2.30
0.36	3.2 E23	0.07	very few	27		5-9's	Hetergeneous Void Dist.	2.31
0.35	1.5 E26	33			1.5	1100		2.32
0.35	5.0 E24	1.1	2.0 E20	24	0.15	6-9's		2.33
0.53	5.0 E24	1.1	1.0 E19	57	0.1	6-9's		2.33
0.56	5.0 E24	1.1	none	---		6-9's		2.33
0.37	4.5 E24	1.0	2.0 E20	24	0.15	6-9's	Dislocation Loops	2.33
0.37	4.5 E24	1.0	1.6 E20	20	0.06	4-9's	Dislocation Loops	2.33
0.37	4.5 E24	1.0	none	---		3-9's		2.33
0.33	2 E23	0.045	3 E18	---	----	Ultra	Homogeneous Distribution	2.40
0.33	8 E23	0.18	2.5 E19	29.5	0.03			2.40
0.33	2.4 E24	0.53	7.8 E19	30.5	0.11	pure	of Voids. (Risbet	2.40
0.33	8 E24	1.8	1.5 E20	35.5	0.41			2.40
0.33	2.0 E25	4.3	2.1 E20	45.0	1.2	0.4 at.ppm	Thesis fluence scan.)	2.40
0.33	3.1 E25	6.9	2.4 E20	50.1	1.9			2.40

Notes: * for calculated value using $V = (d^3)*SQRT(2)/3$.

T_m conversion to °C by (T_m x 990°K) - 273°K or see Fig. 4.19.

1) The conversion of fast neutron fluences to dpa used 4.5×10^{24} n/m^2 for fluence and a displacement energy of 16 eV to produce 1 dpa.

atom) value but the fluence can be used as an overall measure of the level of the damage in aluminum where the fast fluence is given for neutron energies greater than 0.1 MeV. A conversion factor of 3 dpa for 10^{25} neutrons/m^2 was calculated for aluminum from the ratio displacement energies of aluminum and stainless steels and the fluence to dpa conversion factor for stainless steel. A more accurate integrated conversion factor for HFIR of 4.5×10^{24} n/m^2,(2.26) was used to convert the fluence values in Table 2.2 to dpa.

The thermal flux present in all neutron irradiated aluminum is important since thermal neutrons produce silicon from $^{27}Al(n,\gamma)^{28}Al$ which β decays to silicon by $^{28}Al \rightarrow {}^{28}Si + \beta$. Silicon at the beginning of an irradiation influences the end result and in high concentrations, (e.g., 0.4%), silicon completely supresses void formation. Silicon also migrates to voids as shown by Farrell(2.28) and coats the surface of the void. Wolfer(2.34) has shown the effect of void coatings on growth rates and cavity nucleation. The low solubilty of silicon does not establish a significant solute concentration gradient around the void but the silicon coating of the void could alter the emission and capture of vacancies and interstitials. The production of other impurities in aluminum is also sensitive to the fast neutron flux, the most important being hydrogen and helium generated from (n,p) and (n,α) reactions.

Neutron irradiated aluminum sometimes displays heterogeneous void populations and elongated void shapes,(2.22) although the void distributions are generally more homogeneous as the fluence level is increased. The elongated voids are believed to be the result of impurities modifying the void surface energy so that void growth is encouraged at one end of the void. The void continues to drag impurities into the end as it grows and the bias to form a supervoid continues. A bias driven supervoid growth depends on the differential concentration gradient and not an absolute concentration level to provide the driving force for elongation.(2.22)

Voids have been observed in aluminum at neutron fluences from 1.0×10^{23} n/m^2 to 2.0×10^{27} n/m^2 and at temperatures ranging from 0.35 T_m to 0.5 T_m. A variety of aluminum alloys have been irradiated and examined. Commercial purity aluminum (1100) and high purity aluminum reveal the greatest amount of swelling with the higher purity material exhibiting more swelling thatn the lower purity material. Aluminum alloys 6061 and 8001 exhibit much lower swelling values at 0.35 T_m with less than 1% swelling at damage levels greater than 250 dpa.

The analysis of gases generated in aluminum by (n,α) and (n,p) reactions is difficult. Helium can be measured by extraction from melting the sample but attempts to measure the hydrogen generated have proved to be very difficult. Particular problems of hydrogen extraction are the absorption of hydrogen on surfaces and the binding of hydrogen by transmuted silicon and other impurities. The dislocation structures in aluminum are also not well characterized. In the samples with a heterogenous void population, the dislocation structure was also heterogenous. Finally, dislocation loops of both vacancy and interstitial types have been observed in neutron irradiated aluminum.(1.48)

B. Charged Particle Studies

The number of charged particle irradiations which have been conducted relative to the number of neutron irradiations of aluminum is small. There have been two heavy ion irradiations of aluminum before this study was initiated and one heavy ion irradiation of aluminum reported during this study. The first heavy ion irradiation of aluminum was by Mazey et al.(1.40) reported void formation in helium preinjected aluminum irradiated with aluminum ions. M.L. Sundquist(1.29) found aluminum irradiated with aluminum ions needed small amounts of helium gas to form voids. Several α particle and electron irradiations of aluminum have been performed.

Alpha particles were used to irradiate aluminum to produce defect clusters in the early 1960's. The defect clusters observed were dislocation loops at the end of range of the α particle. Annealing the irradiated samples produced small gas bubbles of helium.(2.36,2.37) A later study by Ruedl et al. of α particle irradiated aluminum observed the behavior of helium bubbles in aluminum.(2.38)

A number of investigations of electron displacement damage in aluminum in a high voltage electron microscope have been reported.(1.41-1.47) The results of these HVEM irradiations are not consistent. Shiraishi(1.42,1.43) found defect clusters in aluminum formed and then disappeared as a result of electron irradiation at

0.32 T_m while Wolfenden(1.37) and Kiritani(1.46) observed faulted loops in aluminum following irradiation at 0.35 T_m and 0.36 T_m, respectively. Stigler and Farrell(1.47) demonstrated the upper temperature for loop formation during electron irradiation depended on the impurities in the irradiated aluminum. Impurities were found to reduce the cut off temperature for loop formation considerably. Shiraishi(1.42,1.43) found vacancy loops at temperatures less than 0.32 T_m but the work by Kiritani(1.46) indicated that the loops formed in electron irradiated 99.999% aluminum were predominately interstitial type. Rao(2.39) analyzed the perfect loops in aluminum after irradiation at 20°C with 650 keV electrons and found 42% of the loops were vacancy and 58% were interstitial. Fischer(1.38) reported defect clusters from 0.16 T_m to 0.54 T_m but above 0.3 T_m the defects were situated in layers near the foil surfaces as the result of a highly mobile divacancy. Yang(1.39) observed multilayered defect structures of both vacancy and interstitial types and some faulted loops in 99.9999% (6-9's) aluminum. Wolfenden(1.37) irradiated aluminum preinjected with hydrogen and found that annealing after the hydrogen preinjection was necessary to form loops during electron irradiation. In all of the electron irradiations of aluminum, an occasional cavity was observed but the total numbers were not significant.

The heavy ion irradiations of aluminum by Mazey(1.40) reported a partially ordered void lattice after preinjection with helium. The bombarding ion was 400 keV Al^+ at 0.35 T_m and 0.37 T_m. The helium content was 100 at.ppm and a void concentration of $3.0 \times 10^{22}/m^3$ was observed. Sundquist(1.29) irradiated 6-9's aluminum with 1.5 MeV Al^+ ions and obtained a variety of defect structures depending on temperature and preirradiation treatment. Sundquist found a small amount of helium could initiate void swelling while in samples containing no preinjected helium only loops were observed up to doses of 3 dpa. Swelling occurred in preinjected material with helium concentrations ranging from 0.1 to 10 at.ppm over a temperature range of 0.3 T_m to 0.45 T_m.

Another aluminum ion bombardment study by Engman and Holmquist(1.30) employed 3.4 MeV aluminum ions to bombard high purity aluminum to fluences of 3 to 16 dpa (E_d 25 eV) at 0.42 T_m (140°C). Helium preinjection to 130 at.ppm at 630 keV was performed at room temperature and the helium was deposited uniformly from 1.3 to 2.3 micrometers below the sample surface by rocking the target. The aluminum ion damage was also uniformly dispersed by rocking the target in the same manner as for helium preinjection. Engman and Holmquist found the void number density decreased with increasing ion dose from 5×10^{20} m^{-3} to 3×10^{20} m^{-3} while the diameter increased with ion fluence from 25 nm to 45 nm. The total swelling increased with ion fluence from 0.5% at 3 dpa to 1.6% at 16 dpa.

REFERENCES FOR CHAPTER 2

2.1 P.B. Hirsch, J. Silcox, R.E. Smallman and K.H. Westmacott, Phil. Mag. 3, 897 (1958).

2.2 G. Thomas and M.J. Whelan, Phil. Mag. 4, 511 (1959).

2.3 D. Kuhlmann-Wilsdorf and H.G.F. Wilsdorf, J. of Appl. Phys. 31, 516 (1960).

2.4 R. Vandervoort and J. Washburn, Phil. Mag. 5, 24 (1960).

2.5 K. H. Westmacott, R. S. Barnes, D. Hull and R. E. Smallman, Phil. Mag. 6, (1961), p. 929.

2.6 S. Yoshida, Y. Shimomura and M. Kiritani, J. Phys. Soc. of Japan 17, 1196 (1962).

2.7 S. Yoshida, M. Kiritani and Y. Shimomura, J. Phys. Soc. Japan 18, 175 (1963).

2.8 S. Yoshida and Y. Shimomura, J. Phys. Soc. of Japan 18, 1590 (1963).

2.9 M. Kiritani and S. Yoshida, J. Phys. Soc. of Japan 18, 915 (1963).

2.10 R.M.J. Cotterill and R.L. Segall, Phil. Mag. 8, 1105 (1963).

2.11 M. Kiritani, J. Phys. Soc. of Japan 19, 618 (1964).

2.12 M. Kiritani, Y. Shimomura and S. Yoshida, J. Phys. Soc. of Japan 19, 1624 (1964).

2.13 M. Kiritani, A. Sato, Y. Shimomura and S. Yoshida, 6th Intl. Cong. for TEM, Kyolo (1966), p. 341.

2.14 J.W. Edington and D.R. West, Phil. Mag. 14, 603 (1966).

2.15 T.E. Volin and R.W. Ballaffi, Phys. Stat. Sol. 25, 163 (1968).

2.16 K.H. Westmacott, R.E. Smallman and P.S. Dobson, Metals Sci. J. 2, 177 (1968).

2.17 J.L. Brimhall and B. Mastell, "The Annealing of Radiation Produced Voids in Aluminum," 27th Annual EMSA Meeting.

2.18 K. Farrell, J.O. Stiegler and R.E. Gehlbach, "Transmutation-Produced Precipitates in Irradiated Aluminum", Metallography 3, 275 (1970).

2.19 K.H. Westmacott and R. E. Smallman, "The Formation Stability and Defect on Yield Stress of Cavities in Neutron-Irradiated Aluminum," Mat. Sci. and Engr. 5, 325-333 (1969/1970).

2.20 J.O. Stiegler et. al., Op. Cit. Ref. 19.

2.21 R.M. Mayer and E.T. Morris, "Neutron Irradiation of Dilute Aluminum Alloys," J. of Nuc. Mat. 71, 36-43 (1977).

2.22 K. Farrell and R.T. King, "Supervoids in Irradiated Aluminum," Phys. Status Solidi (a) 2, (1970): K(5).

2.23 R.T. King, E.L. Long, Jr., J.O. Stiegler and K. Farrell, "High Fluence Damage in an Aluminum Alloy," J. Nucl. Mat. 35, 231 (1970).

2.24 N.H. Packan, "Voids in Re-Irradiated Aluminum," J. Nucl. Mat. 37, 251 (1970).

2.25 N.H. Packan, "Fluence and Flux Dependence of Void Formation in Pure Aluminum," J. Nucl. Mat. 40, 1 (1971).

2.26 K. Farrell and A.E. Richt, "Microstructure and Tensile Properties of Heavily Irradiated 1100-0 Aluminum," 9th ASTM International Symposium on Effects of Radiation on Structural Materials (1978) Richland, Wash.

2.27 K. Farrell and R.T. King, "Tensile Properties of Neutron-Irradiated 6061 Aluminum Alloy in Annealed and Precipitation-Hardened Conditions," 9th ASTM International Symposium on Effects of Radiation on Structural Materials, Richland, Wash. (1978).

2.28 K. Farrell, J. Bently and D.N. Braski, "Direct Observation of Radiation-Induced Coated Cavities," Scripta Met. 11, 243-248 (1977).

2.29 A. Jostsons and E.L. Long, Jr., "Radiation Damage and the Effects of Postirradiation Annealing in 1100 Grade Aluminum," Rad. Effects 16, 83-94 (1972).

2.30 R.T. King, A. Jostsons, and K. Farrell, "Neutron Irradiation Damage in a Precipitation-Hardened Aluminum Alloy," To be published.

2.31 J.L. Brimhall and B. Mastel, Op. cit. (2.17).

2.32 R.T. King and E.L. Long, Jr., J. Metals 20, 116A.

2.33 Y. Adda, "Report on the CEA Program of Investigations of Radiation-Induced Cavities in Metals: Presentation of Some Results," Proceedings of the International Conference on Radiation Induced Voids in Metals, ed. by J.W. Corbett and L.C. Ianniello, Albany, N.Y. (1971), CONF-710601, p. 31.

2.34 W.G. Wolfer, L.K. Mansur, and J.A. Sprague, "Theory of Swelling and Irradiation Creep" in International Conference : Radiation Effects in Breeder Reactor Structural Materials, TMS-AIME (1977) p.851.

2.35 T. Muroga, K. Fukuya, H. Kawanishi, and S. Ishino, "Direct Comparison of Electron and Self-Ion Damages in Aluminum as a Fusion Neutron Simulation Study", 2nd Topical Conference on Fusion Reactor Materials, J. of Nucl. Mat. 101&102, (1981).

2.36 R.S. Barnes and D.J. Mazey, Phil. Mag. 5, 1247 (1960).

2.37 D.J. Mazey and R.S. Barnes, "On Interstitial Dislocation Loops in Aluminum Bombarded with Alpha Particles," Phil. Mag. 7, 1861 (1962).

2.38 E. Ruedl, O. Gautsch, and E. Staroste, "On the Behaviour of Very Small He-Bubbles in d-Bombarded Aluminum," Rad Effects 15, 275-6 (1972).

2.39 P. Rao, Report #1750, The Materials Science Center, Cornell University, Ithaca, N.Y. (1972).

2.40 A. Riobet, Etude De La Formation Des Cavities Dans L'Aluminum Pur Et Faiblement Allie Irradie Aux Neutrons Rapides, Ph.D. Thesis, A L'Universite De Paris-Sud Centor D'Orsay (1974).

CHAPTER 3: RADIATION DAMAGE THEORY

Radiation damage as defined in this study is the production of point defects from energetic bombarding charged particles. The incident particle interacts elastically with lattice atoms producing vacancies, and primary knock on atoms (PKA's). In addition, the incident particle and PKA can interact inelastically with the sea of electrons producing heat. The incident particle and PKA slow down as they lose energy and the trail of collision events is described as a collision cascade or a mass collection of point defects and subcascades from PKAs produced from the incident particle. Point defects from the residue of cascades can move and interact with other point defects (vacancies, interstitials, impurities) and other microstructural features (dislocations, cavities, grain boundaries, precipitates, and surfaces). The host material evolves from its initial state into a collection of microstructures by first nucleating small microstructural defects and second, by causing these microstructural defects to grow by continuous absorption of point defects. The macroscopic response of a material to the nucleation and growth of cavities is swelling or the dimensional growth of the material with a corresponding reduction in its density. Other changes in the material typically include the loss of ductility, loss of corrosion resistance, and increasing electrical resistance. In general, radiation damage alters the material from its pristine state to a degraded material containing various point defect sinks.

A. Point Defect Production

Point defects in a crystalline metal lattice are of two general types: (1) impurity atoms and (2) Frenkel pairs (vacancy or interstitial). Neutron irradiation produces both types of point defects while ion simulation produces the Frenkel defects and, depending upon the bombarding ion, can also produce a limited zone of injected impurity atoms. The generation of impurity atoms by neutron is predictable with a knowledge of the neutron spectrum and the corresponding cross sections. Frenkel defects are transient events unless they can be immobilized at very low temperatures or cluster together into a stable formations. The final damage state depends on the initial Frenkel pair production level and the total number of atoms displaced per atom site (displacements per atom or dpa). The dpa unit of radiation damage is the average number of times a lattice atom is forced from its lattice site to an interstitial position creating a Frenkel pair. The definition of displaced atoms does not include the replaced atoms in a collision line sequence but only the last atom that is forced into an interstitial position. The dpa is the unit of radiation damage that compares charged particle irradiations with neutron irradiations for atomic interactions but the effects of transmuted impurities is not accounted for in the dpa damage estimate. The damage level is calculated along the path of the slowing atom by a modified Kinchen and Pease model developed by Torrens and Robinson.(3.2) The displacements are given according to the equation

$$R_d = \frac{J}{N} \kappa \frac{S_D(x)}{2E_d} \qquad (3.1)$$

where J is the fluence of particles and N is the target atomic density. κ is a binary collision parameter describing the efficiency of energy exchange between the lattice atom (e.g., 80%)(3.2) and the energetic particle. The energy to produce a frenkel pair, E_d, is the effective displacement energy for aluminum (16 eV) (E_d REF) averaged over all lattice directions. $S_D(x)$ is the energy deposited in elastic nuclear collisions per unit path length as a function of the path length x.

The rate of displacement production is given by(3.1)

$$(R_d)_x = N \int_{E_d/\Lambda}^{\infty} \phi(E)\, dE \int_{E_d}^{\Lambda E} \sigma(E,T)\nu(T)\, dT \qquad (3.2)$$

where $\phi(E)$ is an arbitrary flux of irradiation particles, N is the atom number density, $\sigma(E,T)$ is the differential cross section for a bombarding particle of energy E to transfer energy T to a recoil atom, $\nu(T)$ is the number of displacements created by the recoiling atom of energy T, and Λ is the expression

$$\Lambda = \frac{4\, M_1 M_2}{(M_1 + M_2)^2} \qquad (3.3)$$

where M_1 and M_2 are the masses of the incident particle and the target particle respectively. $\phi(E)$, $\sigma(E,T)$ and $\nu(T)$ are the key parameters in determining the displacement rate. The factor E for ions requires knowledge of the energy distribution as a function of the penetration depth into the solid. Once $\phi(E,x)$ is known, the differential cross section $\sigma(E,T)$ and the damage function $\nu(T)$ are integrated over the minimum and maximum energy transfers that will cause displacements to obtain the relative probability that an atom will be displaced per atom per unit of energy.

Equation 3.2 can be solved by a Monte Carlo approach or an analytical solution of the distribution equations for energy deposition and resulting displacements. The Monte Carlo approach is very dependent upon the type of interatomic potential chosen for solving the binary collisions between the atoms and requires a large number of collision evaluations plus the additional disadvantage of having a very limited number of interatomic potentials to work with. The analytical approach is more applicable to many problems hand has been developed by several different authors.(3.2-3.13)

Lindhard, Scharff and Schiott(3.4) developed an energy partition model to evaluate the slowing down of atoms by an analytical approach (LSS Theory). LSS describe the energy loss mechanism as two separable parts of electronic stopping power and nuclear stopping power. LSS use the Thomas-Fermi model of the atom for the generation of the collision cross sections. The differential cross section from the Thomas-Fermi model is(3.3)

$$d\sigma = \pi a^2 \frac{dt}{2t^{3/2}} f(t^{1/2}) \qquad (3.4)$$

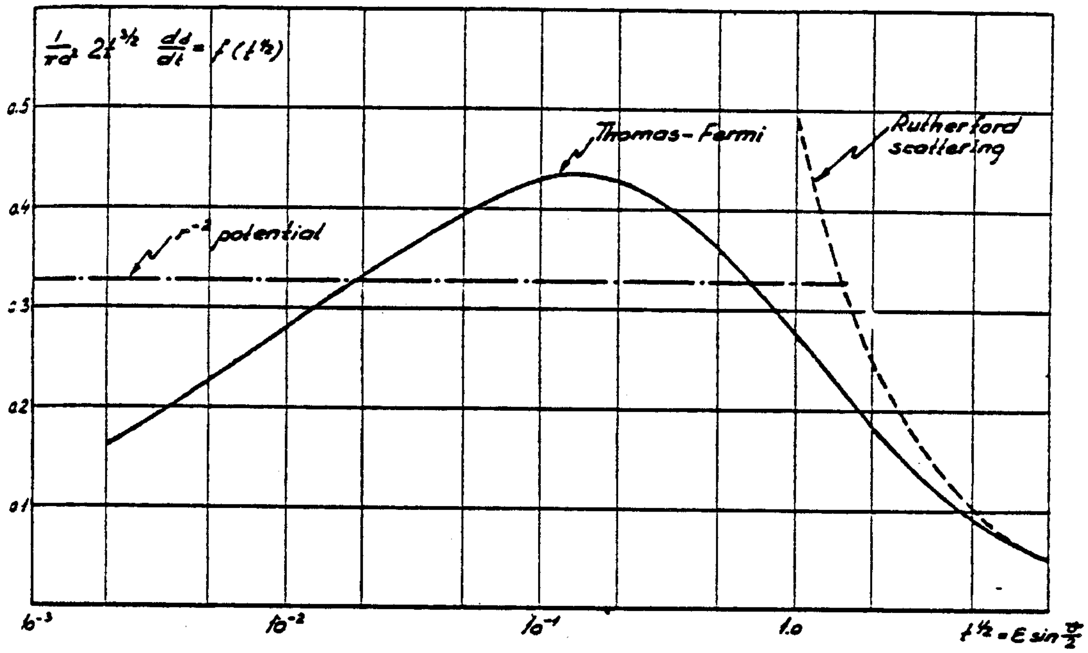

Fig. 3.1. The Thomas-Fermi differential scattering cross section for elastic nuclear collisons joins smoothly with the Rutherford scattering at high values of $t^{1/2}$. The inverse square cross section is also shown. (From Ref. 3.3.)

where a is a screening parameter and

$$t^{1/2} = \varepsilon \sin(\theta/2) \tag{3.5}$$

LSS use ε as a reduced energy parameter and θ is the center of mass scattering angle. LSS numerically calculated $f(t^{1/2})$ for a Thomas-Fermi potential as shown in Fig. 3.1.

The total stopping cross section is separated by LSS into a nuclear stopping cross section and an electronic stopping cross section. The nuclear stopping power is described by

$$(d\varepsilon/d\rho)_n = \int_0^E dx\, \frac{f(x)}{\varepsilon} \tag{3.6}$$

where $x = t^{1/2}$ and the reduced energy epilson should be greater than 0.01.(3.14) For most heavy ion irradiations, $\varepsilon \gg 0.01$. The electronic stopping is modeled as energy loss being proportional to the ion velocity.(3.5) Interactions are calculated with target electrons as an electron gas the Fermi energy. The electronic stopping power is

$$(d\varepsilon/d\rho)_e = k\varepsilon^{1/2} \tag{3.7}$$

where the upper limit of interaction is

$$E_{lim} < 0.025\ M_1 Z_1^{4/3}\ \text{MeV} \tag{3.8}$$

K is a constant equal to

$$Z_1^{1/6}\ \frac{0.0793\ Z_1^{1/2} Z_2^{1/2}\ (A_1 + A_2)^{3/2}}{(Z_1^{2/3} Z_2^{2/3})^{3/4}\ A_1^{3/2} A_2^{1/2}} \approx 0.1 \text{ to } 0.2 \tag{3.9}$$

For aluminum ions incident on an aluminum target, $k = 0.1419$ with $E_{lim} = 20.6$ MeV. Figure 3.2 shows typical curves for $(d\varepsilon/d\rho)_e$. The

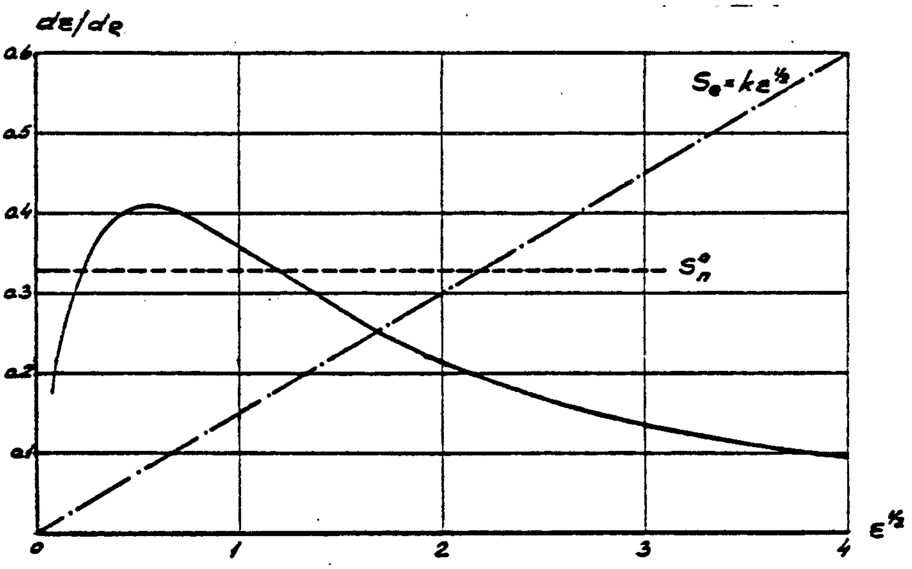

Fig. 3.2. The theoretical nuclear stopping cross section in ρ-ε variables. The abscissa is proportional to the ion velocity or $\varepsilon^{1/2}$. The solid curve is computed from the differential cross section shown in Fig. 3.1 and the dot-dash line is the electronic stopping cross section $k*\varepsilon^{1/2}$ for k = 0.15. (From Ref. 3.3.)

upper limit of validity (E_{lim}) is dependent on the incident ion and not on the target material. Table 3.1 lists both the upper and lower ranges of validity for a number of ions incident on aluminum. The limits can be extended another factor of 10 by using a three-parameter empirical formulation developed by Brice.(3.6) The Brice parameter extends the upper limit for electronic stopping power which is the dominate loss mechanism at high energies. The range of the formula for a 1% to 2% rms error fit to experimental data is 0 to 10 MeV/amu (0 to 270 MeV for aluminum). The ion energy as a function of pathlength can be evaluated by Monte Carlo techniques or LSS analyti-

TABLE 3.1

Energy Limits For Ion Beams On Aluminum From LSS Theory

ION	E_{lower} (MeV)	E_{upper} (MeV)
Hydrogen	0.00106	0.0248
Deuterium	0.00110	0.0496
Helium	0.00245	0.250
Carbon	0.0103	3.24
Nitrogen	0.0129	4.65
Oxygen	0.0157	6.35
Aluminum	0.0345	20.5
Titanium	0.0893	73.4
Vanadium	0.0980	82.7
Nickel	0.137	124.
Copper	0.151	141.
Niobium	0.304	326.
Molybdenum	0.321	348.
Cesium	0.582	690.
Tantalum	1.08	1370.
Gold	1.28	1656.

$$E_{lower} = Z_1 Z_2 (Z_1^{2/3} + Z_2^{2/3})^{1/2} (A_1 + A_2)/A_2 \ (3.07 \times 10^{-5} \text{ MeV})$$

$$E_{upper} = A_1 Z_1^{4/3} \ (2.48 \times 10^{-2} \text{ MeV})$$

cal techniques. Analytical methods have a broader range of applications and is preferred to Monte Carlo calculations. The range of pathlength can be determined simply but the energy deposition is a more difficult problem. The range of a particular atom will have a range straggling given by a gaussian expression

$$f(x) = \frac{1}{\sqrt{2\pi}\alpha_x} \exp\left[- \frac{(x - x_m)^2}{2\alpha_x^2}\right] \tag{3.10}$$

α_x is the equivalent of the rms standard derivation and x_m is the mean projected range. The energy deposition is modeled by applying the gaussian distribution to the ions as they slow down in the material. This gives the energy loss of deposition as a function of position in the material and is used by Manning and Mueller(3.7) and Brice(3.8-3.12) to calculate the damage distribution in a material bombarded by an ion of known energy. The major difference between the two computer codes EDEP and "the Brice code" is that the Brice code extends LSS theory with energy extension by the empirical three parameter formula and additional integral moments describing momentum transport while the Manning and Mueller code (EDEP) does not offer these two refinements. The nuclear energy loss is expressed as

$$S_D(x) = \int_x^{\infty} f(x') \, S_L[E_1(x' - x)] \, \frac{dR(x' - x)}{dx'} \, dx' \tag{3.11}$$

where $E_1(x)$ is the average energy of an ion with projected range x, $S_D(x)$ is the average deposited energy into atomic displacements, R(x) is the total range of the ion, and $S_L(E)$ is the function for the deposited energy.

The partitioning of energy to recoil atoms represented by the equation developed by LSS(3.4)

$$\eta(\varepsilon) = \frac{\varepsilon}{1 + kg(\varepsilon)} \qquad (3.12)$$

which gives the fraction of the PKA energy dissipated into displacements. Robinson(3.2) has fitted a numerical solution for $g(\varepsilon)$ expressed as

$$g(\varepsilon) = \varepsilon + 3.4008\ \varepsilon^{1/6} + 0.40244\ \varepsilon^{3/4}\ . \qquad (3.13)$$

the factor k is the same as given by Eq. 3.9 and epilson is the reduced energy.

The formulation given for the generation of point defects involves the calculation of the bombarding ion energy as a function of penetration distance into the irradiated material. The energy deposited by the bombarding ion can be determined and a fraction of this deposited energy will result in a number of displaced atoms within the irradiated material. The best estimates made for this theory is an error of 20% and several experiments discussed by LSS, Manning and Mueller, and Brice justify the validity of the theoretical predictions. The cross section studies of void formation by Whitely(3.15) and precipitate formation by Knoll(3.16) indicate a greater range for the ions than predicted. The range error found in both of these studies is less than the 20% error limit for LSS theory but their studies suggest that LSS may be underestimating the range of energetic ions.

B. Cascades

The ideal simulation by ion bombardment would have a primary knock on atom (PKA) spectrum that is identical to the one being simulated. A fast breeder reactor simulation needs a fast breeder reactor PKA spectrum while a fusion reactor simulation needs a fusion PKA spectrum. Unfortunately, the ion PKA spectrum is significantly different from both fusion and fission spectra. It is necessary to examine the ion PKA cascade structure and PKA spectrum to determine whether the differences are significant.

Figure 3.3 is a schematic diagram of the general radiation induced defect production process in a metal. Primary radiation particles (PRP) collide directly with constituent atoms of the irradiated material. Atoms directly struck by a PRP are primary knockon atoms. The PRP in a fast reactor or fusion reactor are energetic neutrons while the PRP in ion simulation studies the PRP is an energetic charged particle. Each PKA that receives enough kinetic energy from a PRP to be ejected from its normal lattice site initiates a collision cascade. A collision cascade is a localized dynamic disturbance active for a picosecond producing vacancies and interstitials that remain after the cascade dissipates. A cascade producing two or more displacements is characterized as a displacement spike. The

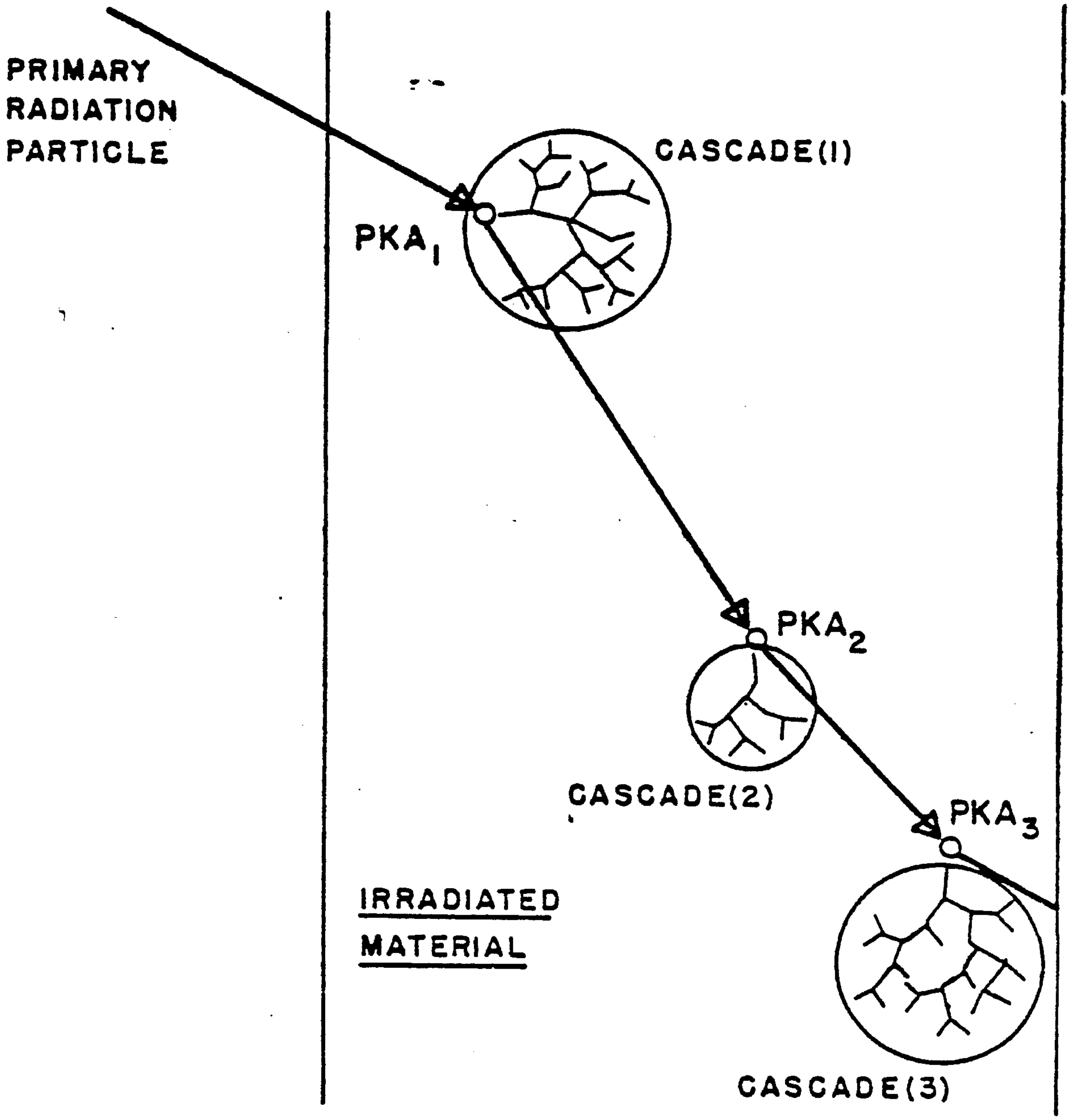

Fig. 3.3. PKA production by a primary radiation particle (PRP) where the PKA production sites are represented by small open circles.

distinction between a Frenkel pair and a thermal spike arises from different stability factors for a single vacancy interstitial pair to those for a collection of Frenkel pairs. This stability difference is dramatically demonstrated by electron irradiation induced damage when compared to neutron or heavy ion irradiations as in Fig. 3.4.

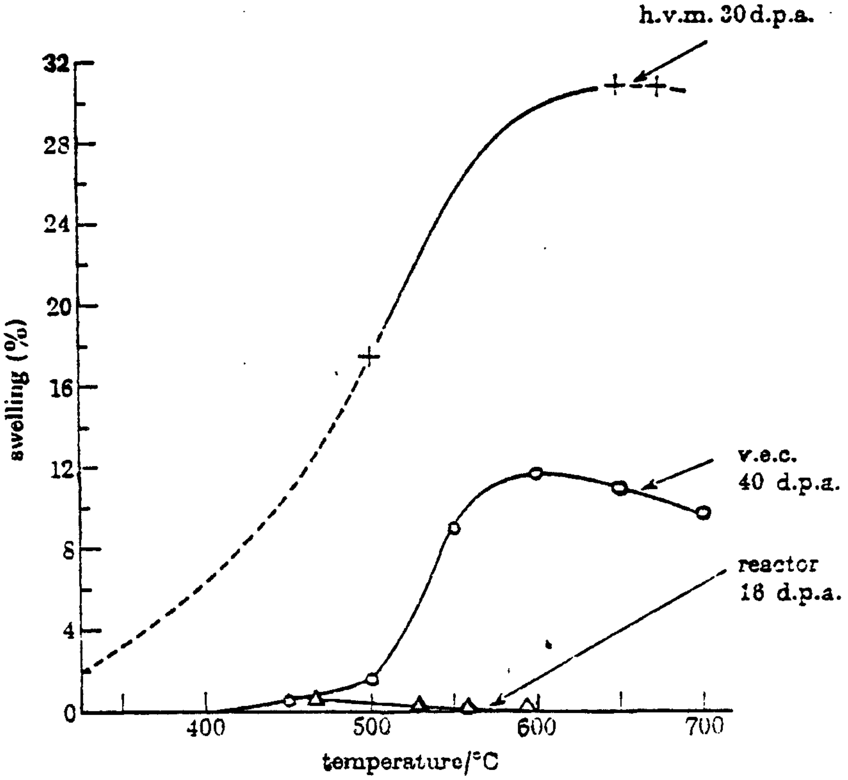

Fig. 3.4. The experimentally measured swelling as a function of irradiation temperature in solution treated M316 steel irradiated with 1 MeV electrons, 22 MeV carbon ions, and fast neutrons. (From Ref. 3.25)

The collision cascade initiated by each PKA is represented schematically by a tree structure. The initiating PRP can be an electron, a neutron, or a heavy ion.(3.1)

Two approaches for evaluating cascade effects are Monte Carlo and analytical techniques as for describing point defect production. Monte Carlo techniques have been used by Beeler(3.17,3.18) and Doran(3.19,3.19a) while analytical methods have been utilized by Marwick(3.20) and Bullough.

Marwick(3.20) examined the effect of PKA mass and energy on the size and distribution of cascades. The amount of data on the size of a cascade as a function of recoil energy is very small. For nickel, Marwick demonstrated that the mean free path between energetic recoil production is larger than the size of the cascades produced by the recoils. This results in little overlap of the adjacent cascades of the same event and little interference of the cascades upon one another as shown in Fig. 3.5. The interaction between a PKA and target atom is a heavily screened coulomb potential. This type of interaction has long range effects that result in large numbers of low energy recoils as shown in Fig. 3.6. As the mass of the bombarding ion increases, the screened coulomb potential is more heavily screened which reduces the number of displacements from low energy recoils and increases the number of displacements for high energy recoils. Figure 3.7 shows the effect of increasing ion mass on the shift toward more energetic recoils. One of the important considerations in ion simulation studies to note that the fraction of damage

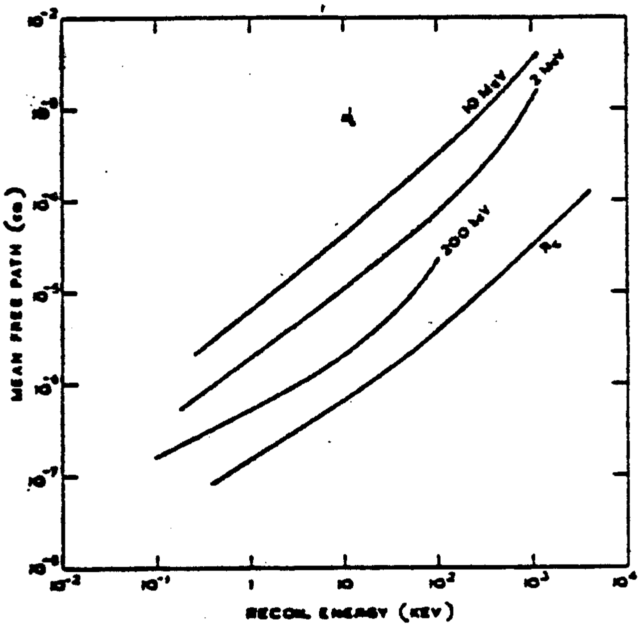

Fig. 3.5. The mean free path for production of energetic recoils as a function or recoil energy for nickel projectiles of three different energies moving in a nickel target. The cascade size is estimated by the curve R_C. (From Ref. 3.20)

due to low energy recoils is much higher than in the corresponding case for neutron irradiations.

Monte Carlo studies for cascades are still limited by the size of computers for adequate simulation descriptions. One of the general trends shown by Beeler(3.18) suggests that increasing the mass of the incident ion is more likely to cause interference of different branches of the cascade. For aluminum on aluminum one can expect even less overlap in the cascade structure than for Marwick's study of nickel on nickel in Fig. 3.5. Aluminum will have a PKA structure

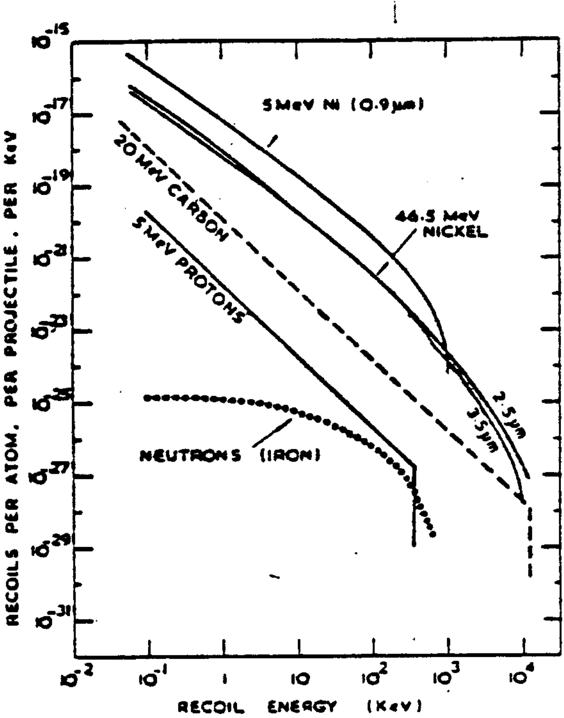

Fig. 3.6. The PKA spectra for various ions in nickel and fast reactor neutrons in iron. For the nickel beams the calculations are for the depths indicated with an ion beam of 46.5 MeV. (From Ref. 3.20.)

that is "wispy" and diffuse with little cascade overlapping and interaction.

Other studies of cascade substructure by Beeler show a large degree of subcascade interaction. Simulated fusion neutron cascades in iron are shown in Figs. 3.8 and 3.9. The interference within the cascade is an area of controversy and experimental evidence reveals a large variation in the degree of interaction. Experimental work by

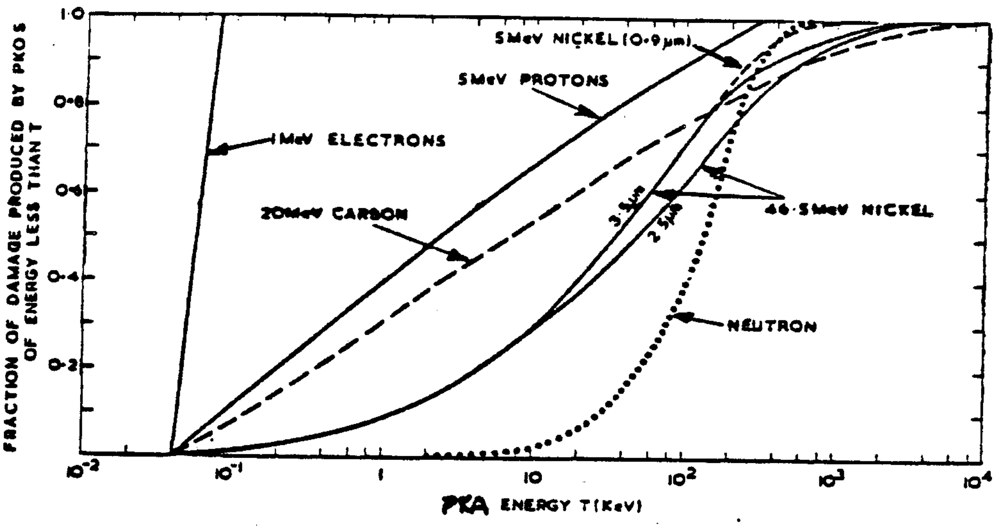

Fig. 3.7 The proportion of the total number of displacements produced by PKA recoils as a function of PKA energies. The low energy recoil damage is higher for ion simulation than for neutron irradiations and the electron irradiations are completely dominated by the low energy recoils. (From Ref. 3.20)

Merkle and Averback(3.21) in silver and gold reveal 40% to 100% survival of vacancies suggesting a very efficient transport of interstitials from the center of the cascade. An upper limit of 25% recombination has been established by computer calculations of Norgett(3.22) who has extended the calculations of Beeler. This value is in general agreement with the earlier experiments of Merkel and Averback. The analytical work of Winterbon, Sigmund, and Sanders(3.23) on cascade models is used by Lyles and Merkle(3.24) to

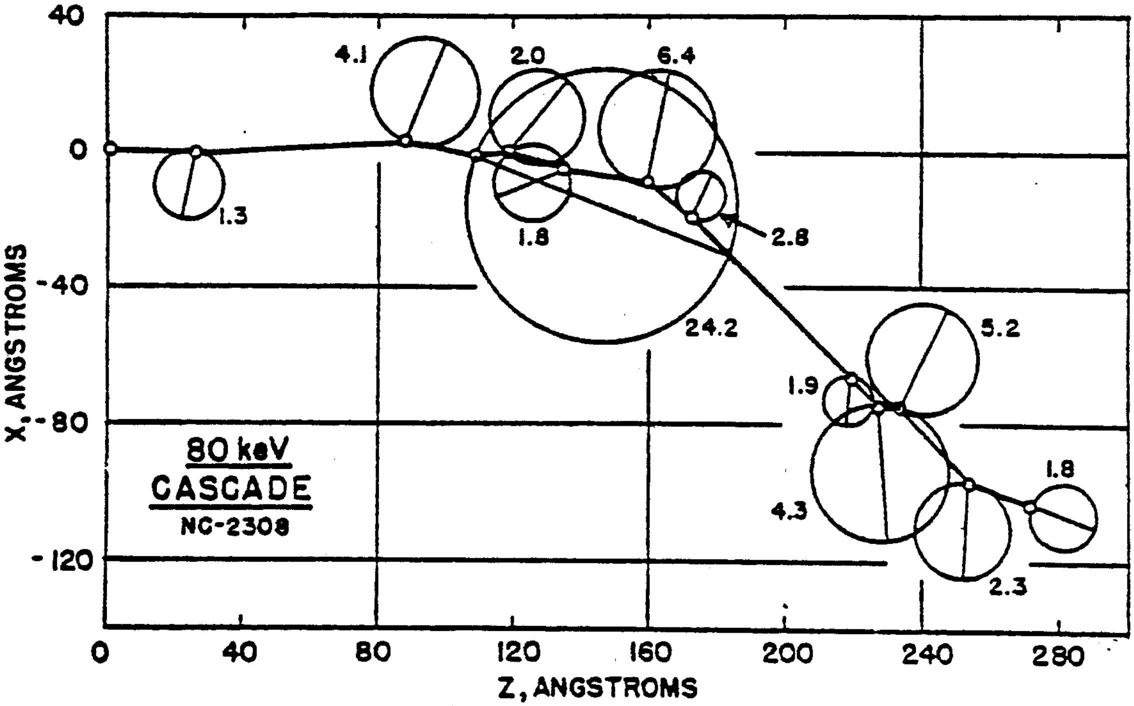

Fig. 3.8. A transverse diagram of an 80 keV cascade in FCC iron from a binary collision model. The path of the PRP is shown and PKA subcascades are indicated by circles. The energy of the PKA is proportional to the diameter of the PKA circle and illustrates the overlapping potential of subcascades. (From Ref. 3.17)

explain the separation of the cascade structures they observed in 14 MeV neutron irradiated silver and gold. The random cascade model$^{(3.23)}$ gives good agreement for the cascade and substructure observed by Lyles and Merkle. The work of Heinisch$^{(3.19a)}$ with cascade simulation has not shown subcascade formation and the defect yields from cascades are proportional to the damage energy. More recent

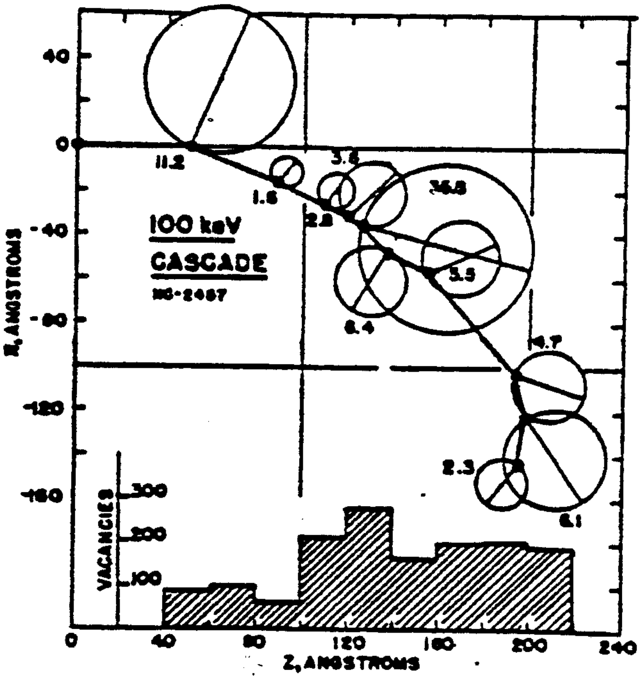

Fig. 3.9. A 100 keV cascade in FCC iron is shown as for 3.8 with the surviving vacancy population indicated by the histogram. (From Ref. 3.17)

investigations of the defect yield or defects that survive the collision cascade are indicating the yield may not be as high as formerly believed.(3.19b)

The rate theory developed by Brailsford and Bullough has also been applied to cascade phenomena. Bullough, Eyre, and Krishan(3.25) (BEK) extended the rate theory to incorporate the effects of cascades upon swelling in irradiated materials. BEK showed that when a number of vacancies from the vacancy rich core of a cascade collapse to form loops, the free vacancy concentration is reduced. This reduced vacancy concentration also reduces the swelling rate. Pulsed ion irradiations(3.26) and calculations by Ghoniem(3.27) have shown the importance of retained vacancies as predicted by BEK. Brailsford also used rate theory to examine the effect of cascades and included the effect of self interstitials as well. Brailsford found that the effect of self interstitials could be as important to rate theory and void growth as the collapse of cascades. The extra interstitials increase the recombination rate and reduces the void swelling rate.

C. Nucleation

The irradiation of metals produces vacancies and self interstitials as discussed in Section A. The interstitials are attracted more strongly to dislocation sinks and have much higher mobilities. As a result of the higher mobilities, the interstitials are absorbed more rapidly at sinks and the remaining vacancies greatly outnumber the interstitials. The growth of a point defect aggregate is controlled by the arrival rate of interstitials and vacancies and not by the respective concentrations of interstitials and vacancies. Typically, the arrival rate of vacancies to a neutral sink such as a void is of the order of a few percent greater than for interstitials. Some of the parameters affecting the arrival rate (displacement probabilities and dislocation bias) are not well known and make quantitative predictions difficult, but the physics of the damage and growth processes are reasonably understood.

A similar understanding for the physics of void nucleation is developing but the fundamental process of aggregation of small clusters of point defects which, by themselves cannot grow into a stable microstructural defect is not well understood. However, the production of voids is understood well enough to formulate the basic parameters that influence nucleation. The functional dependence (temperature, stress, and impurity effects) of each parameter is known and experiments tailored to investigate the behavior of these parameters need to be performed to establish model data for the present theories. Determining the mechanism of void nucleation is of central importance in the understanding and control of void swelling in irradiated metals.

There are several fundamental approaches to the mechanisms by which a void gains supporting constitutents (vacancies, impurities, and gas atoms) and suffers destructive interference (interstitials, vacancy emission, gas resolution, and impurities). As such, there are many possible combinations of constructive and destructive agents for formulation of a theory of nucleation. Several different attempts have been devised and are summarized as follows.

1) Co-precipitation of vacancies and self-interstitials by a matter-antimatter analog.(3.36,3.38)

2) Heterogeneous nucleation on single gas atoms or gas atom clusters.(3.37,3.44)

3) Co-precipitation of vacancies, self-interstitials, and mobile gas atoms.(3.43,3.42,3.39)

4) Direct formation from the vacancy rich core of a cascade.(3.48,3.49)

5) Agglomeration from Brownian motion of embryonic gas containing voids.(3.50)

6) Stress modifications to the arrival rates of vacancies and interstitials as a function of void size and impurity concentration.(3.40,3.41)

Supporting evidence for each of the above concepts exists and all six of these variations describe void nucleation within various constraints. Russell(3.46) has tried to combine most of the above into a general theory that reduces to the simpler cases. A general theory still is lacking where the fundamental parameters of temperature, dose rate, gas concentrations, impurity concentrations, and stress components can be specified and qualitative results can be obtained.

C.1 Computer Simulation of Nucleation

Computer simulation programs(3.29-3.35) developed to study defect production and interaction have been extended to include the behavior of vacancy and interstitial aggregates. Studies(3.28,3.34) with a 1000 atom crystal and a 8000 atom crystal at 0°K in which random Frenkel pairs were created, revealed a saturation in the stable number of defects at 0.17 dpa. There was a maximum deviation of +83% to -38% from the average saturation level and a statistically random fluctuation process could provide the conditions necessary for void embryo nucleation. The number of stable defects is very sensitive to the size of the recombination volume. Two recombination sizes of 27 atoms and 57 atoms were used and the larger recombination volume increased the separation distance between the stable defects. The larger recombination volume produced a lower saturation level but the fluctuation about the average value was still observed.

Another computer simulation method for studying void nucleation involves the creation of large vacancy clusters from displacement spikes and the overlapping of cascades(3.28,3.47) as suggested by Levy(3.48) and Shively(3.49). The defect density in a displacement spike is saturated and overlapping of a saturated defect density displacement spike with another one does not increase the average saturation of defects nor does it change the interstitial or vacancy cluster size distribution (compared to that produced by an isolated cascade). The saturated primary damage state consists of single interstitials, interstitial loops, monovacancies, divacancies, trivacancies, and a region of vacancy clusters. The vacancy cluster region resulting from the displacement spike could provide void embryos that may grow into visible voids.

The vacancy clusters produced by displacement spikes are irregular in shape and rearrangement by diffusion could produce a more stable void nuclei or cause the void to disappear altogether. Short term annealing of displacement spikes by computer simulation provides a method to examine the effects of temperature and diffusion on the formation of void embryos produced by displacement spikes. Doran(3.35) examined displacement spike annealing at 800°K and 300°K in iron with a temperature dependent recombination volume. Doran found the number of void nuclei were reduced when the interstitials were mobile. At 800°K, where both vacancy and interstitials are mobile, the number of large vacancy clusters increases even though the total vacancy population is reduced by a factor of 5 by annihilation events. An even more interesting result was the appearance of new void nuclei from the collection of small vacancy clusters best described as a form of homogeneous nucleation. Present homogeneous nucleation theory describes nucleation by single point defects and not by small vacancy clusters.

C.2 Analytical Void Nucleation Theories

Homogeneous nucleation theory has been developed by Russell,(3.38,3.39) Katz and Weidersich,(3.36,3.37) and Wolfer.(3.40,3.41) The approach used follows the ideas of classical nucleation theory but with some significant differences. One of the major differences is that the condensing defects, interstitial atoms and vacancies, can mutually annihilate each other and are thus similar to matter and antimatter. The theory of nucleation is then developed by considering the effects of the point defect concentrations of vacancies, interstitials, and gas atoms upon a size distribution of void embryos. The void nucleation theories by Katz, Weidersich, and Russell, hearafter referred to as KWR, are very similar. Because of their similarity, the theory notation and basic equations follows that of Katz and Weidersich.(3.43)

The two major restrictions of the theory presented by Weidersich(3.43) are: (1) the embryos are assumed to have a unique shape so that they can be characterized by a single parameter such as x, representing the number of atoms or vacancies comprising the embryo and (2) the embryos are assumed to grow or to shrink by the absorption or emission of single defects only and reactions with multiple point defect clusters such as divacancies are ignored. The first approximation is reasonable, but the second constraint of single vacancy and interstitial additions conflicts with the results of Doran's short term annealing with divacancies and trivacancies.

The net flow rate in size space of embryos of size x to embryos of size x+1 at time t is given by the equation(3.43)

$$J(x,t) = f(x)n(x,t) - b(x + 1)\ n(x+1,t) \tag{3.14}$$

where n(x,t) is the number of embryos of size x at time t, f(x) is the rate constant for the forward reaction and b(x + 1) is the rate constant for the reverse or backward reaction. This equation represents a set of equations that connect the populations n(x,t) of embryos of various x sizes with the fluxes J(x,t) between the sizes. An equilibrium distribution of clusters can be described by a Boltzmann distribution

$$n^{\circ}(x) = N \exp \{-W(x)/kT\} \tag{3.15}$$

where W(x) is the reversible work required to form the embryo of size x. For a spherical embryo the reversible work of formation is given from its surface free energy by

$$W(x) = \sigma 4\pi (3v/4\pi)^{2/3} x^{2/3} \qquad (3.16)$$

where σ is the surface energy and v is the vacancy volume. The rate constants for the forward and backward reactions are evaluated and are strong functions of the vacancy and interstitial saturation level and presence of gas. The forward reaction f(x) in the presence of interstitials is

$$b(x) = [\beta_i + \gamma_v(x)] a(x) \qquad (3.17)$$

where β_i is the condensation rate of interstitials, and $\gamma v(x)$ is the rate of emission of vacancies from an embryo containing x vacancies. Stress effects are incorporated thorough modification of defect emission terms.

The nucleation of dislocation loops is treated in a similar matter and antimatter approach. The differences include expressions for the effective area a(x) and the emission rate of vacancies which are determined from energy expressions appropriate for the type of loop involved. The effect of stress on the work term depends upon the orientation of the dislocation loops with respect to the stress.

The effect of helium, hydrogen, and other gases produced in nuclear reactions play an essential role in the nucleation of voids. The effect of the gas is treated as if it is immobile or mobile. The equilibrium cavity size distribution is modified to

$$n^\circ(x,y) = n^\circ(x^*,y)\ \exp[-W(x,y)/kT] \qquad (3.18)$$

where y represents the number of gas molecules, x^* the most probable size of a bubble, and $n^\circ(x^*,y)$ is the concentration of clusters of x^* vacancies containing y gas molecules. The value of x^* is obtained from the minimization of $W(x,y)$ with regard to x, or equivalently, is the value corresponding to the Gibbs-Thomson relation among the equilibrium pressure, the surface free energy, and the radius of a cavity from $p = 2\ \sigma/r$.

If the element and/or temperature are such that the gas is insoluble in the lattice, one can neglect the effects of thermal emission of molecules from gas vacancy clusters. The arrival rate of interstitial gas atoms is much lower than the arrival rate of vacancies and interstitials and the flow in embryo size space among the clusters containing any given number of gas molecules is essentially undisturbed. The nucleation process is then the sum of independent and parallel nucleation processes, connected only by their competition for interstitials and vacancies. The total rate of nucleation is then the sum of the homogeneous rate plus the rate of nucleation for embryos containing one gas atom, plus the rate of nucleation for embryos containing two gas atoms and so on. The net effect is to construct a number of parallel nucleation paths centered about the most probable cluster size.

An essentially unchanging distribution of helium clusters is a simplification of the effect of mobile gas. A number of mechanisms yield mobile helium during irradiation even when thermal emission of helium atoms from vacancy clusters and vacancies are small. During neutron irradiation, n-α reactions produce helium atoms that come to rest at interstitial sites. Experimental evidence(3.51-3.53) and theoretical calculations(3.54,3.55) indicate that interstitial helium is quite mobile in a number of metals and should migrate rapidly until it is trapped in vacancies, void embryos, or dislocation cores. The displacement process will remobilize trapped helium in addition to displacing the host atoms. The complication that arises in homogeneous nucleation theory is the elimination of the single path assumption. The parallel paths described for the case of immobile gas now become interlinked with the possibility of emitting and absorbing gas atoms as well as interstitials and vacancies.

Qualitatively, there are two effects of the mobile helium. First, it decreases the rate of vacancy emission through the free energy increase necessary to emit vacancies and, second, it blocks void shrinkage below some minimum size required to accommodate the helium atoms. Both effects increase the void nucleation rate and both are controlled by the magnitude of the helium flux.

The equation describing the net flow rate of clusters in size space must be modified for this two-dimensional nucleation problem. Weidersich and Katz(3.43) express the time rate of change of the number of embryos of x_j vacancies and y_j gas molecules as

$$\frac{dn_j}{dt} = \sum_j k_{i\to j}\, n_i - \sum_i k_{j\to i}\, n_j + k_j - l_j \qquad (3.19)$$

where the first sum is extended over all reactions that convert voids of type i to voids of type j. The second sum describes the loss of type j voids by reactions, resulting in type i voids. The term k_j is the rate at which type j voids are produced from cascades and l_j is the removal rate of embryos to other vacancy sinks. This set of equations described by Eq. 3.19 for all j's of interest describe the nucleation and growth of gas containing voids. The solution of this set of nonlinear differential equations is difficult so that the application of steady state is necessary to remove the time dependence of the rate constants and of the concentrations n_j. The rate constants $k_{i \to j}$ are schematically shown in Fig. 3.10 which depicts the flow in cluster space of gas containing void embryos.

Weidersich and Katz solved this system of equations and investigated the effects of vacancy supersaturation, of the arrival rate ratio, and of temperature for nickel with mobile helium. The production rate of vacancies and interstitials in metals are roughly equal and for voids to form and grow there, must be an excess of vacancies. It is customary to use the ratio of the rates of condensation of interstitials β_i to the rate of condensation of vacancies β_v to voids as a parameter, the ratio β_i/β_v, called the arrival rate ratio, is often estimated to be between 0.8 and 1.0 and is closely related to the bias factor arising from the preferential adsorption of interstitials at dislocations.

Nucleation is dominated by vacancy supersaturation and is to a lesser extent is effected by the arrival rate ratio, where the in-

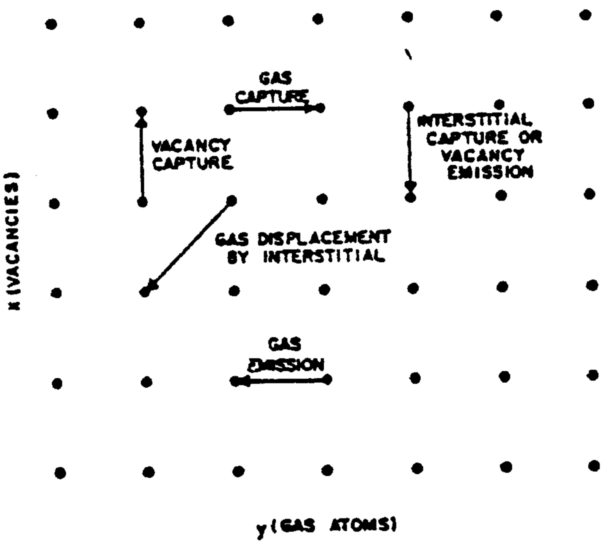

Fig. 3.10. A schematic showing the 2-dimensional flow of clusters in cluster space consisting of X vacancies and Y gas atoms. The various step reactions or flow event paths are labelled.

creasing of the arrival rate ratio requires a higher vacancy supersaturation for the same nucleation rate. As (β_i/β_v) approaches unity increasingly larger vacancy supersaturations are required to obtain a given nucleation rate indicating that dislocations are essential to the nucleation of voids. This effect is explained by the ratio of the backward to forward reaction rate constants and the critical size limit. For a finite nucleation rate, $b(x)/f(x)$ must be smaller than unity for large x or $\beta_i/\beta_v < (1 - 1/S)$ where S is the supersaturation. Russell(3.46) uses the same arrival rate ratio and expresses the nucleation rate following classical nucleation parameters of a

Zeldovich factor(3.38) and an incubation time.(3.56) The Zeldovich factor is expressed as

$$Z = \left[\frac{-1}{2\pi kT} \frac{\partial^2}{\partial n^2} \left(\Delta G(x,y)\right)\right]^{1/2} \qquad (3.20)$$

where the curvature of the pseudo free energy curve near the maximum is approximated as a parabola. The free energy curve is described as

$$\Delta G(x,y) = kT \sum_i \ln \beta_i/\beta_v + \exp\left(\frac{1}{RT} \frac{\partial \Delta G^0(i,x)}{\partial i}\right) \qquad (3.21)$$

The incubation time or delay before the onset of steady state nucleation is given as

$$\tau = \frac{1}{2\, Z^2 \beta_v x^{1/3}} \qquad (3.22)$$

and the impinging vacancy rate ($r\beta_v$) is the same as Katz and Wiedersich arrival rate of vacancies. The theory presented by Russell attempts to simpilfy the flow of void embryos in cluster space by introducing a Poincare model or method(3.46) of dividing the void embryos into two components of x vacancies and y gas atoms (using the Katz and Weidersich notation). Russell illustrates the nucleation barrier (peusdo free energy) as two nodal lines of $\dot{x}$ and $\dot{n}$, both equal to zero, as shown in Fig. 3.11. Unfortunately, the details of intermediate steps in Russell's theory are few and attempts to apply his concepts to experiments are difficult.

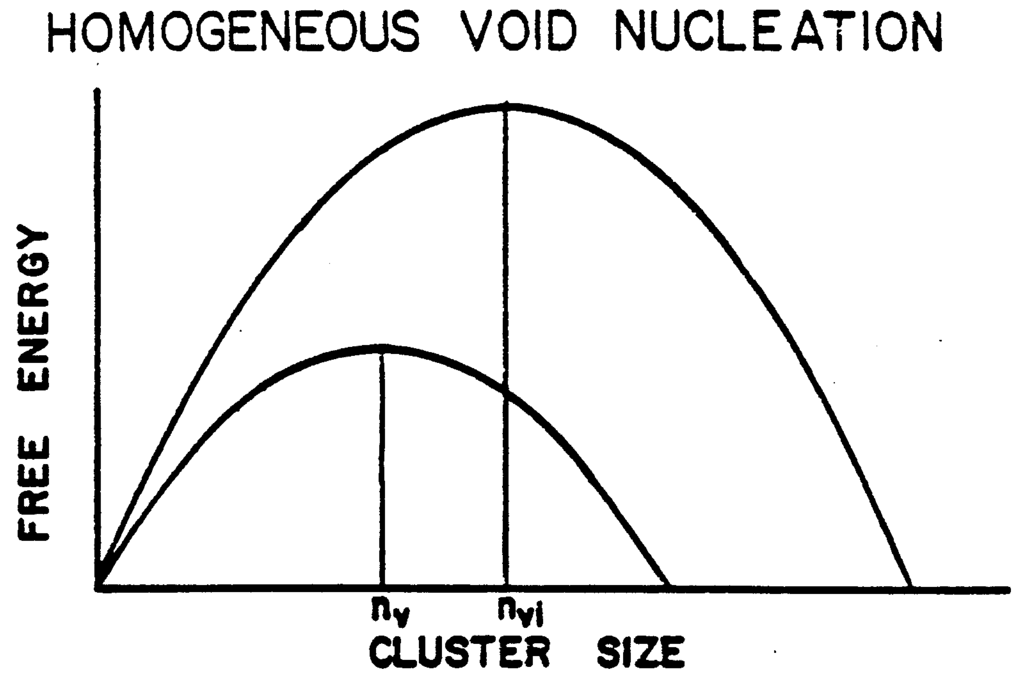
HOMOGENEOUS VOID NUCLEATION

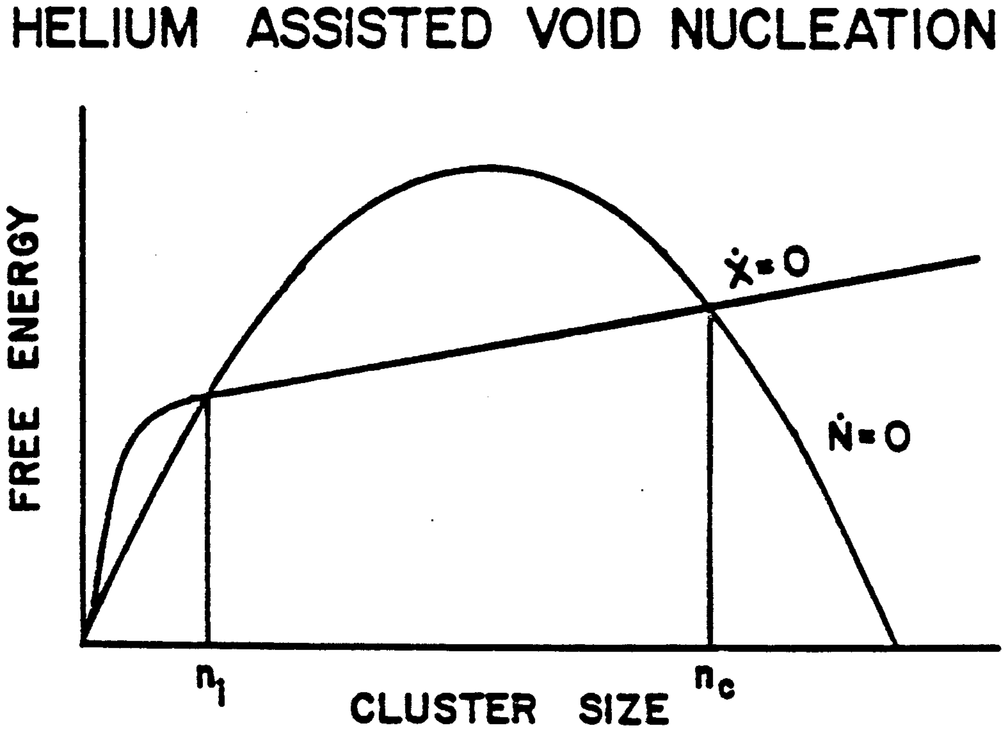
HELIUM ASSISTED VOID NUCLEATION

Fig. 3.11. Two cases of void nucleation as proposed by Russel (Ref. 3.46). The top curves are for gas free nucleation with and without interstitials. The bottom curve shows two nodal lines for vacancy clusters and gas clusters and the two critical points n_i and n_c.

As the production rate of defects during irradiation becomes balanced by the loss rate that results from recombination and sink annihilation, a quasi-steady state is approached as described qualitatively by Eq. 3.22. The steady state concentrations and supersaturations are determined by the temperature, displacement rate, and the sink annihilation probability. The effect of more sinks is to decrease the nucleation rate particularly at high temperature. The nucleation rate rapidly goes to zero with increasing temperature due to the strong decrease in vacancy supersaturation with temperature at a constant displacement rate. The effect of an increasing displacement rate n produces more vacancies, increasing the nucleation rate, and extending the upper temperature limit of nucleation cut off.

The effect of mobile helium gas on the void nucleation rate is very significant and various approaches by Katz and Weidersich, Russell, and Wolfer et al. all indicate that gases enhance void formation.

Katz and Weidersich find that the nucleation rate for a given displacement rate is independent of the gas concentration at low temperatures since homogeneous nucleation is dominant there. At higher temperatures the presence of only 0.1 at.ppm of mobile helium enhances the nucleation rate and increasing the mobile helium concentration to 10 at.ppm shifts the void nucleation into a gas driven regime where the growth rate is limited by the production of vacancies.

Russell separates the gas contribution to nucleation by his nodal line approach and obtains a void nucleation parameter that explicitly requires gas to be present or void formation is zero.(3.46) The concentration of gas in Russell's void nucleation parameter is not the at.ppm concentration but an effective gas concentration where gas trapping sites, resolution from voids, and resolution from other traps are included. Russell is requiring gas for void formation.

Wolfer and Yoo offer a modification to the free energy barrier for void formation by including another term in the free energy calculation. This has the effect of lowering the overall height of the free energy barrier but does not change the critical size of the void embryo. The effect of gas is to stabilize the void embryo by reducing the vacancy emission rate but when the void reaches a critical size the internal gas will have no effect.

The comparison of the many variations of nucleation, the cascade model, the homogeneous nucleation model, the gas assisted model, and the coalescence model shows some differences. The cascade model is dependent on the number of cascades and the concentration of helium gas while the homogeneous model suggests nucleation of voids can occur without significant concentrations of gas. An electron irradiation would not show spike nucleation while heavier incident ion beams would create larger displacement spikes and enhance the rate of spike stabilized nucleation. The preinjection of helium gas would eliminate the fluence dependence for helium generation and the numbers of nucleated spikes should be sensitive to the helium injection level. The homogeneous nucleation models suggest temperature is the dominate parameter with gas having a lesser role particularly at lower temperatures. The approach by Russell suggests that gas is required for void formation.

The concepts of homogeneous nucleation and heterogenous nucleation were reviewed here to describe the physical differences of the theories. The progression of nucleation theories and in particular homogeneous nucleation theory has led to the incorporation of many of the aspects of heterogenous nucleation into the homogeneous nucleation theory and there will be more changes in the future.

D. Void Growth

The four general requirements necessary for void swelling to develop in a material are : (1) vacancy supersaturation, (2) vacancy mobility, (3) void embryos and, (4) void growth. The first three requirements have been covered in some detail in the previous sections and now the next step is to determine the void growth rate.

There have been two approaches to the void growth problem. Bullough and Perrin(3.57) proposed a cellular model and rate theory models have been proposed by Weidersich,(3.58) Harkness and Li,(3.59) and Brailsford and Bullough.(3.60) The theory of Brailsford and Bullough, hereafter known as BB, is conceptually the same as the other theories but is less complicated and physically simpler.

The discreet sink density for point defects in rate theory is reduced to a continuum sink density that is easily treated mathematically. Voids, dislocations, grain boundaries, and impurities are all homogenized into this continuum of sinks. The essential assumption in BB is the voids grow because other sinks exist with a net bias for interstitials and since vacancies and interstitials are produced in equal numbers, a net flow of vacancies will occur to the unbiased sinks such as voids.

The equations describing BB theory relate the conservation of interstitials are

$$\frac{dC_v}{dt} = K' - D_v C_v k_v^2 - \alpha C_v C_i \qquad (3.23)$$

$$\frac{dC_i}{dt} = K - D_i C_i k_i^2 - \alpha C_v C_i \qquad (3.24)$$

where K' is the effective production rate of vacancies including thermal emission of vacancies, K is the atom displacement rate, C_i and C_v are the average interstitial and vacancy concentrations, D_i and D_v are the respective diffusion coefficients for vacancies and interstitials, and α is the effective recombination coefficient. The term DCk^2 refers to the loss of point defects to all sinks and 1/k is the mean free path a defect must travel before entering a sink.

The strength of each sink is determined by approximating the sink as a sphere with a radius R_s surrounded by another sink free sphere of R_0. These two concentric spheres are surrounded by an infinite medium containing a homogeneous distribution of the sinks of the particular system. The steady state concentrations of defects without recombination are described by

$$D\nabla^2 C + K = 0 \qquad \text{for } R_S < r < R_o \qquad (3.25)$$

$$D\nabla^2 C + K - DCk^2 = 0 \qquad \text{for } r > R_o \qquad (3.26)$$

The boundary condition is taken at the sink interface

$$r = r_s \qquad D\,\frac{dC}{dr} = \overline{K}(C - \overline{C}_o) \qquad (3.27)$$

where $\overline{K}$ is a transfer velocity of defects across the interface. The transfer rate is the jump frequency of the defect in the lattice. $\overline{K}$ has the form$^{(3.58)}$

$$\overline{K} = \frac{D}{b}\,\exp\left[\frac{-\Delta E_m}{kT}\right] \qquad (3.28)$$

where ΔE_m is the activation enthalpy. The term $\overline{KC_o}$ is the thermal emission rate where

$$\overline{C}_o = C_{eq}\,\exp[\Delta E/kT] \qquad (3.29)$$

with C_{eq} the equilibrium concentration of vacancies and ΔE is the change in enthalpy of the sink when the vacancy is emitted. $\overline{C}_o$ is a function of surface energy and internal gas pressure for voids while the $\overline{C}_o$ for dislocations depends on the stacking fault energy and dislocation line length. The energy of formation of interstitials is so large that thermal emission of interstitials is essentially zero.

Equations 3.25 and 3.26 also have the conditions of a continuous first derivative and continuous concentration at $r = r_s$. BB solved these equations to get

$$k_v^2 = 4\pi r_s C_s \tag{3.30}$$

and

$$k_d^2 = Z\rho_d \tag{3.31}$$

where ρ_d is the dislocation density and C_s is the void concentration.

The void sink term for finite surface transfer kinetics is given by(3.58)

$$k_v^2 = \frac{4\pi r_s C_s}{\left(1 + \frac{D}{\overline{K} r_s}\right)} \tag{3.32}$$

The expression is proportional to the void surface area. Biased sinks are represented by increasing the radius of a sink by the factor Z such that the effective sink radius will correctly define the point defect flux to the sink. The important aspect of Z_i and Z_v is the difference between the two $(Z_i - Z_v)$ which gives the bias factor for the drift rate of interstitials to the sink. Estimates for $Z_i - Z_v$ range from a high of 0.25(3.59) but is usually taken to be 0.01 to 0.02. Equations 3.23 and 3.24 can be solved with appropriate sink strengths to determine the point defect concentrations for the matrix. The void swelling rate results from the net flow of defects into the void sinks given by

$$\frac{d}{dt}\frac{(\Delta V)}{V_o} = 4\pi r_s C_s \left(D_v C_v - D_i C_i - D_v \overline{C}_o\right) \tag{3.33}$$

The factors that are strongly dependent on temperature can be factored into one term, called F(n) by BB, while the other term contains the irradiation and material parameters. The function of term F(n) is sensitive to the dose rate as well as the temperature and is the function that is responsible for the temperature shift. The temperature shift is experimentally observed and is the shifting of the bell shaped swelling curve from one temperature to another. The saturation level of point defects is dependent on the defect production rate or the displacement rate. A given number of these defects will recombine depending on their mobility and level of concentration. If the displacement rate is held at high level and the temperature is increased so that the defects have a much greater mobility, the concentration of defects is reduced, less recombination occurs, and the swelling rate increases. This phenomena is known as the temperature shift and can be derived from BB theory. An expression for the shift in temperature to a higher effective temperature is

$$T_1 = T_2 + \frac{T_2^2 \ln (K_2/K_1)}{\frac{E_v}{k} + T_2 \ln (K_2/K_1)} \tag{3.34}$$

where E_v is the diffusion energy, T_1 is the effective temperature, T_2 is the physical temperature, and K is the displacement rate.

REFERENCES FOR CHAPTER 3

3.1 D.R. Olander, Fundamental Aspects of Nuclear Reactor Fuel Elements, Technical Information Center, Office of Public Affairs, Energy Research and Development Administration (1976), TID-26711-P1, Chapt. 17.

3.2 I.M. Torrens and M.T. Robinson, "Computer Simulation of Atomic Displacement Cascades in Metals," Proceedings of the International Conference on Radiation Induced Voids in Metals, eds. J.W. Corbett and L.C. Ianniello, Albany, N.Y. (1971) CONF-710601, p. 739.

3.3 J. Lindhard, M. Scharff and H.E. Schiott, "Range Concepts and Heavy Ion Ranges," Mat. Fys. Medd Dan. Vid. Selsk. 33, No.14 (1963).

3.4 J. Lindhard, J. Nielsen, M. Scharff and P.V. Thomsen, "Integral Equations Governing Radiation Effects," Mat. Fys. Medd. Dan. Vid. Selsk. 33, No. 10 (1963).

3.5 J. Lindhard and M. Scharff, Phys Rev. 124, No. 128 (1961).

3.6 D.K. Brice, "Three-Parameter Formula for the Electronic Stopping Cross Section at Nonrelativistic Velocities," Physical Review A 6, No. 5, 1791 (1972).

3.7 I. Manning and G.P. Mueller, Com. Phy. Comm. 7, No. 85 (1974).

3.8 D.K. Brice, "Ion Implantation Depth Distributions: Energy Deposition into Atomic Processes and Ion Locations," Applied Physics Letters 16, No. 3, 103-106 (1970).

3.9 D.K. Brice, "Spatial Distribution of Energy Deposited into Atomic Processes in Ion-Implanted Silicon," Rad. Effects 6, 77-87 (1970).

3.10 D.K. Brice, "Depth Distribution of Energy Deposition by 4-40 MeV Fe^+ Incident of Fe," Rad. Effects 11, 51-54 (1971).

3.11 D.K. Brice, "Spatial Distribution of Ions Incident on a Solid Target as a Function of Instantaneous Energy," Rad. Effects 11, 227-240 (1971).

3.12 D.K. Brice, "Application of a Stopping Power Formula to Channeled Ions," Rad. Effects 18, 13-16 (1973).

3.13 M.T. Robinson, Nuclear Fusion Reactors, BNES, London, 1971, p. 410.

3.14 K. Shiraishi, A. Hishinuma, Y. Katano and T. Tacka, J. Phys. Soc. Japan 32, 114 (1972).

3.15 J.B. Whitely, "Depth Dependent Damage in Heavy Ion Irradiated Nickel," PhD. Thesis Univ. of Wisconsin (1978).

3.16 R.W. Knoll, "Effects of Heavy-Ion Irradiation on the Phase Stability of Several Copper-Base Alloys," PhD. Thesis Univ. of Wisconsin (1981).

3.17 J.R. Beeler, Jr., M.F. Beeler and C.V. Parks, "Collision Cascades in Iron and Niobium," Radiation Effects and Tritium Technology for Fusion Reactors, Proceedings of a Conference CONF-750989, Vol. I, p. 362.

3.18 J.R. Beeler, Jr., "Computer Simulation of Radiation-Induced Void Nucleation and Growth in Metals," Proceedings of International Conference on Radiation Induced Voids in Metals, ed. by J.W. Corbett and L.C. Ianniello, Albany, N.Y. (1971) CONF-710601, p. 684.

3.19 D.G. Doran and R.A. Burnett, "Computer Simulation of Short Term Annealing of Displacement Cascades," Batelle Colloquium, Interatomic Potentials and Simulation of Lattice Defects, Paper III-6, June 14-19, 1971.

3.20 A.D. Marwick, "The Primary Recoil Spectrum in the Simulation of Fast Reactor Radiation Damage by Charged-Particle Bombardment," J. of Nucl. Mat. 55, 259-266 (1975).

3.21 K.L. Merkle and R.S. Averback, "Energetic Displacement Cascades at Elevated Temperature," Fund. Aspects of Rad. Damage in Metals 1, p. 127.

3.22 M.J. Norgett, The Physics of Irradiation Produced Voids, ed. R.S. Nelson, Harwell, Oxfordshire, U.K., Sept. 1974, AERE-R7934 (1975), p. 44.

3.23 K.B. Winterbon, P. Sigmund and J.B. Sanders, Mat. Fys. Medd. Dan. Vid. Selsk. 37, No. 14 (1970).

3.24 R.L. Lyles and K.L. Merkle, "14 MeV Neutron Damage in Silver and Gold," Radiation Effects and Tritium Technology for Fusion Reactors, Proceedings of a Conference, CONF-750989 Vol.I, p. 191.

3.25 R. Bullough, B.L. Eyre and K. Krishan, "Cascade Damage Effects on the Swelling of Irradiated Materials," Proc. R. Soc. Lond. A. 346, 81-102 (1975).

3.26 A. Taylor, D.I. Potter and H. Wiedersich, "The Effects of Pulsed Irradiation on Void Microstructure in Nickel," Argonne National Laboratory Report ANL/FPP-79-3.

3.27 N. Ghoniem, "Transwell," Univ. of Wis. Fusion Design Memo No. 181.

3.28 J.R. Beeler, Jr., "Computer Simulation to Predict Radiation Effects in Reactor Materials," IAEA-SM-1201E1.

3.29 J.B. Gibson, A.N. Goland, M. Milgram, and G.H. Vineyard, "Dynamics of Radiation Damage," Phys. Rev. 120, 1229 (1960).

3.30 R.A. Johnson, "Point Defect Calculations for an FCC Lattice," Phys. Rev. 145, 423 (1966).

3.31 D.G. Besco and J.R. Beeler, Jr., "Computer Programs Describing Collision Cascades in Binary Materials; III. Body-Centered Cubic and Face-Centered Cubic Structures," USAECK Report GEMP-243, General Electric Company, Nuclear Materials and Propulsion Operation (1963).

3.32 D.G. Besco, "Computer Simulation of Point Defect Annealing in Metals," USAECK Report GEMP-644, General Electric Company, Nuclear Materials and Propulsion Operation (1967).

3.33 J.R. Beeler, Jr., "Computer Experiment Studies on Mechanisms for Irradiation Induced Defect Production and Annealing Processes Progress Report," USAEC KReport ORO-3912-4, NCSU, (1970).

3.34 J.R. Beeler, Jr., and R.A. Johnson, "Vacancy Clusters in Alpha Iron," Phys. Rev. 156, 677 (1967).

3.35 D.G. Doran, "Computer Simulation of Displacement Spike Annealing," Rad. Eff. 2, 249 (1970).

3.36 J.L. Katz and H. Wiedersich, J. Chem. Phys. 55, 1414 (1973).

3.37 J.L. Katz and H. Wiedersich, J. of Nucl. Mat. 46, 41 (1973).

3.38 K.C. Russell, "Nucleation of Voids in Irradiated Metals," Acta Met. 19, 753-758 (1971).

3.39 K.C. Russell, "Nucleation of Voids in Irradiated Metals; II. The General Case," Scripta Met. 6, 209-214 (1972).

3.40 W.G. Wolfer and M. Ashkin, "Stress-Induced Diffusion of Point Defects to Spherical Sinks," J. Appl. Phys. 46, 547 (1975).

3.41 W.G. Wolfer and M.H. Yoo, "The Effect of Stress-Induced Diffusion on Void Nucleation," Radiation Effects and Tritium Technology for Fusion Reactors - II, CONF-750989 (1975), p. 458.

3.42 H. Wiedersich and J.J. Burton, "Effect of Mobile Helium on Void Nucleation in Materials During Irradiation," J. Nucl. Mat. 51, 287 (1974).

3.43 H. Wiedersich and J.L. Katz, "The Theory of Nucleation," Proc. of Conf. on Correlation of Neutron and Charged Particle Radiation Damage, CONF-760763 (1976), p. 21.

3.44 K.C. Russell, "Nucleation of Voids in Irradiated Metals, III. Impurity Effects," Scripta Met. 7, 755-760 (1973).

3.45 K.C. Russell, "Comment on Theories for Helium-Assisted Void Nucleation," J. of Nucl. Mat. 61, 330-333 (1976).

3.46 K.C. Russell, "The Theory of Void Nucleation in Metals," Acta Met. 26, 1615-1630 (1978).

3.47 J.R. Beeler, Jr., "Displacement Spikes in Cubic Metals; I. Alpha Iron, Copper, and Tungsten," Phys. Rev. 150, 470 (1960).

3.48 V. Levy, The Physics of Irradiation Produced Voids, edited by R.S. Nelson, HMSO London (1975), p. 50.

3.49 J.H. Shively, General Discussion, in Radiation Damage in Reactor Materials, Sym. Proc., Vol. 2, IAEA, Vienna, STI/PUB/230 (1969), p. 253.

3.50 B.N. Singh and A.J.E. Foreman, The Physics of Irradiation Produced Voids, HMSO London (1975), p. 205.

3.51 W. Bauer and G.J. Thomas, J. Nucl. Mat. 42, 96 (1972).

3.52 W. Bauer and D. Morse, J. Nucl. Mat. 44, 337 (1972).

3.53 F.A. Smidt, Jr. and A.G. Pieper, "Helium Mobility and Bubble Formation in 316 SS, Aluminum, and Vanadium," to be published.

3.54 W.D. Wilson and R.A. Johnson, Interatomic Potentials and Simulation of Point Defects, P.C. Gehlen, J.R. Beeler, Jr., R.K. Jaffee, editors, Plenum Press, NY (1972), p. 375.

3.55 D.J. Reed, "Review Article: A Review of Recent Theoretical Developments in the Understanding of Migration of Helium in Metals and Its Interaction with Lattice Defects," Rad. Eff. 31, 129-147 (1977).

3.56 T.L. Davis, "Nucleation Rate of Vacancy Clusters in Aluminum," J. Appl. Phy. 9, 3756-3760 (1967).

3.57 R. Bullough and R.C. Perrin, Radiation Induced Voids in Metals, Proc. of Int. Conf., CONF-710601 (1972), p. 769.

3.58 H. Wiedersich, Rad. Eff. 12, 111 (1972).

3.59 S.D. Harkness and Che-Yu Li, "A Study of Void Formation in Fast Neutron-Irradiated Metals," Met. Tran. 2, 1457 (1971).

3.60 A.D. Brailsford and R. Bullough, J. Nucl. Mat. 44, 121 (1972).

CHAPTER 4: EXPERIMENTAL APPARATUS AND METHODS

The experimental apparatus and experimental methods used in this study are described along with a chronological history of a sample. The numerous discussions with fellow graduate students, professors, and research scientists were invaluable toward completing an experimental setup. The indebtedness to the many helpful ideas is acknowledged and appreciated.

A. As Received Material Description

The material used in this study was used by Packan(4.1) for neutron irradiation and by Sundquist(4.2) for ion irradiation. A number of HVEM irradiations by Yang(4.3) were also performed on the same material. The material analysis was characterized by Packan(4.4) and is reported in Table 4.1. This material was originally obtained from Cominico and a recent irradiation by Green(4.5) with 600 MeV protons used the same Cominico source for the high purity aluminum.

The aluminum rods used by Packan were cold rolled to a thickness of 200 μm (0.008 inches or 8 mils) for ion irradiations and were about 2 cm (one inch) in width and 15 cm (6 inches) long.

B. Preirradiation Polish and Preparation

Samples were prepared in the form of 3.18 mm (1/8 inch) disks for irradiation and transmission electron microscope analysis. The disks were punched from the aluminum sheets with a precision hand punch manufactured by Fulham.(4.6) The aluminum was very soft and

TABLE 4.1

IMPURITIES IN HIGH PURITY ALUMINUM

Element	at.ppm
Boron	1.0
Calcium	0.6
Chromium	0.08
Copper	0.06
Iron	0.3
Indium	0.04
Potassium	0.5
Magnesium	0.3
Manganese	0.04
Sodium	0.1
Nickel	0.07
Silicon	4.0
Tantalum	0.04
Titanium	0.1
Zinc	0.4
TOTAL	7.3

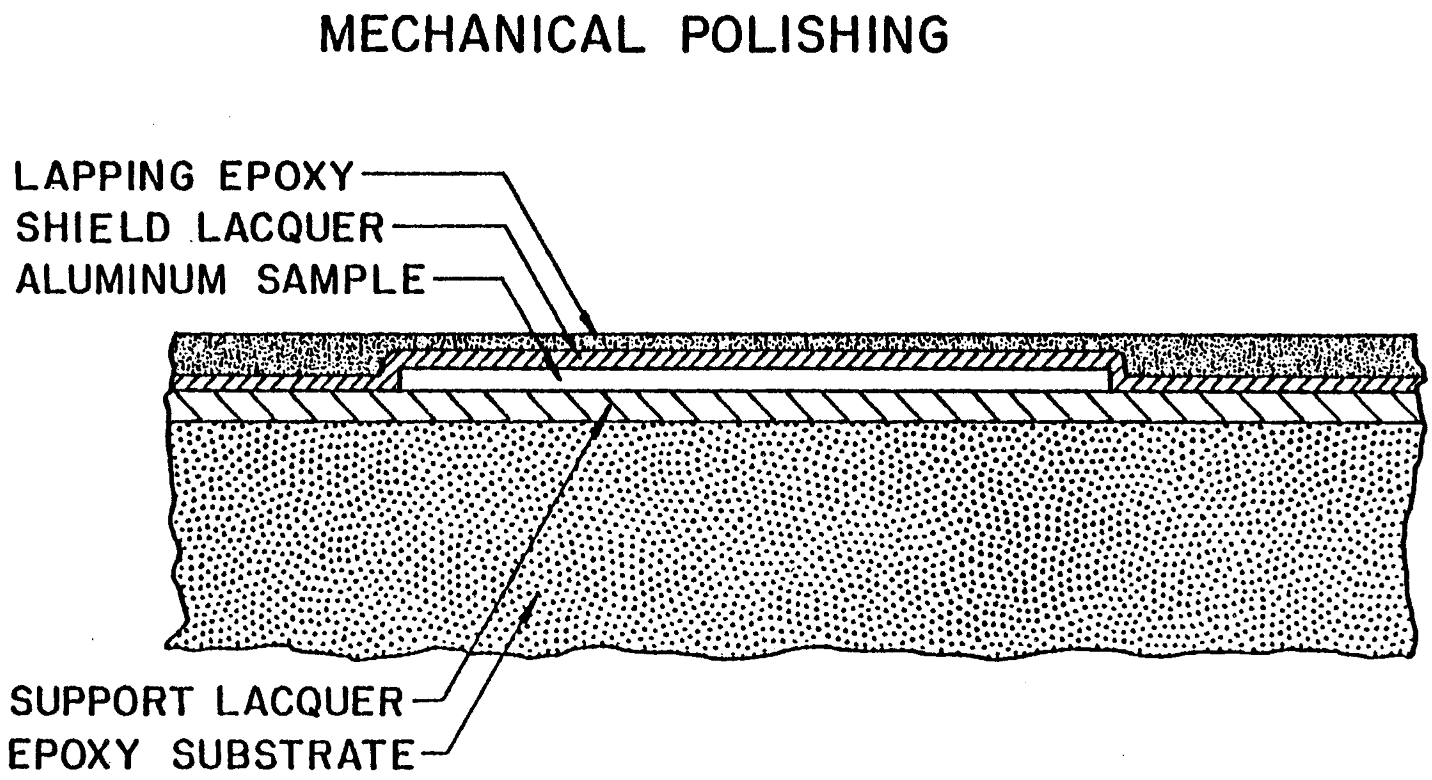

Fig. 4.1. Diagram of the rough-fine mechanical polishing arrangement for initial mechanical polishing. A cross-section diagram showing the substrate, microstop, sample, microstop, and epoxy layers.

ductile and paper cards of 75 to 100 μm thickness were helpful in reducing the burrs and bending of the three millimeter disks. The bent aluminum disks were flattened by compression between two hard, flat surfaces. Glass microscope slides or a machinist micrometer each work well for flattening the aluminum disks. The three millimeter aluminum disks were ready for the first stage of polishing.

The mechanical punching of the disks produced a burr that was reduced by placing the aluminum foil between two paper cards. The samples were placed on a polishing holder so that any burr that was produced can be mechanically polished away. This is necessary to reduce the burr's interference in the irradiation sample holder and the analysis stage for the transmission electron microscope. The mechanical polish of the samples was done by placing the samples with the burr side up onto a polishing boat as pictured in Fig. 4.1. The boat substrate was thermoset plastic or epoxy castings that were ground flat with 600 grit silicon carbide on a Buehler hand grinder.(4.7) An adhesion surface of microstop(4.8) was applied to the substrate and reground to a flatness that enabled the even polishing of an aluminum disk. The aluminum disks were then attached to the microstop coated carrier with acetone which partially dissolved the microstop, bonding the aluminum disk to the carrier. The carrier with 15 to 30 disks were given another coat of microstop to completely surround the aluminum disks and when dry, a coating of epoxy was placed over the aluminum disks to provide a firm, hard material for even mechanical polishing. The samples were mechanically ground on 600 silicon carbide to expose the aluminum surface and they were then placed into a Syntron vibropolisher(4.9) with 0.3 μm alumina abrasive in distilled water containing a few drops tincture of green soap. The green soap acts as a buffer to prevent the high purity aluminum from pitting in the polishing slurry.(4.10) The samples were polished 24 to 48 hours until the finish was mirror-like. The aluminum had a flat surface that contained scratches less than a micrometer in depth. The samples were removed by soaking the sample carrier in acetone for a few hours. The acetone dissolved the microstop surrounding the sample and allowed the sample to be removed from the carrier. The samples were ready for the third and final polishing step.

The fine scratches of one micrometer size were removed by a 30 second electropolish in a cold solution of 20% perchloric acid and 80% ethyl alcohol. The samples were attached to an electropolishing holder shown in Fig. 4.2 using silver paint and areas not to be polished were insulated from the electropolishing solution by microstop lacquer. A cross section of the final preirradiation electropolish arrangement is shown in Fig. 4.2. The samples were removed from the electropolish holder by an acetone soak to dissolve the silver paint and microstop lacquer and then each sample was numbered by scratching a number into the back side of the sample. The samples had distinct fronts and backs with the front having a mirror like finish and the back surface in the as received condition with an

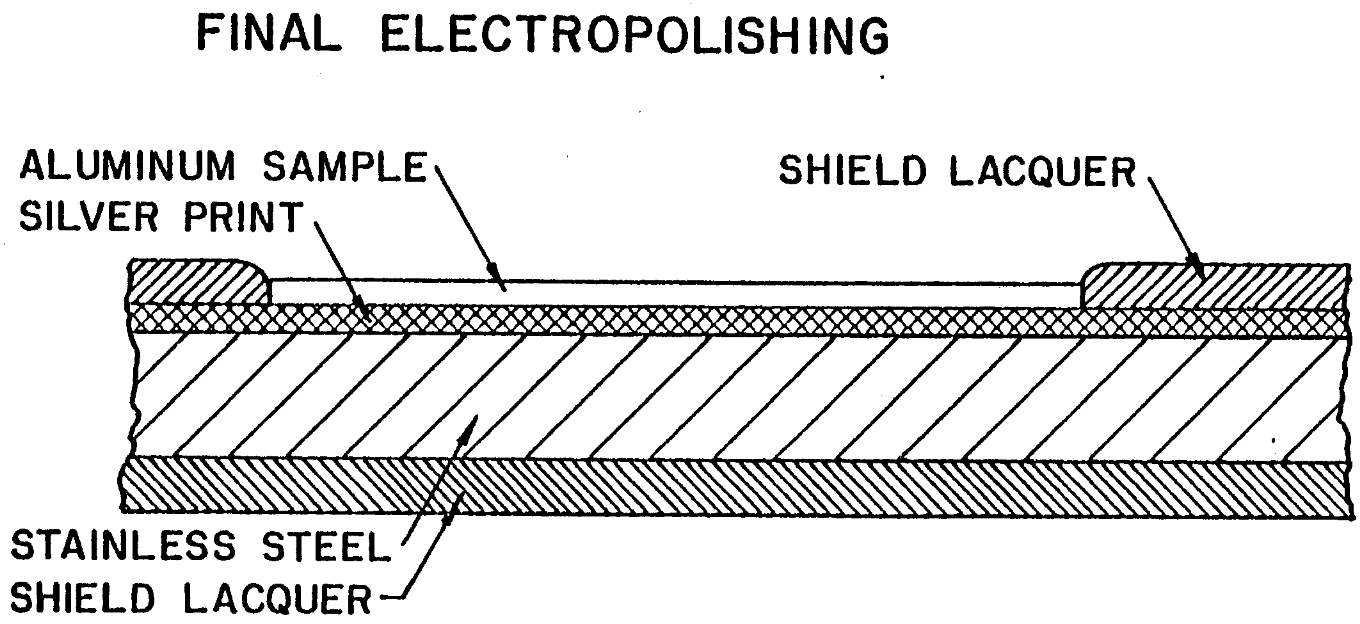

Fig. 4.2. Cross-section diagram of the electropolish arrangement for aluminum sample preirradiation electropolish. The layers show the stainless steel substrate, the silver paint, the aluminum sample, and the microstop.

identification number. The samples were then stored in a room temperature desiccator after electropolishing and numbering.

Annealing of the aluminum samples was performed in an ultra high vacuum system described by Weber.(4.11) The annealing was done at 550°C for one hour at a vacuum of less than 5×10^{-8} Torr (7×10^{-6} pascals). The annealed samples were stored in a dessicator at room temperature until irradiated. The high temperature and high purity of the aluminum produced a large grain size of 500 μm (30 grains in 7.9 square millimeters as shown in Fig. 4.3). Any hydrogen charging that appears in other electropolished metals was removed by the high temperature and high vacuum anneal. The residual gases present during an anneal were dominated by hydrogen and water vapor as shown in Fig. 4.4.

C. Helium Preinjection

Preinjection of helium into the aluminum was performed using a radioactive source of helium by the Isotope Sales Division of Oak Ridge National Laboratories. The helium injection has been described by Packan(4.12) and the experimental arrangement is shown in Fig. 4.5. The radioactive Cm-242 was the source of 5.8 MeV alpha particles which have a total range of 28 μm in aluminum. A finite thickness or thin film source of the Cm-242 was placed onto a titanium substrate and samples to be doped with the alpha particles was placed near the film source. The Cm-242 film is thin enough to allow an α particle emitted from the far side of the film to penetrate the Cm-242 film and travel an additional distance into the aluminum sample.

Fig. 4.3. An optical micrograph showing the grain size and grain structure of an annealed aluminum sample.

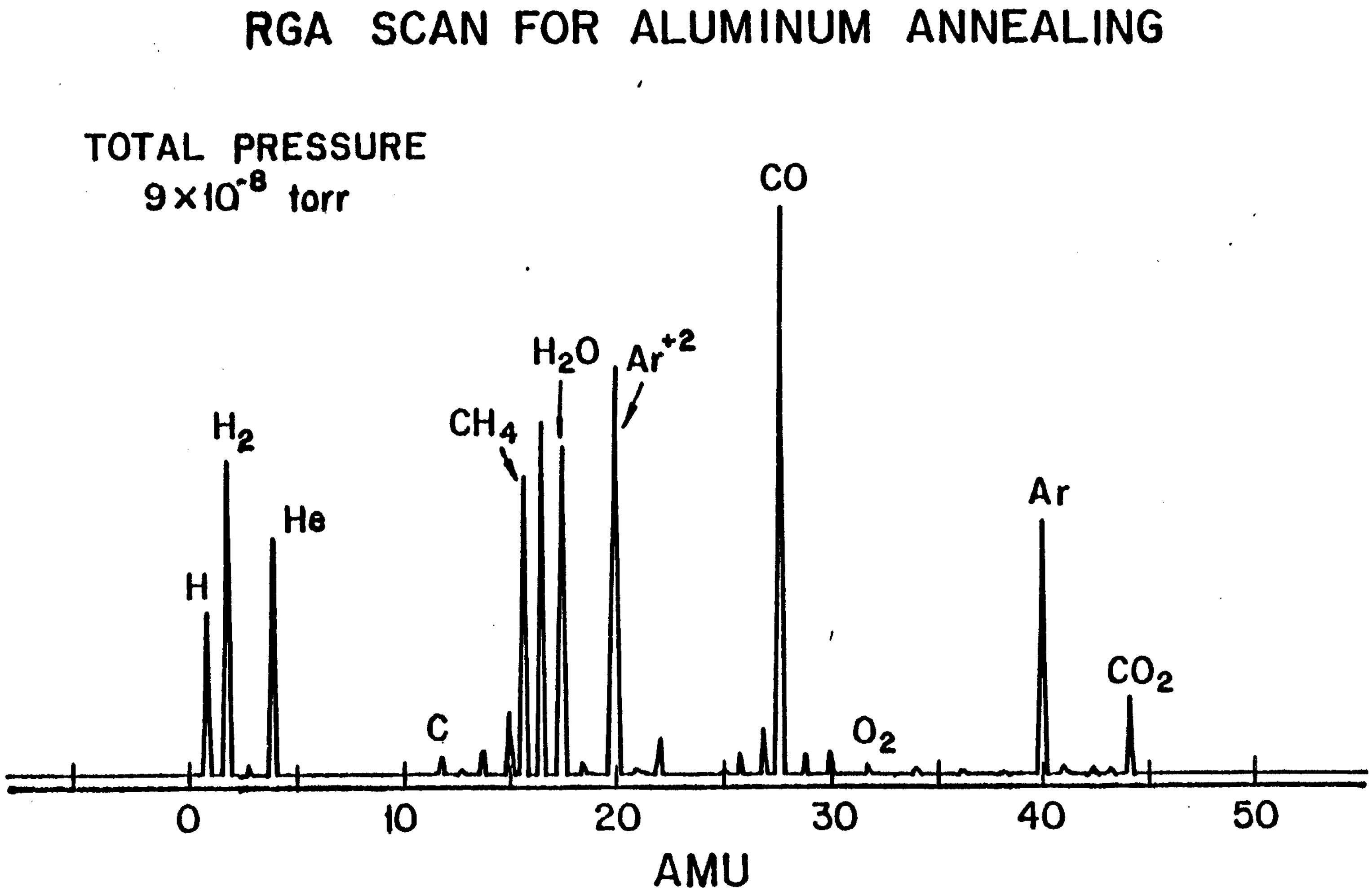

Fig. 4.4. The residual gas analysis of the annealing of a lot of aluminum samples. Pressure is 9 x 10^{-8} torr at 500°C.

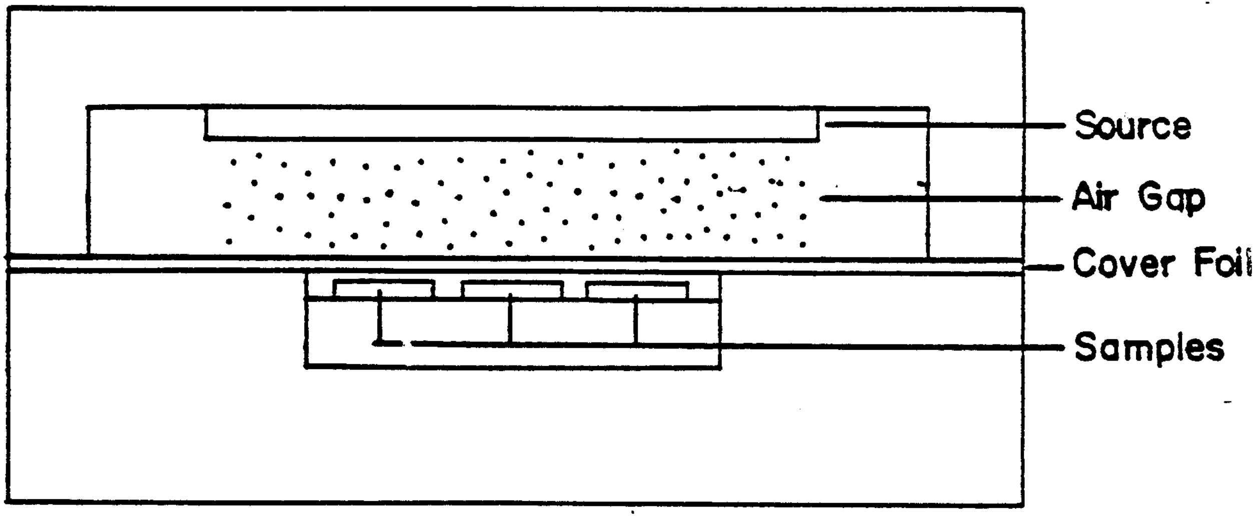

RADIOACTIVE HELIUM SOURCE

Fig. 4.5. The radioactive helium irradiation schematic for Cm-242 sources. Helium is injected into the aluminum disks from a thin Cm-242 alpha emitter.

The isotropic emission of the alpha particles produces a constant concentration of helium atoms in the irradiated material to the depth x^* as shown in the Fig. 4.6. There are deviations from the ideal flat line concentration because of the finite size of the radioactive source. The samples are arranged in three concentric circles as in Fig. 4.7. The twelve samples are grouped in an inner ring of three, a middle ring of three, and an outer ring of six samples. The samples closer to the outer edge of the helium source see more of the finite edge of the source than samples in the center ring. The deviation from the infinite source curve by the finite size of the source is eliminated by a cover foil placed over the sample. The x^* distance for aluminum is approximately 20 μm and a 5 μm cover foil of aluminum is sufficient to eliminate the finite source effects and provide a helium doped region twice the total range of the irradiating aluminum ion.

Three lots of twelve samples each were irradiated to doses of 0.1, 1.0, and 10 at.ppm of helium. The helium concentrations were calculated from data supplied by Packan for source 0 calibration data. The absolute level of helium can be determined from cover foils placed over a sample in each of the three rings of the three irradiated batches but the major emphasis is directed at the relative levels of helium rather than the absolute levels. The nominal concentrations of helium are maximum values and are believed to be 10 to 20% low since the sources have deteriorated from helium embrittlement of the titanium substrate.

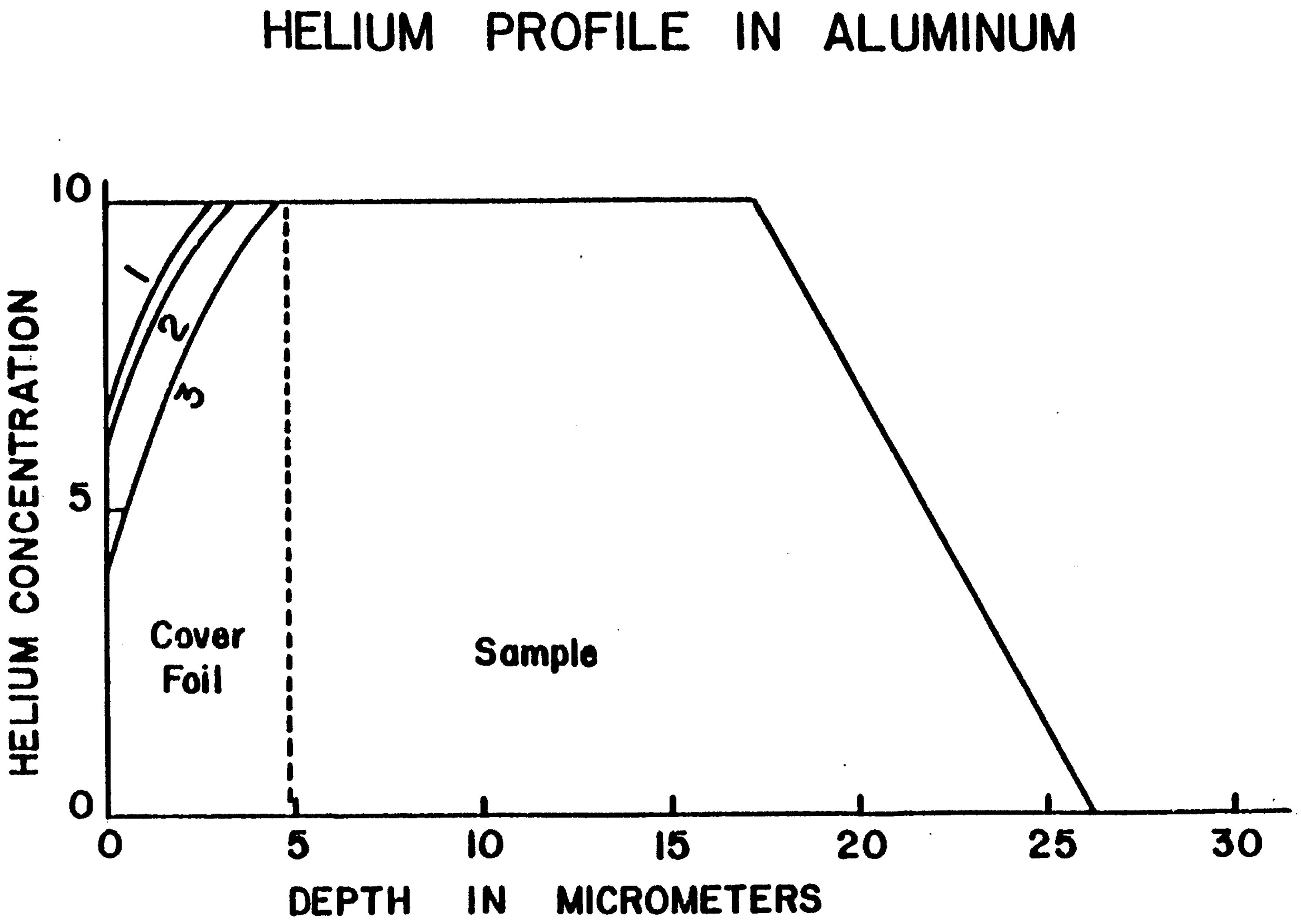

Fig. 4.6. A plot of the relative concentrations of helium from the Cm-242 source.

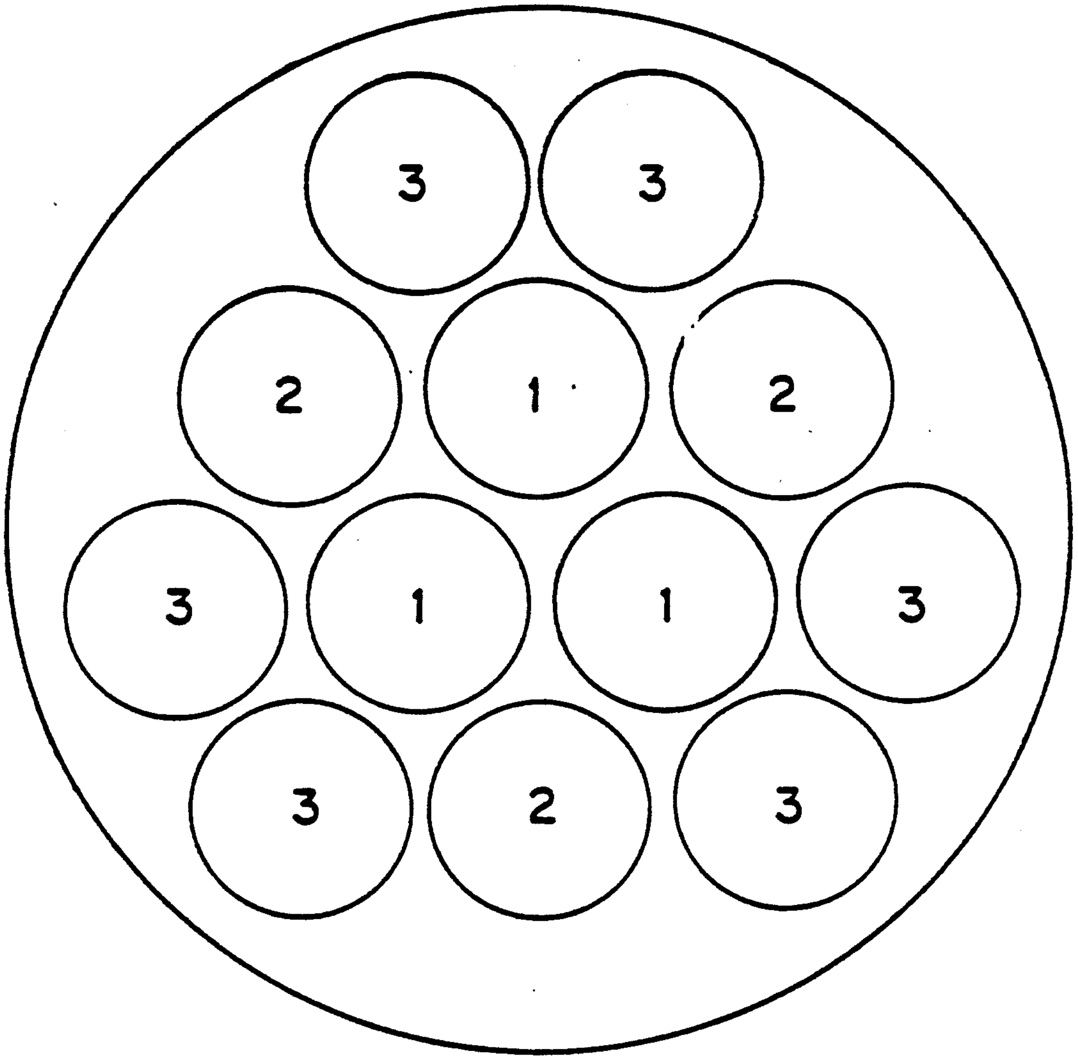

ALUMINUM SAMPLE HOLDER FOR HELIUM PREINJECTION

Fig. 4.7. A picture of the sample holder showing the concentric arrangement of sample positions.

A radioactive survey of the samples returned from Oak Ridge showed very low levels of activity but contamination was visible from the unaided eye. Examination of the samples with scanning electron microscope and x-ray analysis of the contamination could not find any detectable amounts of Cm-242 or any element other than aluminum. The contamination was worse on the 10 at.ppm helium irradiations and thus related to the dose. The irradiation environment produces other chemical products and the contamination was believed to be composed of organic compounds since the x-ray analysis can detect elements with atomic numbers greater than 10. The contamination could not be removed with methyl alcohol or acetone but a five minute soak in a cold chromic acid solution removed the contamination. Figure 4.8 shows the aluminum surface after 10 at.ppm helium irradiation and Fig. 4.9 shows the same surface after a 5 minute soak in 0°C chromic acid solution. All of the samples were soaked in the chromic acid solution for 15 minutes to remove the contamination, before aluminum ion irradiation to remove any contamination layers. The cleaned helium doped samples were stored in a cold (-20°C) dessicator until irradiation with heavy ions.

D. Material Irradiation

All of the heavy ion irradiations were done in the University of Wisconsin Heavy Ion Irradiation facility using a HVEC Model E Tandem Van De Graff Accelerator. The irradiation facility was designed to irradiate materials from a selection of ion beams at high vacuum and

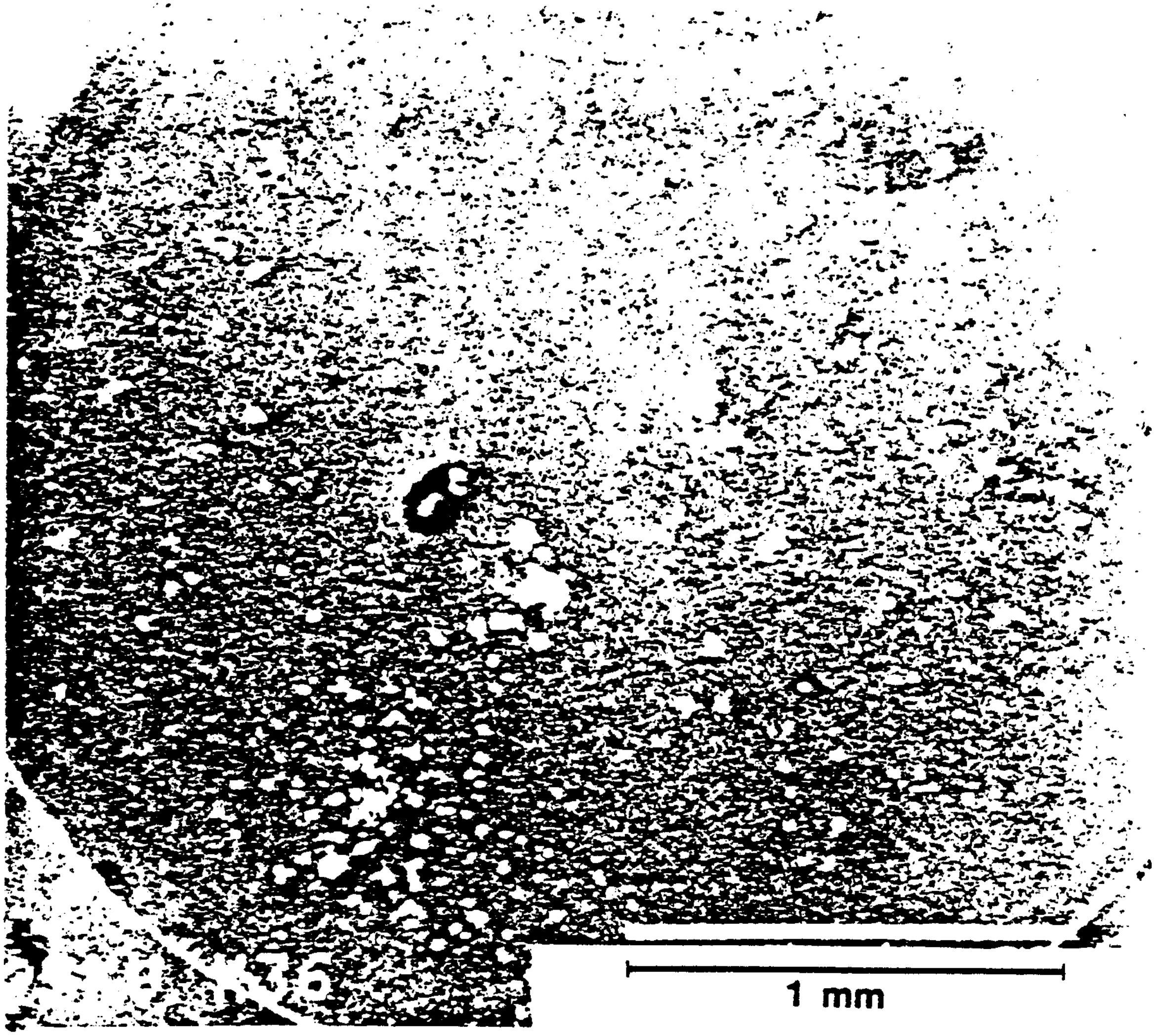

CONTAMINATION ON ALUMINUM DISK

AFTER HELIUM DOPING

Fig. 4.8. Scanning electron micrograph of contaminated aluminum surface after helium irradiation and before cleaning.

HELIUM DOPED ALUMINUM DISK AFTER CLEANING IN CHROMIC ACID

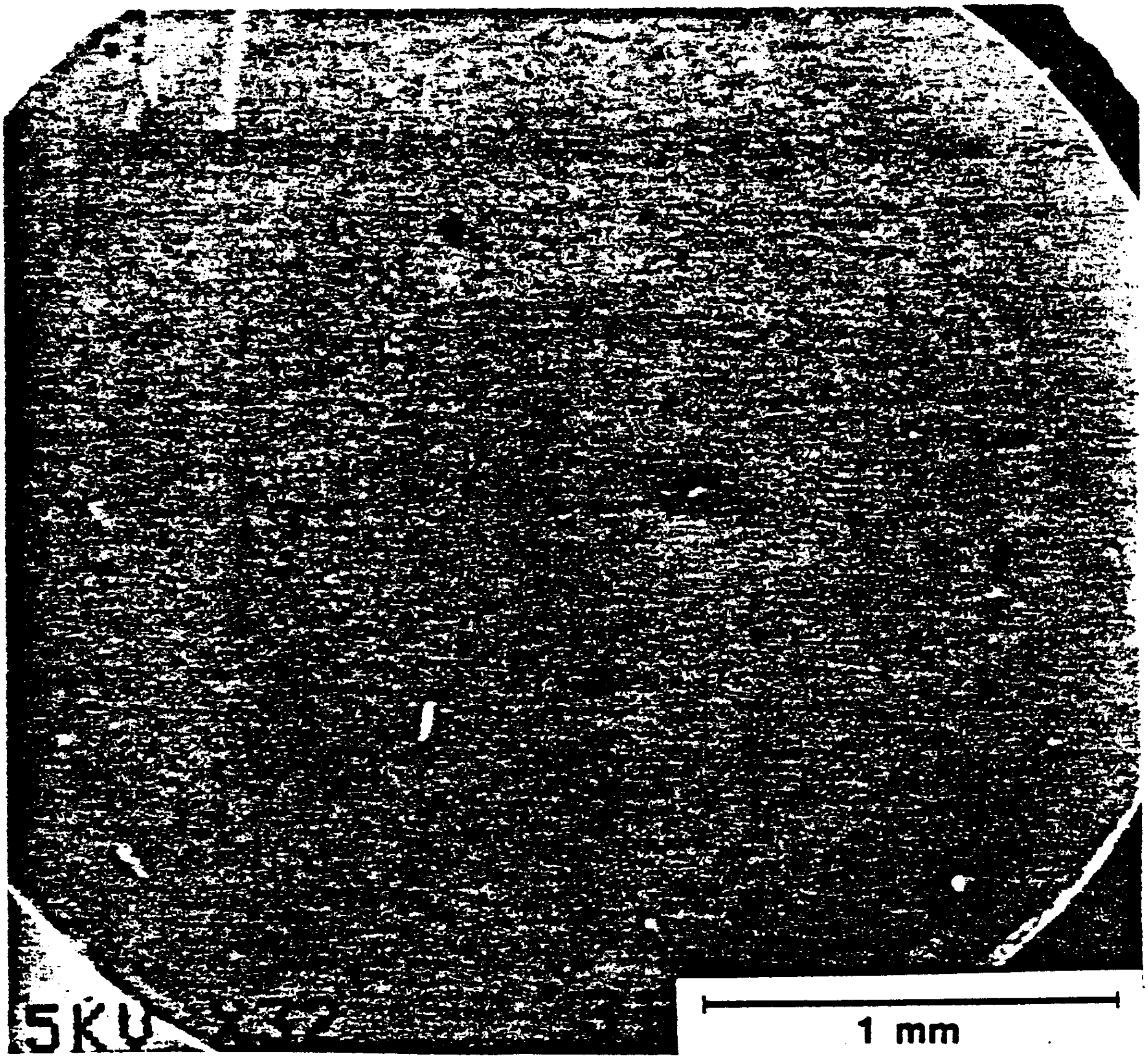

Fig. 4.9. Scanning electron micrograph of same area after cleaning with cold chromic acid solution.

provide experimental diagnostics and control of temperature, pressure, and beam current.

The irradiation was accomplished by creating a source of negatively charged metal ions which were injected into the first half of the tandem accelerator and accelerated to the positively charged terminal or dome. A schematic of the Wisconsin Heavy Ion Irradiation facility is shown in Fig. 4.10. The negative metal ions were converted to positive ions in a gas stripper and were further accelerated by repulsion from the positively charged terminal. Beam handling equipment was used to select and direct an appropriate beam to the irradiation target area. The irradiation sample chamber maintained a high vacuum and a controlled temperature throughout the irradiation.

Negative ions of copper and aluminum were used in this study and were produced by two types of sputter ion sources. A sputter penning ion gauge source (SPIGS) was developed by Smith and Richards(4.13) and used for the copper ion irradiation of aluminum. Later developments and refinements of the SPIG source by Caskey(4.14) lead to a surface ionization negative ion source or SNICS which produced 10 times the beams of SPIGS and produced suitable aluminum negative ion beams. The aluminum ion produced by SNICS is a two atom molecule of aluminum sharing a single negative charge. The acceleration of the aluminum molecule to the dome potential and subsequent ionization to a positive charge state results in the net energy being divided between to two aluminum atoms of the original molecule. The final

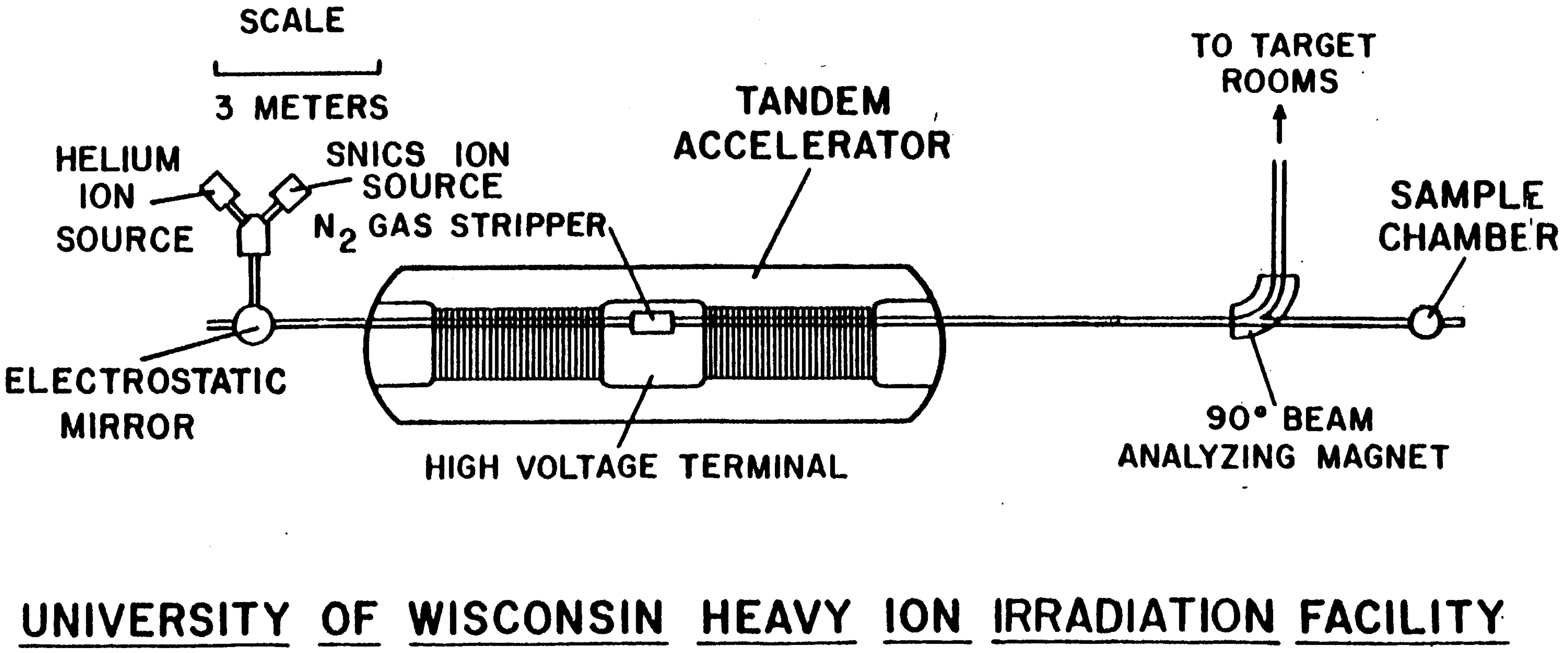

Fig. 4.10. A schematic of the University of Wisconsin Heavy Ion Irradiation Facility.

energy was obtained by the repulsion of the positive aluminum ions from the terminal and out of the accelerator. For a given impressed voltage on the tandem accelerator terminal, the final energy is given as

$$E = (q + 1/2)V \qquad (4.1)$$

where the effective negative charge ($q_{/neg}$) for aluminum (Al_2^{-1}) is one half and the positive charge state after gas stripping is two (Al^{+2}). A dome potential of 3.6 million volts gives a final energy of 9 MeV for the bombarding aluminum ion. The SNICS source provided a typical input beam of 2 microamps (4 particle microamps) and the accelerator emitted a 2 microamp (1 particle microamp) beam at 9 MeV. The plus two charge state was selected by a combination of quadripole lens focusing and magnet deflection of less than one degree to provide a 800 nanoamp aluminum beam at the exit of the deflection magnet. The beam was collimated and focused to a three millimeter spot in the target area with 200 nanoamps of aluminum available. The beam was collected by the sample holder and a 4 π geometry can surrounding the sample that subtended 95% of the secondary electron emission solid angle. The beam current can be measured through the heat conduction rod or through one of the thermocouple wires. The beam current was integrated by current to frequency conversion and displayed by scalers to determine the total dose. An RC filter was used to attenuate the 60 Hz noise on the beam current signal and the resistor provided 10 volts of suppression at 200 nanoamps of beam current. A 200 nanoamp (100 particle nanoamp) aluminum 2^+ beam at 9 MeV produced 1.8 watts of beam heating.

The two watts of beam heating can produce large temperature changes. The three millimeter diameter, 200 μm thick aluminum disk has a mass of four milligrams and a specific heat capacity of four milliwatts/°C. The operating temperature of the sample depended on the conduction path between the sample and the major mass of the sample holder. If a good conduction path existed between the irradiated aluminum sample and the sample holder then the temperature rise within the sample was less than 1°C with 2 watts of beam heating. The range of the 9 MeV aluminum ion was six micrometers (Fig. 4.11) and the energy deposition from electron losses was linear over the six micrometer range. If all of the energy was deposited at the surface the resulting temperature rise at the surface of the sample was 1.2°C with a constant temperature boundary condition applied at the back surface of the 200 μm aluminum disk.

The radiation damage target chamber was designed by Lott, Smith, and Weber(4.15) to provide a high vacuum environment at high temperatures suitable for refractory element irradiations. A schematic view of the radiation damage target chamber is shown in Fig. 4.12. The accelerator vacuum operates in a range of 5×10^6 Torr and this vacuum is reduced at the target chamber by two stages of differential pumping. A 400 liter/second diffusion pump provides a vacuum of 2×10^{-6} Torr in the first stage. The intermediate pumping is by a

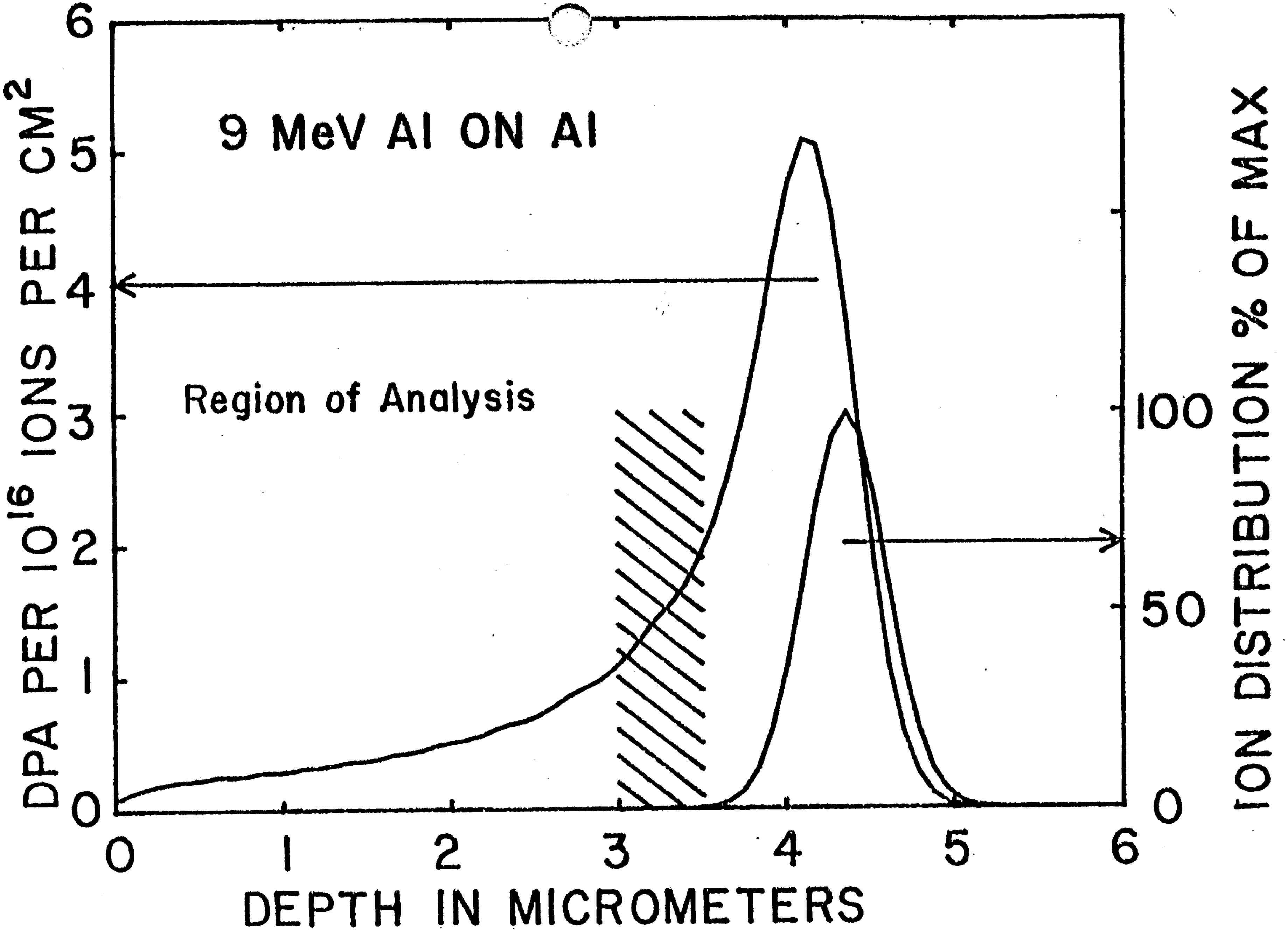

Fig. 4.11. The aluminum ion damage and the aluminum ion range as a function of the distance of ion penetration into aluminum metal. The region of analysis was the region examined in the transmission electron microscope with the corresponding dimension

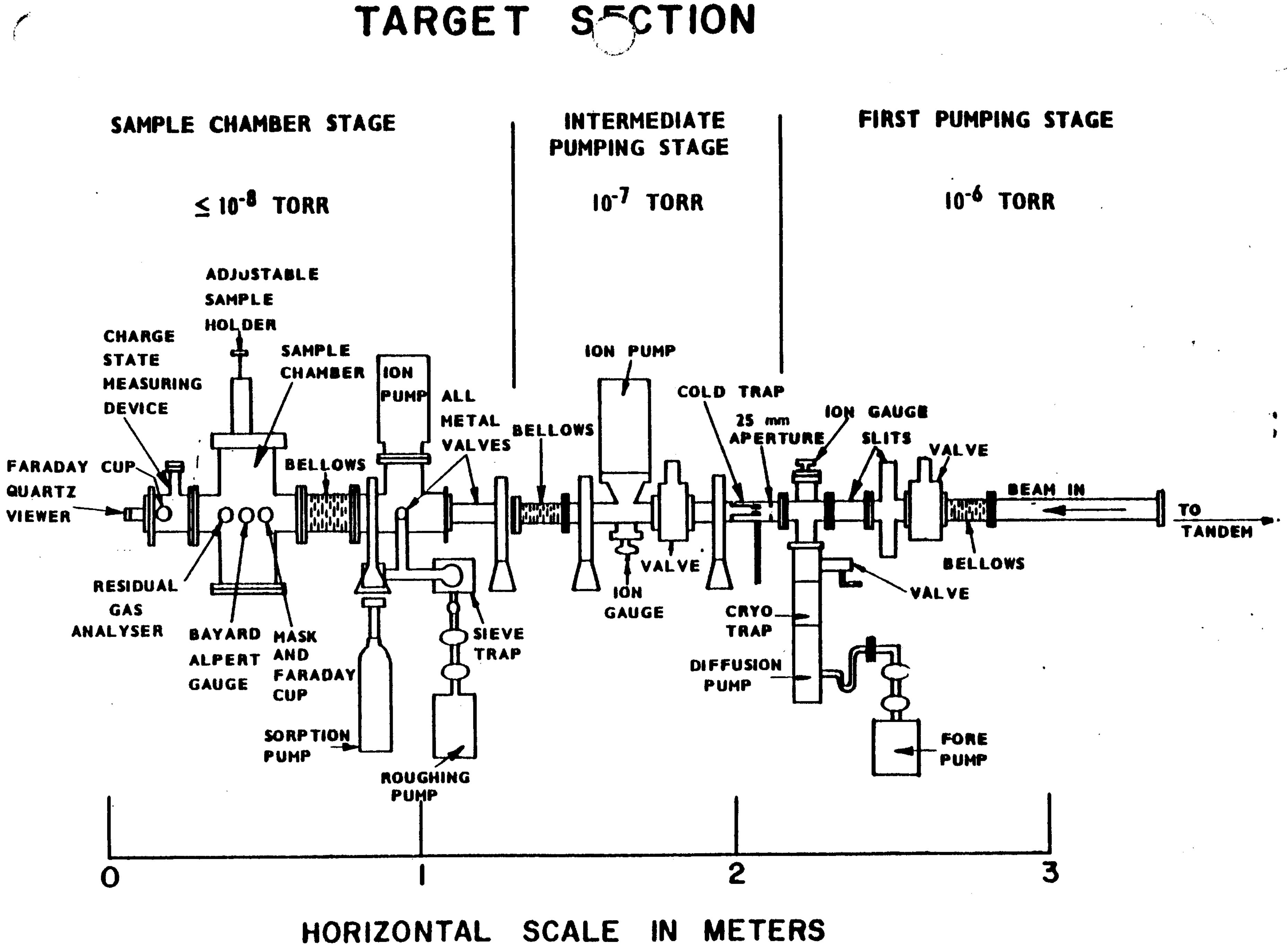

Fig. 4.12. A schematic of the radiation damage target chamber showing the vacuum related equipment and temperature control equipment.

sublimation pump with a vacuum of 1 x 10^{-7} Torr. The final vacuum of 8 x 10^{-9} is obtained with a 1000 liter/second getter-ion pump. A Varian VGA-100 residual gas analyzer is used to monitor the vacuum composition.

Since aluminum does not need the high temperature design of the furnace and a room temperature sample stage was designed to provide both heating and cooling. The high temperature design provides substantial insulation and beam heating from the accelerator beam is sufficient to provide 70 to 100°C. The temperature control uses heat conduction to control the sample temperature. A thermoelectric module with a heat pumping capacity of 20 watts was used to control the flow of heat to and from the samples. A diagram of the sample holder is shown in Fig. 4.13 and a picture of the sample holder and conduction path is shown in Fig. 4.14. The thermal conduction path is entirely aluminum which has excellent thermal response characteristics. A copper feed-through is used to provide the conduction path outside the vacuum chamber to the thermoelectric module. The thermoelectric module is cooled by water for low temperature irradiations and insulated irradiations higher than 75°C.

An automatic temperature controller was designed and built to regulate the the temperature of the sample holder. The small size of the heater power and the relative large mass of the sample holder introduces a large time delay requiring regulation of the temperature of the thermoelectric module rather than the sample temperature. The controller uses the analog output of the thermocouple reader to sense

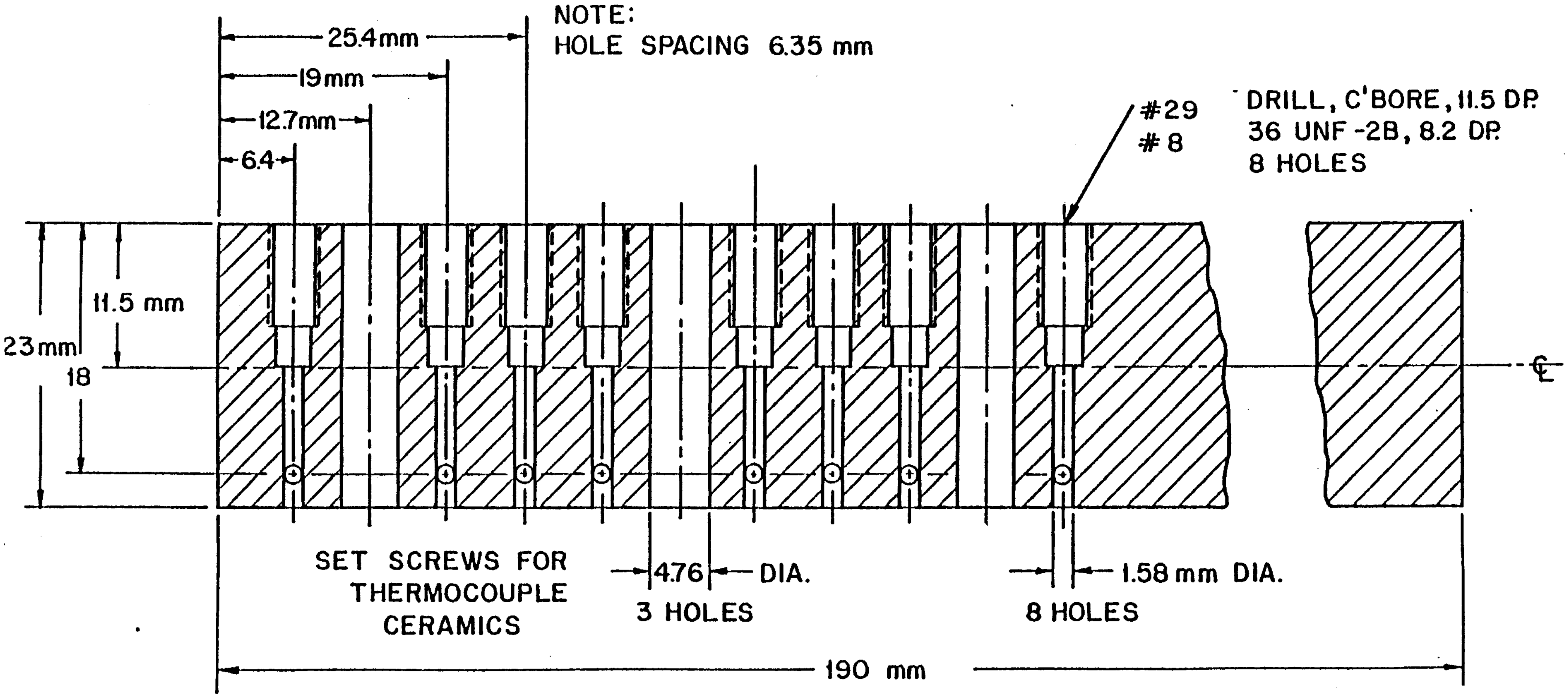

CROSS SECTION OF ALUMINUM ROD TARGET ASSEMBLY

Fig. 4.13. The aluminum sample holder shown in cross-section illustrating the 8 sample positions and 3 beam diagonostic holes.

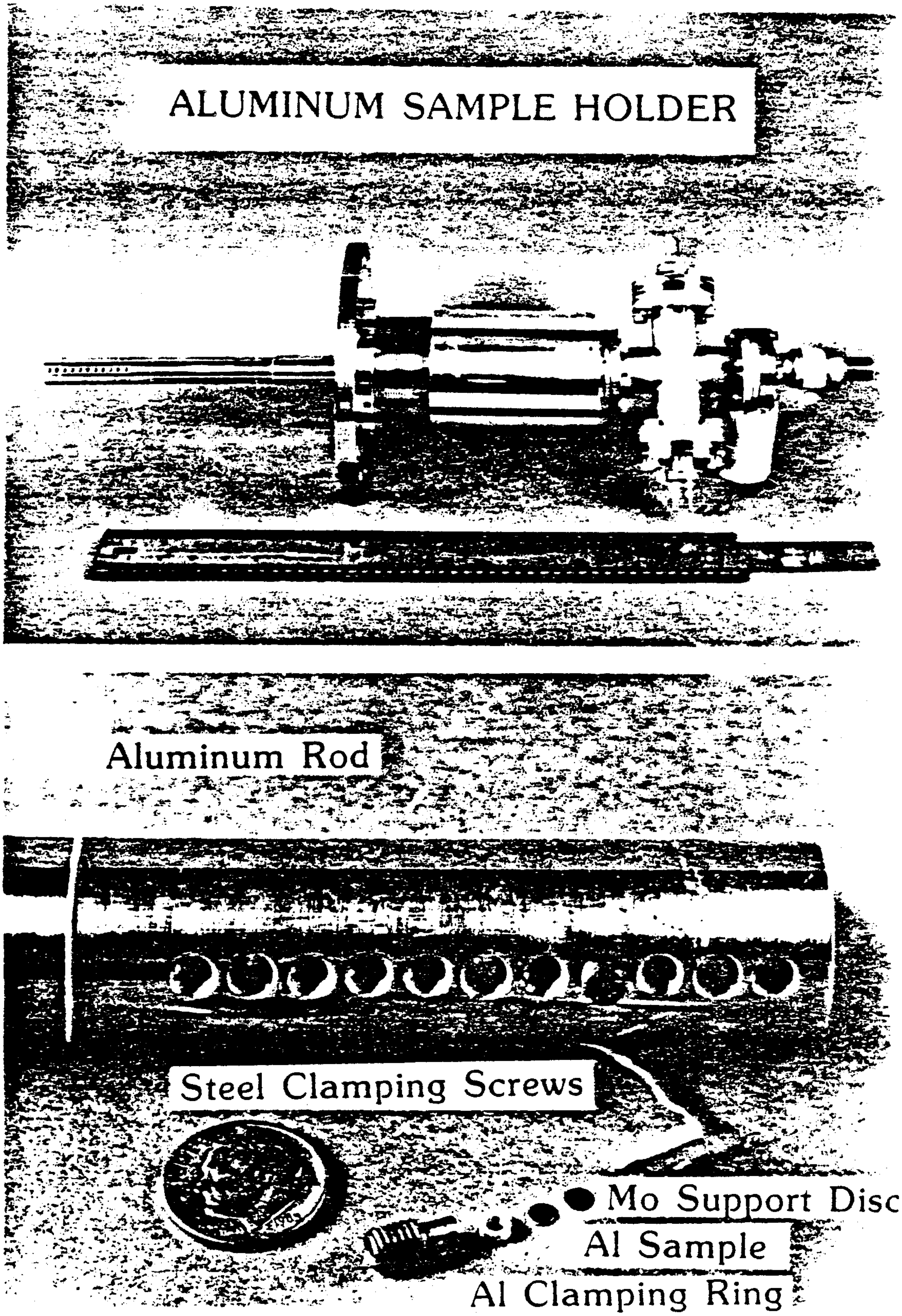

Figure 4.14 A picture of the low temperature sample holder as used for heavy ion irradiations. The top picture shows the conduction path and the bottom shows details of the sample holder.

the temperature of the sample holder. This output is compared to voltage that is set by a ten turn potentiometer and an error signal is produced. An integrator with a 20 minute time constant is used to integrate the error signal and the sum of the error signal and its time integral are applied to the power amplifier to control a bi-directional current through the thermoelectric module. The effect of the integrator is to provide an analog memory of the current setting needed to maintain a given temperature. The time response of the temperature control requires an hour for a temperature change of 25°C and once the temperature is established, the controller keeps the temperature within 2° of the set temperature. A block diagram and electrical schematic of the thermoelectric module controller appears in Fig. 4.15.

The samples were mounted in a sandwich arrangement as shown in Fig. 4.16. The aluminum sample was held by a threaded steel ring and a aluminum clamping collar and supported on the back side by a molybdenum disk. The temperature of an assembly was monitored from the back of the molybdenum disk by an insulated chromel alumnel thermocouple. The large thermal mass of the sample holder and the low resistance conduction path between the sample and the holder kept the temperature to within 2° of the initial value and all thermocouples indicated the same value. Positions for eight samples were provided as shown in Fig. 4.13, along with three beam diagnostic holes. The samples were positioned by a large hollow screw surrounding the vacuum bellows. A thrust bearing supported the force of the atmos-

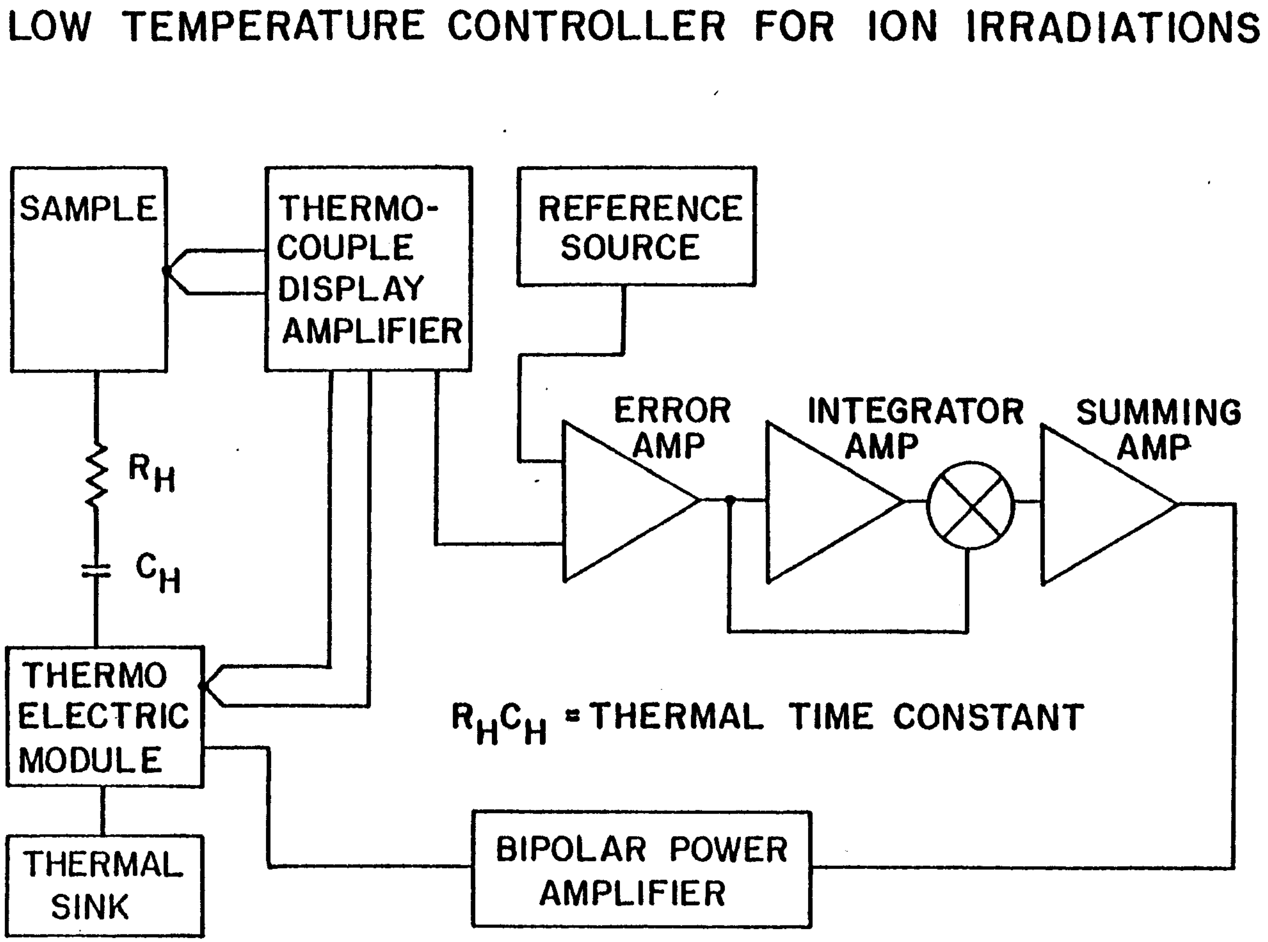

Fig. 4.15. A block diagram of the thermoelectric temperature controller shows the generation of error signals from the inputs of temperature and control setting. The error signal is amplified and integrated and the sum of the error signal and its time integral are amplified to power the thermoelectric module and control the flow of heat.

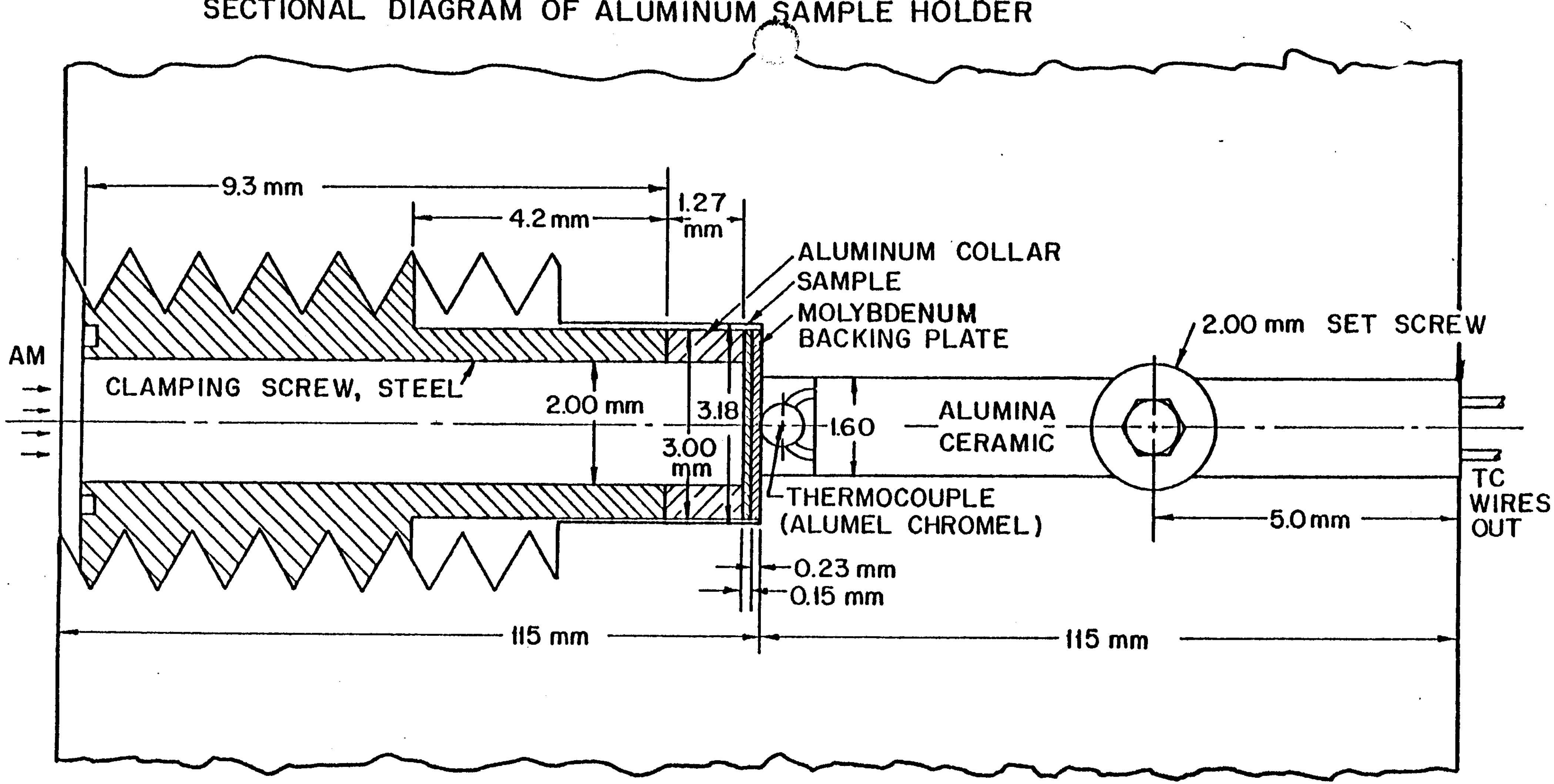

Figure 4.16 A schematic of the aluminum sample holder. The insulated thermocouple monitors the temperature of the molybdenum disk. Bombarding ions enter through the hollow screw and strike the aluminum sample. Heat is conducted away by the aluminum collar and the molybdenum disk by clamping to the major mass of the sample holder.

phere and allowed the rotation of the screw. A telescope provided visual alignment of the sample with the beam defining apertures prior to each sample irradiation. The beam diagnostic holes allowed the determination of the charge state of the beam and accurate measurement of the beam current. The charge state determination is made by scattering beam particles ninety degrees off of a gold foil into a silicon barrier detector where the deposited energy produces an electrical current. The schematic of the charge state and sample holder configuration is shown in Fig. 4.17 and the charge state measuring apparatus is described in reference (4.16). The charge state spectrum for an aluminum run is shown in Fig. 4.18 and demonstrates the very good beam purity.

E. Post Irradiation Sample Storage

The irradiated samples were transferred from the high vacuum environment of the irradiation sample chamber to a cold desiccator. The desiccator used calcium sulfate as the desiccant and the desiccator was stored in a freezer at -20°C until sample preparation. Room temperature is 0.3 T_m for aluminum as shown in Fig. 4.19 and the freezer keeps the samples at 0.27 T_m.

F. Irradiated Sample Preparation

Ion irradiated samples can be prepared for examination in the TEM by two approaches. The standard or conventional approach is to remove material from both sides of the specimen to a certain depth and examine the 0.3 to 0.6 μm thick foil microstructure at this depth. This technique yields 10,000 to 20,000 square micrometers of

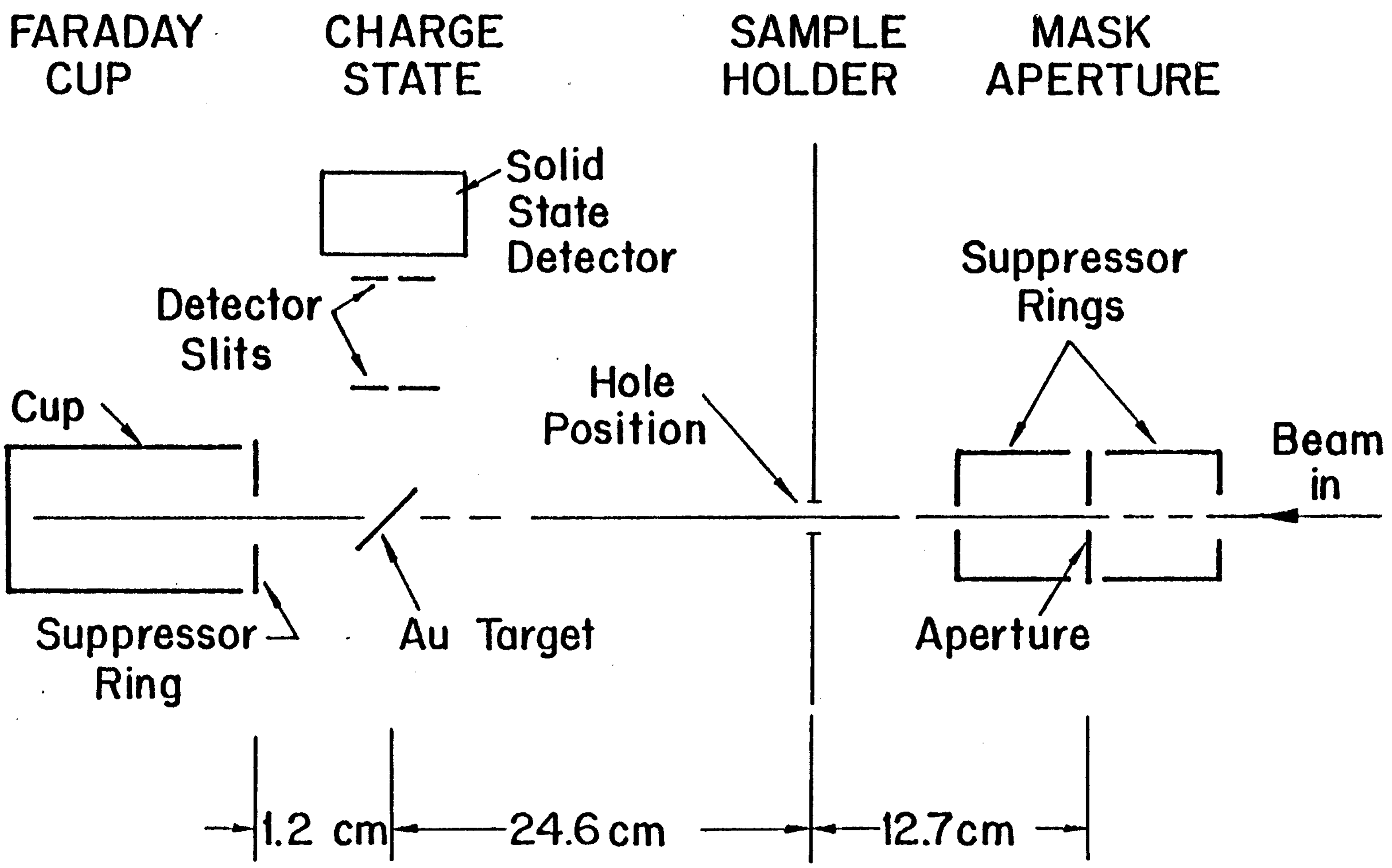

Figure 4.17 A schematic view of the sample holder and the beam diagnostic instruments.

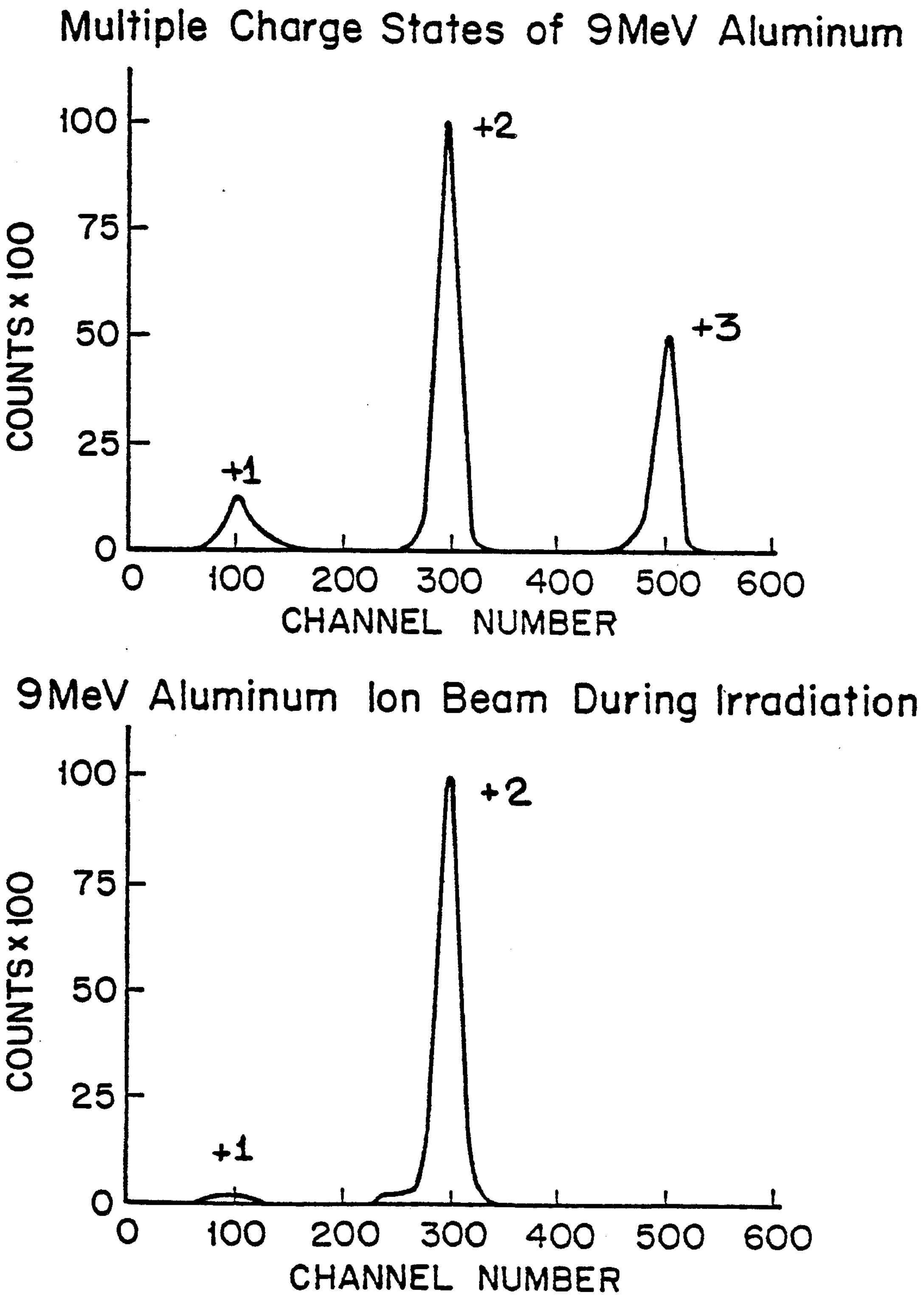

Figure 4.18 Charge state spectrums for aluminum ions at 9 Mev. The charge states are 1+, 2+, and 3+. A 2+ charge state was used as shown for the irradiations.

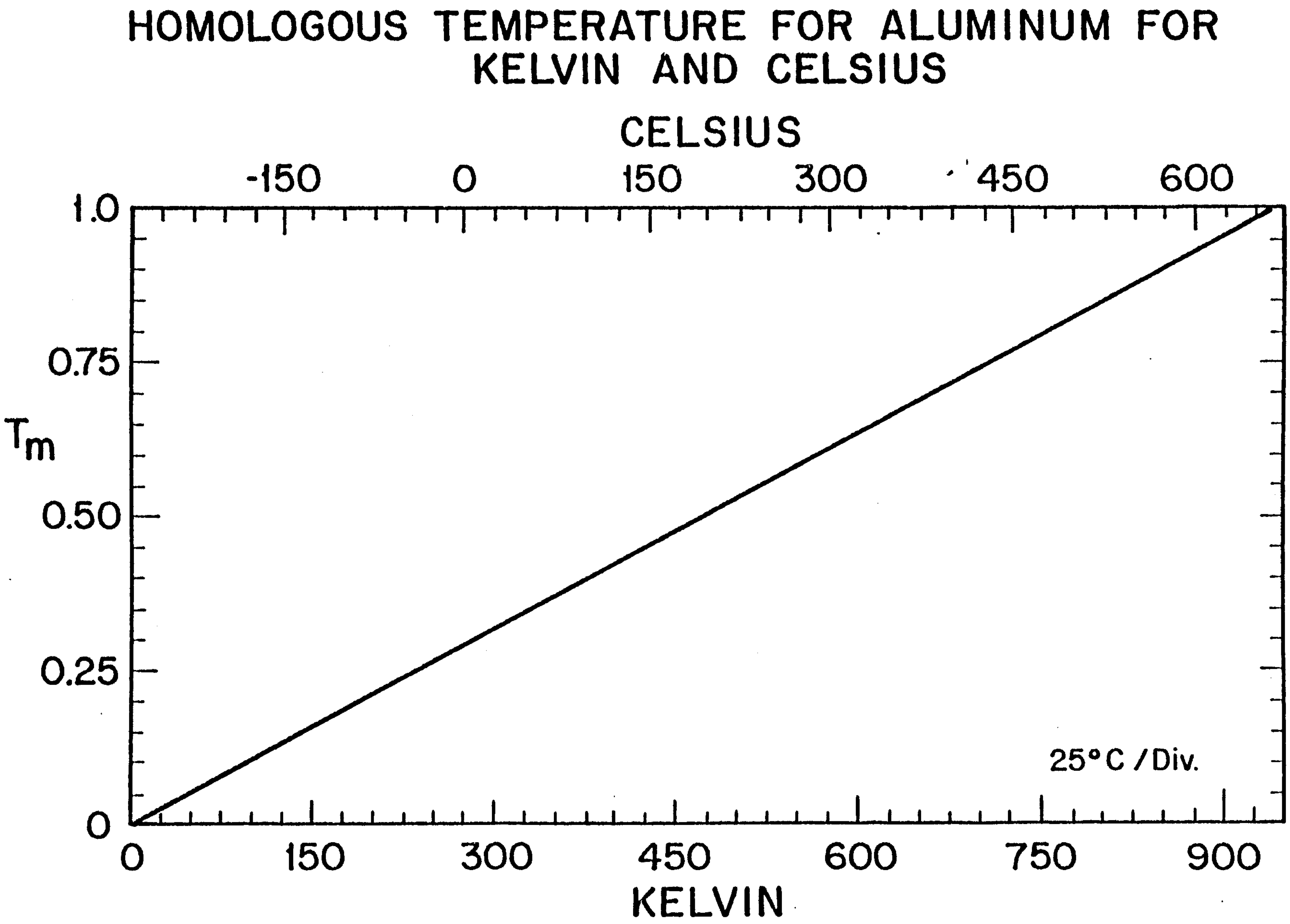

Figure 4.19 A graph of the homologous temperature as for aluminum in terms of Kelvin and Celsius temperature. The melting temperature of 660 degrees C was used for high purity aluminum.

microstructural information at the depth but material above and below the foil is removed and lost. Another technique is to examine the foil in the cross section or transverse mode to observe the damage along the path of the bombarding ion. This technique has provided information as a function of the depth of the foil for other studies in nickel, vanadium, and copper. A technique of electroplating aluminum with aluminum was developed (see Section H in this chapter) for cross section analysis of aluminum but the quality of the bond between the sample and the electrodeposit was poor.

All the irradiated samples were prepared by the conventional back-thinning technique. The cross section method required an adhesive material compatible with electropolishing to produce a suitable TEM foil. The process of electroplating aluminum on aluminum was attempted and electrodeposits of aluminum were obtained but the bonding between the aluminum sample and the electrodeposited material was unsatisfactory for electropolishing. The transverse analysis technique was abandoned since the aluminum electrodeposits would not adhere to the aluminum oxide coating and efforts to modify the surface oxide to make the material adherent were unsuccessful.

F.1 Irradiated Aluminum Sample Surface Removal

Irradiated aluminum samples were removed from the dry cold storage by warming to room temperature in a large desiccator box at room temperature. Efforts were made to keep the aluminum samples as dry as possible. The surface removal of ~ 3 μm to the region of analysis (as shown in Fig. 4.11) was accomplished with electropolishing in a 5-10% perchloric acid solution with 95-90% ethyl alcohol. The 3 mm sample was held by a polishing jig made from a pair of stainless steel tweezers. The tweezers served the dual purpose of mechanically supporting the sample and providing electrical contact between the sample and the power supply. The elecropolishing sample holder for surface removal with an aluminum disk is shown in Fig. 4.20. The irradiated sample and the electropolishing holder were coated with a protective lacquer(4.17) except for a square area that defined the irradiated area of the sample.

An Erlenmeyer flask with observing windows was used to hold the electropolishing holder, the stainless steel cathode, a thermometer, and the electropolishing solution. The Bollman technique(4.18) was used to define the geometry of the electropolishing cell. The Bollman principle uses a point cathode source to reduce field line concentration at the boundary between the sample and the stop off lacquer. The electropolishing was performed at temperatures of -30 to -50°C with a static solution and a stereo microscope at 25 power was used to observe the polishing surface condition. A switch was used to interrupt the polishing current when bubbles formed and a two channel strip chart recorder monitored the current and voltage during the polish. A current limited and voltage controlled power supply(4.19) was used to define the saturation or maximum currents and voltages used during the electropolishing. The current was integrated by a digital current integrator(4.20) to provide a real time determination of the depth of the surface removal.

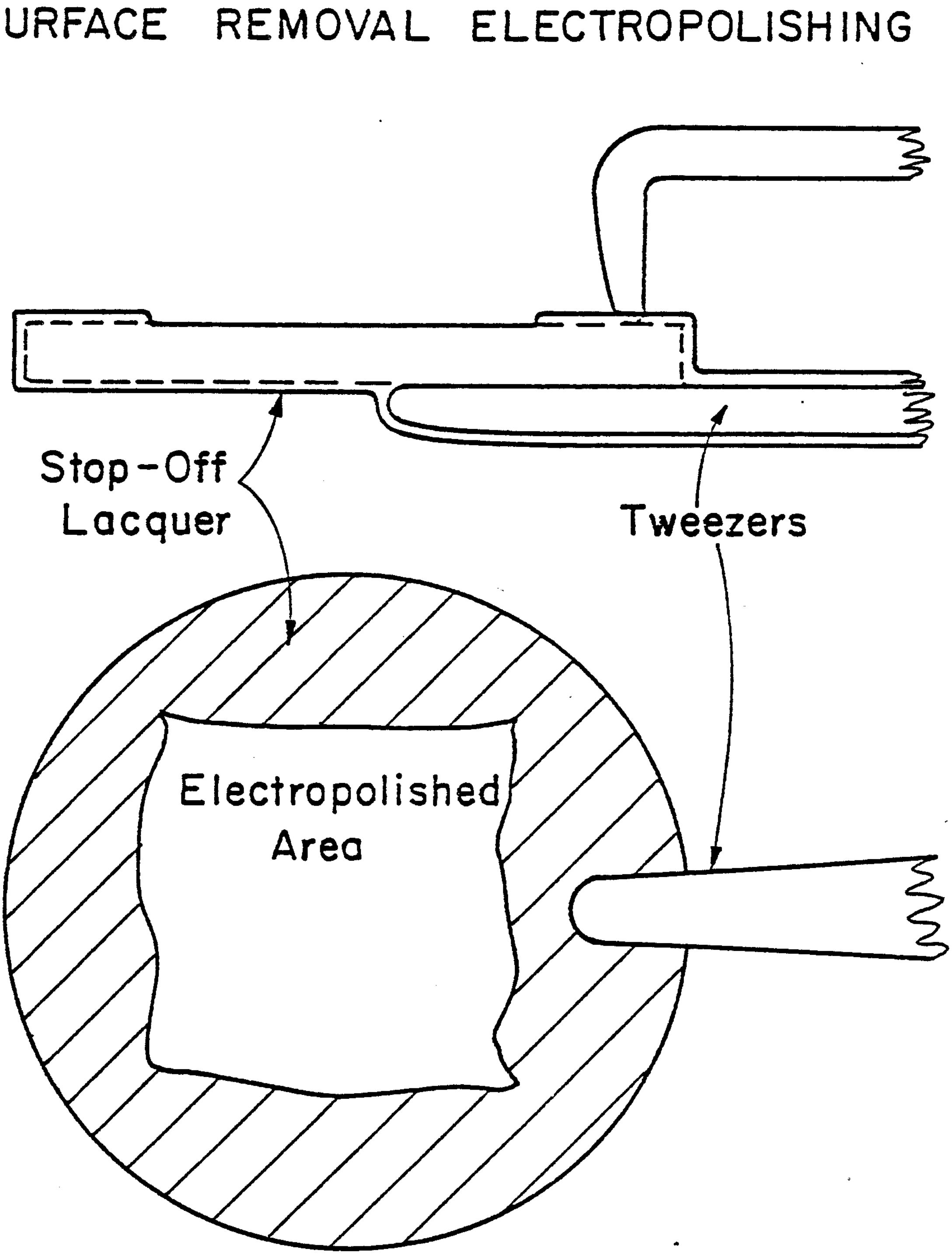

Fig. 4.20. The surface of the irradiated aluminum was removed by grasping the sample with the tweezers and electropolishing the exposed area in an solution of perchloric acid in ethyl alcohol.

Electropolishing high purity aluminum in perchloric based polishing solutions presented no major problems except when the material has been irradiated with an ion beam. The ion beam apparently modifies the surface and the irradiated material can resist electrochemical attack. The resistance to electropolishing increases the initial voltage needed to initiate electropolishing from 7 volts to more than 100 volts. The electropolishing must be done with a controlled current since the current available at 100 volts will cause extensive pitting.

The amount of material removed can be determined by two methods. A measurement of the step height can be made by an interference microscope(4.21) where the number of light fringe shifts can be measured and the shift is related to the depth by each fringe representing 0.295 μm. A depth of 3 μm is desired in aluminum ion irradiated aluminum and this corresponds to 10 fringes. The fringe count has an uncertainty of one fringe so the error in depth is 10%. This approach has been used by Weber,(4.22) Liou,(4.23) Lott,(4.24) and Knoll(4.25) to determine the depth of sample removal. This technique involves electropolishing for a predetermined amount of time and then measuring the amount of material removed.

The erratic and pulsing current used to electropolish aluminum made the use of predetermined time polishing impossible to use. A method of real time measurement of the sample depth was developed and used. The amount or volume of material removed is the product of the area and the depth. The area was determined from height and width measured to the nearest 0.04 mm and the total volume of material removed was related by charge conservation. The integrated current and the volume were equal when each aluminum atom removed used two electrons. The area was measured and number of microcoulombs needed for a three micrometer depth was given from the relation

$$\text{Total Counts} = 56{,}710 \times \text{Area}$$

where the total counts is in microcoulombs and the area is expressed in square millimeters. This technique allows a significant improvement in the accuracy of depth removal from ±10% to ±4% where the errors involved are from the area measurement. Figure 4.21 shows the sample surface removal setup used for electropolishing aluminum to a 3 μm depth.

F.2 Irradiated Aluminum Sample Final Thinning

The irradiated aluminum samples were thinned for examination in the transmission electron microscope by using a commercial jet thinner.(4.26) The jet thinning produces a dimple polish profile that produces a wedge of thin material suitable for transmission electron microscope examination. The jet thinner is equipped with a automatic shutoff circuit that stops the thinning once a set amount of light is detected.

The electropolishing solution used for the final thinning of aluminum used 10% perchloric acid in 90% methyl alcohol. The current was 10 to 20 mA while the voltage was 25 to 50 volts. Both the

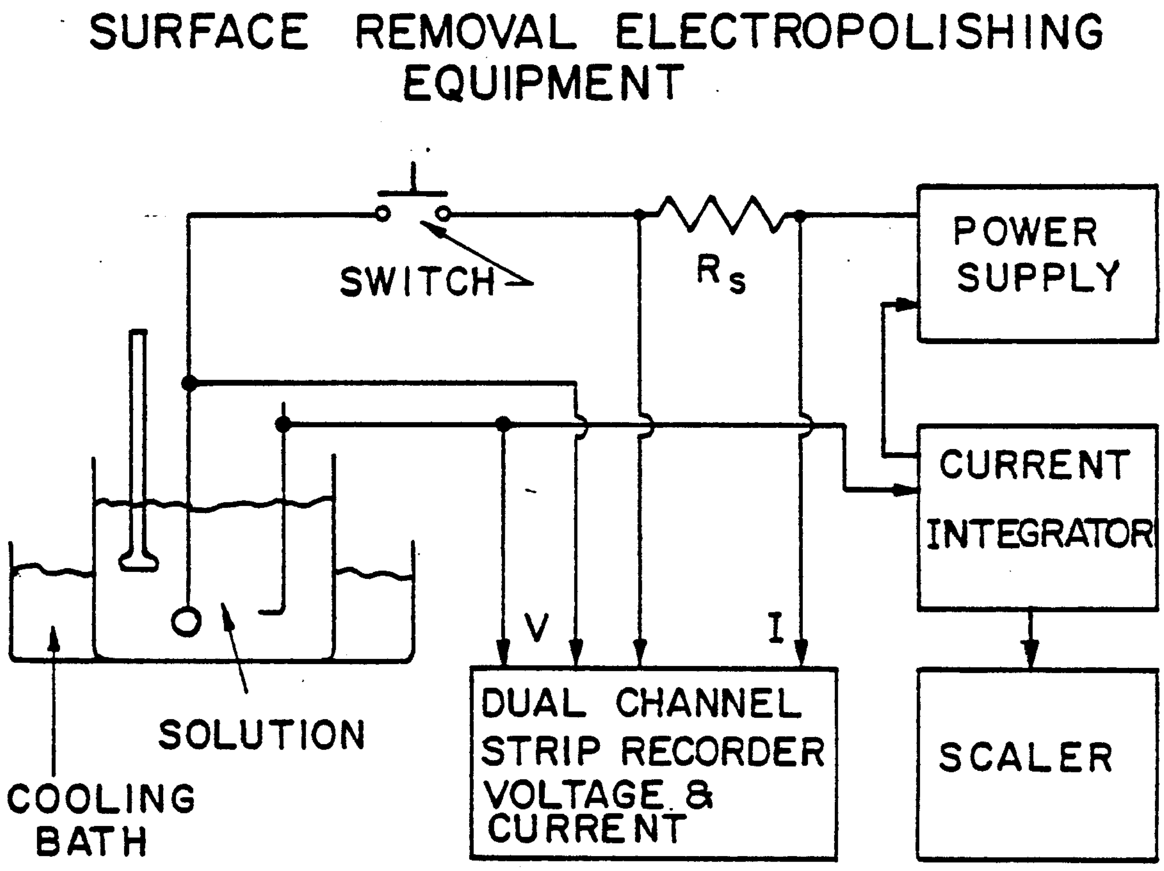

Fig. 4.21. Surface removal of the irradiated aluminum samples was performed with the polishing equipment while the voltage and current was recorded.

current and voltage were sensitive to the temperature and the best results were obtained at temperatures below -40°C. Liquid nitrogen was used to provide cooling and was preferred to dry ice (solid carbon dioxide) since the polishing solution would saturate with carbon dioxide gas and cause pump cavitation. Pump cavitation would reduce the pumping of the polishing solution and the jetting action would cease. Nitrogen was not observed to interfere with the operation of the pump and provided effective control of the temperature. The final thinning polishing conditions had a wide latitude for temperature, voltage, and current and either voltage controlled polishing or current controlled polishing produced equally good results. Most of the samples were thinned at -50°C with 10 mA of current and the voltage ranged from 20 to 30 volts during the polish. The light sensitivity was adjusted to give a hole of 50 to 100 µm in diameter with a 50 to 100 µm halo of thin area surrounding the hole.

The foil was thinned by applying stop-off lacquer to protect the three micrometer deep removed surface and jet thinned from the back side. The condition of the foil prior to final thinning was important to the final flatness of the thinned foil. The final thinning concentrated any bending stresses and the thin foil would shear under tensile stresses and buckle under compressive stresses. Figure 4.22 illustrates the two mechanisms of compression and tension stress concentration for a thinning foil. The protective lacquer coating also provided extra strength and support for the thin area during the final jet electropolish where the foil was exposed to the thrust

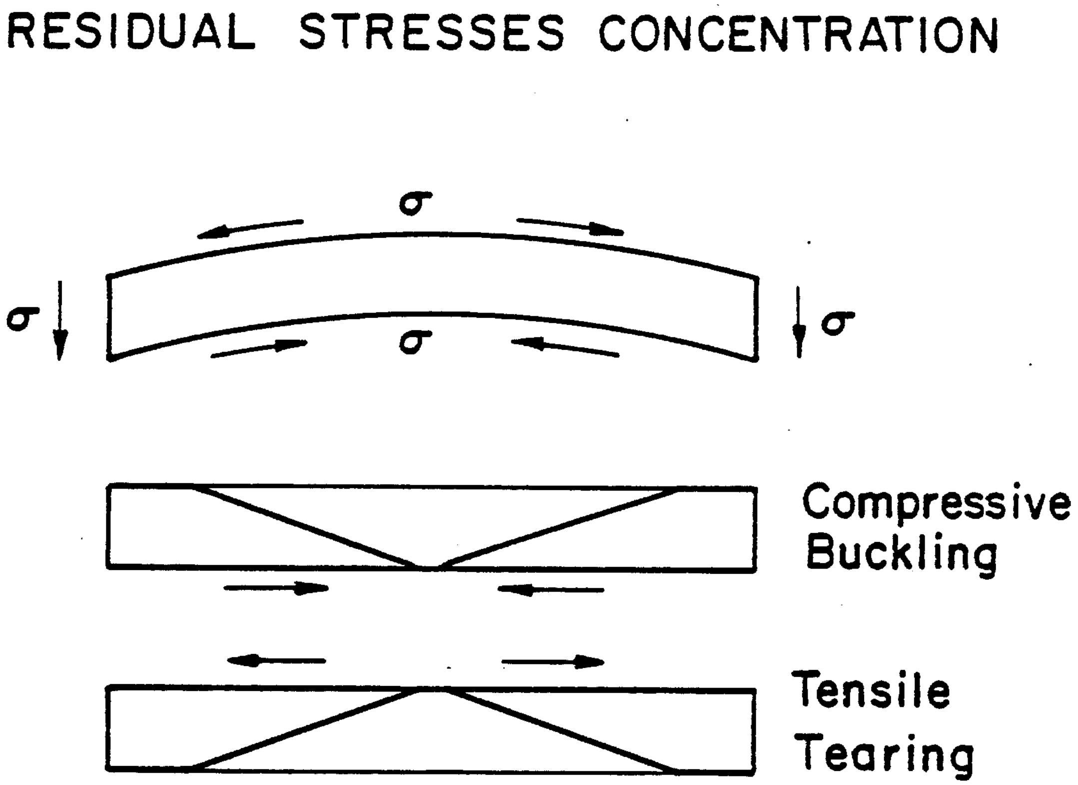

Fig. 4.22. The final thinning of aluminum can concentrate residual stress in the sample. The aluminum disk is shown in cross-section with a cone of material removed from the disk and the stress will exceed the yeild stress of the aluminum before it reaches the center. The stress can be compressive or tensile depending on the direction of bending before polishing started.

force of the impinging electropolish jet. The protective lacquer was removed by dissolution in acetone and any stresses relieved by the stop-off lacquer were removed as the lacquer dissolved. Irradiated samples were washed in acetone and methyl alcohol several times and stored in a room temperature desiccator until examined in a transmission electron microscope.

G. Transmission Electron Microscope Analysis

The analysis of the irradiated specimens was performed in a JEOL 100B transmission electron microscope operated at 120 kilovolts and some analysis was done in an AEI EM7 operated at 1000 kilovolts. The samples were oriented in the microscope with the irradiated surface facing the phosphor screen and all micrographs were analyzed with the emulsion side up.

The foil thickness determinations were done by stereo microscopy using a known tilt angle and a parallax measured on a Hilgar Watts stereo viewer.(4.31) The foil thickness is determined by

$$t(\text{nm}) = \frac{p(\text{mm}) \times 10^6 \ (\text{nm/mm})}{2\ M \sin(\theta/2)} \tag{4.2}$$

where the thickness is expressed in nanometers, M was the magnification of the print being analyzed, and theta was the total tilt angle in degrees. p(mm) is the parallax measurement reading obtained from the Hilgar Watts and is measured to the nearest 0.01 mm. The foil thickness determinations were done at optimum angles as described by Hudson(4.32) and the tilting procedures used minimized the

LOOP ANALYSIS FACTORS

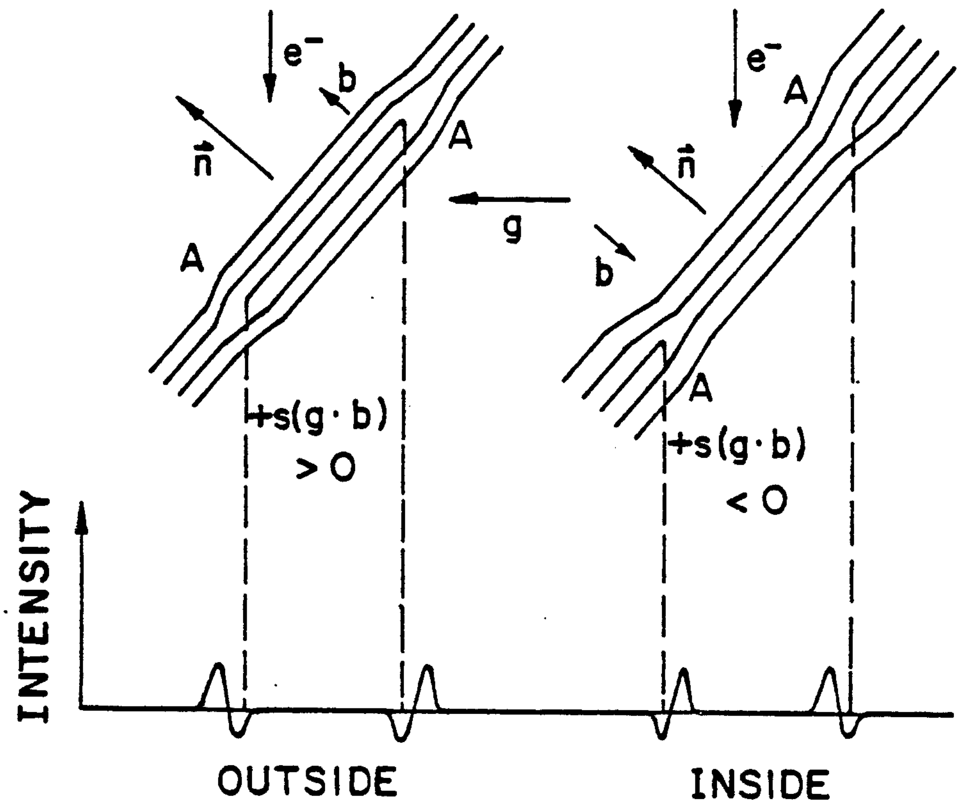

Figure 4.23 The principle of loop analysis is illustrated(Ref 4.34). Electron diffraction shifts the diffraction beam to one side of the dislocation core according to the direction of the diffracting beam. Reversing the diffracting beam shifts the diffraction image to the opposite side of the dislocation core. The diffraction image is typically 3 nanometers wide and the shifts are typically 6 nanometers.

errors as discussed in Ref. (4.33). The Hilgar Watts stereo viewer was calibrated with drawings of a known parallax and foils of 300 to 500 nanometers thickness were typical with the 300 giving the best void imaging conditions in low contrast pictures. The electropolishing process produced surface features which were used to measure the parallax. Samples containing voids which had intersected the surface were also used to measure the foil thickness.

The loop analysis techniques(4.34) used the principle of inside and outside contrast to determine the vacancy or interstitial nature of the loops as described in Fig. 4.23. The technique used was developed by Tjhia(4.35) and is the same, with one minor difference, as proposed by Eyre.(4.36) Tjhia suggested the unsafe analysis condition proposed by Eyre involved a sign change and could be accounted for in the analysis. A dislocation loop consists of a burger's vector and a loop plane normal. The inside/outside contrast is determined by the $\vec{b} \cdot \vec{n}$ product of these two values. When the burger's vector or the loop normal change sign, then Eyre described this area of the stereo projection as unsafe, since a straight forward application of loop analysis would indicate the wrong type of loop.(4.37) Figure 4.24 illustrates the principle of safe and unsafe conditions. Both safe and unsafe conditions were used in the analysis since the sign of the loop normal was used to determine the vacancy or interstitial nature of the loops.

Imaging of the voids or cavities used the underfocus condition to image the voids. The underfocus also caused bright fringes that

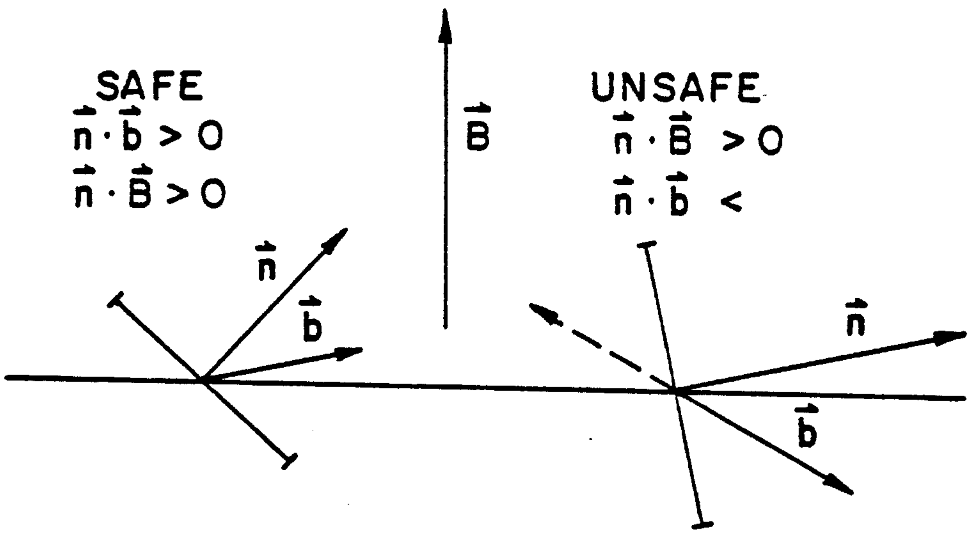

Figure 4.24 Loop analysis can be done for both safe and unsafe conditions if the product of the loop plane normal and burgers is known. The condition where the product changes from an up or positive value to a down or negative is used to interpret the inside/outside contrast results and determine the interstitial or vacancy nature of the dislocation loops.

delineate the edges of the void as seen in micrographs in Fig. 5.22 and described by Foreman.(4.38) The void volume for an octahedral void is

$$V = \sqrt{2}/3\ a^3 \tag{4.3}$$

where a is the void edge length as shown in Fig. 4.25. An octahedral void appears in a number of shapes as illustrated in Fig. 4.25 and the sizing of the void image used corrected values to determine the void volume. The measurement of the void size was made by a Zeiss particle analyzer and the circular projection of the analyzer was matched to the side distance of the octahedral void. The void volume could then be calculated by using the particle size results without further manipulation or corrections. The Zeiss comparator records the void sizes into j classes and the number of voids in a class size was corrected for the fraction that would intersect the foil surface using

$$n_j' = n_j \frac{t}{(t - d_j)} \tag{4.4}$$

where d_j was the void size of class j, n_j the uncorrected void count, and n_j' the corrected void count for class j. The average void size d was determined by

$$\langle d \rangle = \sum_j \frac{n_j' d_j}{N} \tag{4.5}$$

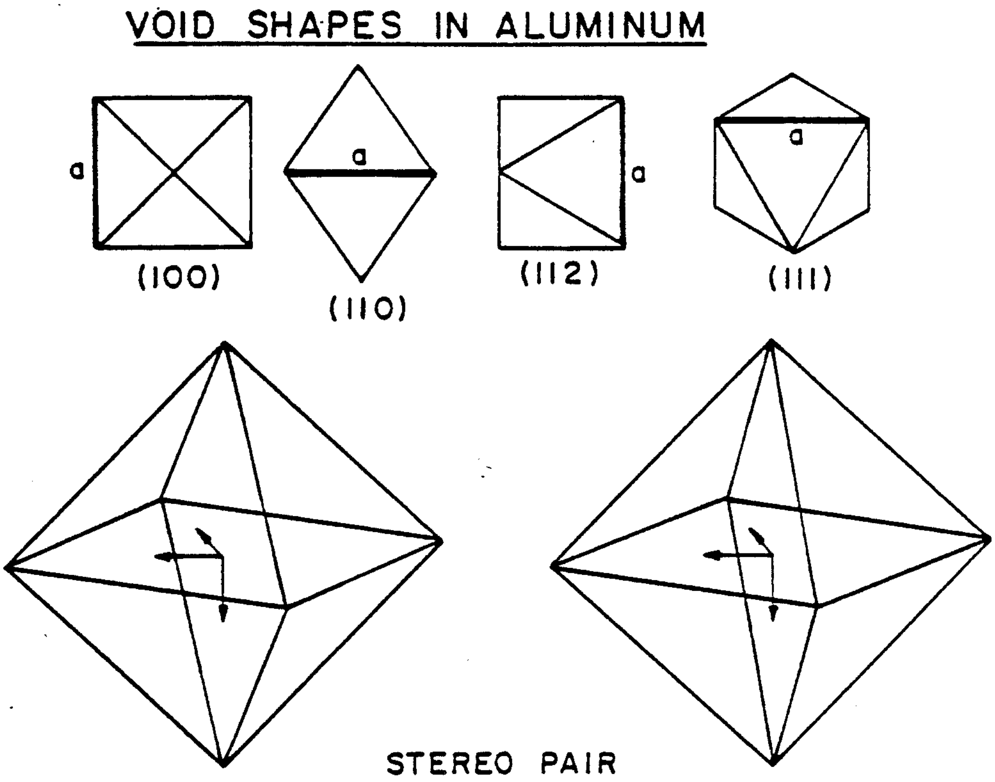

Figure 4.28 - Projections of octahedral voids in face centered cubic materials are shown for the three low index directions <001>, <011>, and <111> in the transmission electron microscope. A computer drawn stereo pair is shown for 3-dimensional viewing of the void shape.

where N is the total sum of n'_j voids. The swelling was given by the summation of the n_jV_j classes as

$$\frac{\Delta V}{V} = \frac{1}{V} \sum_j N'_j \frac{\sqrt{2}}{3} d_j^3 \qquad (4.6)$$

where V' was the foil volume analyzed.

H. Electroplating Aluminum

A method of examining ion irradiated aluminum along the ion pathlength by electroplating with aluminum and sectioning the electroplated sample to obtain a number of foils for transmission electron microscope samples was investigated. The chemical activity of aluminum required an electroplating solution based upon a solutions free of water and an electroplating bath of aluminum chloride in ethyl ether was selected since this solution had been used more frequently by a number of authors.(4.27)

The electroplating solution consisted of aluminum chloride, diethyl ether, and lithium aluminum hydride. The aluminum chloride supplied the source of aluminum metal ions, the ether was the solvent and the lithium aluminum hydride absorbed any traces of water vapor. The chemicals were anhydrous and the entire experimental plating process was done in a glove box containing an argon-nitrogen gas atmosphere free of oxygen and water vapor.

The aluminum chloride was refined by a three pass sublimation to remove impurities.(4.28) A 300 ml electroplating solution consisted of 136 grams of anhydrous aluminum chloride with 120 ml of a 1 molar solution of lithium aluminum hydride in ethyl ether with anhydrous ethyl ether added to make the 300 ml solution. Commercial purity 1100 grade aluminum anodes 1 cm in diameter and 5 cm long were used to replenish the aluminum in the electrolyte. The electroplating was sensitive to forming whiskers or trees of aluminum which would short out the electroplating cell. A periodic reverse current(4.29) was used to reduce the formation of aluminum trees and provide a smooth aluminum electrodeposit. Electroplating was done at room temperature with 50 mA of forward current for 160 seconds followed by a reverse current of 50 mA for 16 seconds. The voltage ranged from 5 to 20 volts during the forward and reverse cycles and the ether evaporation rate required fresh ether every five hours. The electroplating current density was 20 mA per square centimeter forming an electrodeposit at a rate of 25 μm per hour and appeared very nodular. A sample of the electrodeposit is shown in Fig. 4.26 achieved with the aluminum chloride and ethyl ether electroplating bath.

The electrodeposit did not adhere very well to the aluminum oxide coated sample surface. Separate attempts to removed the aluminum oxide surface were made by a strike or reverse electroplate and a commercial zincating(4.30) surface preparation. The reverse electroplate and strike did not improve the adhesion between the electrodeposit and the aluminum substrate. The commercial zincating process to electroplate aluminum with other metals used a layer of zinc metal to form the interface between the electrodeposited metal and the aluminum, replacing the aluminum oxide layer. The zincation tech-

ELECTROPLATED ALUMINUM

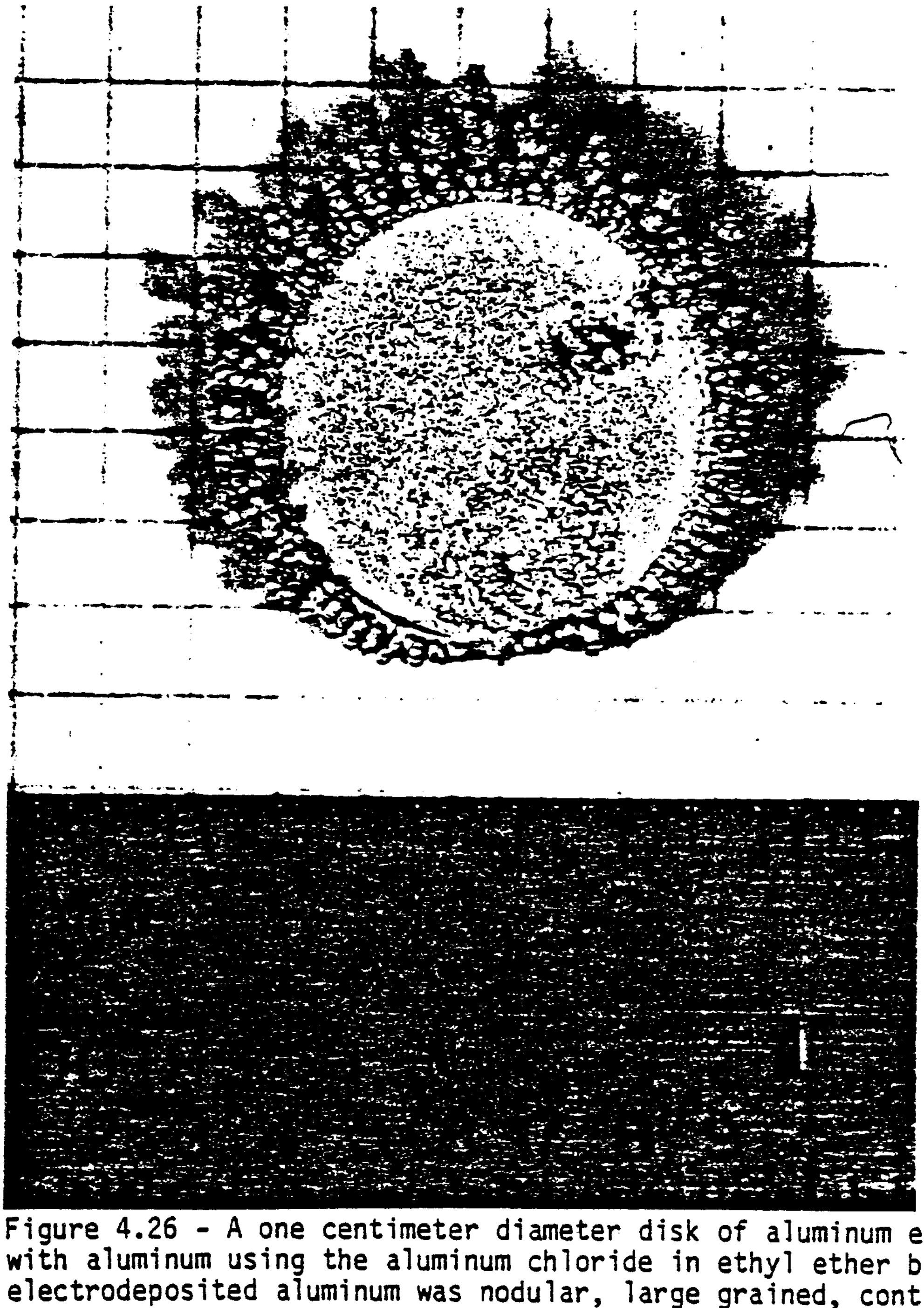

Figure 4.26 - A one centimeter diameter disk of aluminum electroplated with aluminum using the aluminum chloride in ethyl ether bath. The electrodeposited aluminum was nodular, large grained, contained holes, and weakly bonded to the aluminum disk.

nique was used to remove the aluminum oxide layer by chemically replacing the aluminum oxide layer with a aluminum-zinc alloy. The zincating solution was made from 300 grams of sodium hydroxide, 75 grams of zinc oxide, 6 grams of copper cyanide, and 170 grams of potassium cyanide in one liter of water. Aluminum metal was immersed in this solution and a friable deposit of Al_xZn_y plus Zn was deposited where the x and y represent a variable composition of aluminum and zinc. The zinc is removed by a controlled solution at 20°C in a mixture of 3 volumes nitric acid, 1 volume of hydrofluoric acid, and 4 volumes of water without attacking the Al_xZn_y. Another nonfriable or dense coating of zinc metal was again deposited by returning the sample to the zincating bath. The process worked for commercial purity aluminum but the high purity material would take the zinc metal only on certain grains of aluminum. A scanning electron microscope micrograph of the zincated high purity aluminum is show in Fig. 4.27 where the hexagonal zinc metal is located only on certain aluminum grains. The zinc crystals are oriented with their basal planes close to the aluminum foil surface. The close packed planes of aluminum and zinc are comparable in atom to atom distance and zinc atoms were believed to attach only to those aluminum grains that presented a low angle close packed plane to the zinc basal plane.

The effort to produce cross section aluminum samples was finally abandoned since the electroplated aluminum would not adhere to the aluminum. The aluminum oxide layer presented a major problem to the formation of adherent aluminum electrodeposits.

ZINCATED HIGH PURITY ALUMINUM

Figure 4.27 A scanning electron micrograph of the zincating material reveals the hexagonal nature of the zinc electroless deposit. The chemical activity of the aluminum drives the reaction to replace the aluminum with zinc metal. The close packed atom planes of the FCC aluminum and HCP zinc are closely matched.

REFERENCES FOR CHAPTER 4

4.1 N.H. Packan, Voids in Neutron Irradiated Aluminum, Ph.D. Thesis, University of Missouri (1971).

4.2 M.L. Sundquist and J.M. Donhowe, Nucl. Tech. 30 (1976) p. 4.

4.3 W.J. Yang, R.A. Dodd, and G.L. Kulcinski, "Electron Irradiation Damage in High Purity Aluminum," J. of Nuclear Materials 64, 157-166 (1977).

4.4 Reference 4.1, pp 38-39.

4.5 W.V. Green, S.L. Green, B.N. Singh, and T. Leffers, "Effects of High Helium Production Rate on Microstructural Evolution in Aluminum During 600 MeV Proton Irradiation," J. Nucl. Mat. 103 & 104, 1221 (1981).

4.6 Ernest F. Fullam, Inc., 3 mm Hand Punch, Cat. No. 1178, 900 Albany Sheher Rd. Latham, NY 12110.

4.7 Buehler Ltd., Handimet Grinder, Cat. No. 39-1471, 3120 Greenwood Street, Evanston, IL 60204.

4.8 Michigan Chrome & Chemical Co., Microstop and Microshield STOP-OFF LACQUER, 8615 Grinnell Avenue, Detroit, MI 48213.

4.9 Syntron A Division of FMC Corp., Model LP01 Vibroratory Polishing Machine, Homer City, PA 15748.

4.10 Personal Communication with Jim Nelson at Buehler, 16 September 1976 (p. 25 LOG I).

4.11 W.J. Weber, Heavy-Ion Induced Void and Loop Formation in High Purity Vanadium, Ph.D. Thesis, University of Wisconsin (1977), p. 76-80.

4.12 N.H. Packan and W.A. Coghlan, "Injecting Irradiation Samples with a Uniform Concentration of Helium using Curium-242," Nuclear Tech. 40, 208-213 (1978).

4.13 H.V. Smith, Jr. and H.T. Richards, Nucl. Instr. and Meth. 125, 497 (1975).

4.14 G.T. Caskey, R.A. Douglas, H.T. Richards, and H. Vernon Smith, Jr., "A Simple Negative-Ion Sputter Source," Nucl. Inst. and Meth. 157, 1-7 (1978).

4.15 H. Vernon Smith, Jr. and R.G. Lott, "A High Temperature, Ultra High Vacuum Facility for Heavy Ion Simulation of Neutron Radiation Damage to Potential Reactor Materials," Nucl. Inst. and Meth. 143, 125-132 (1977).

4.16 J.M. Freeman and B.W. Hooton, Nucl. Instr. and Meth. 111, 501 (1973).

4.17 Michigan Chrome and Chemical Company, Microshield and Microstop Stop-off Lacquers, 8615 Grinnell Ave., Detroit, Michigan 48213.

4.18 W. Bollman, Phys. Rev. 103, 1588 (1956).

4.19 Kepco Inc., Model ATE 100-0.5M, 131-38 Sanford Ave., Flushing, NY 11352.

4.20 EG&G ORTEC, Model 439 Current Integrator, 100 Midland Rd., Oak Ridge, TN 37830.

4.21 William J. Hacker & Co., Inc., H/I Interference Microscope, Box 646, West Caldwell, NJ 07006.

4.22 W.J. Weber, Heavy Ion Induced Void and Loop Formation in High Purity Vanadium, Ph.D. Thesis, University of Wisconsin (1977) p. 89.

4.23 K.Y. Liou, Radiation Effects in Molybdenum and Molybdenum-Zirconium Alloy, Ph.D. Thesis, University of Wisconsin (1979) p. 75.

4.24 R.G. Lott, The Effect of Nickel and Nitrogen on Void Formation in Vanadium, Ph.D. Thesis, University of Wisconsin (1979) p. 89.

4.25 R.W. Knoll, Radiation Damage in Copper and Copper Beryllium Alloys, Ph.D. Thesis, University of Wisconsin (1981).

4.26 E.A. Fischonie Inst. Manufacturing, Twin Jet Electropolisher Model 110 & 120, 7925 Thon Drive, Verona, PA 15147.

4.27 D.E. Couch and A. Brenner, Electrochem. Soc. 99, 234 (1952).

4.28 The author wishes to acknowledge the advice and assistance of Prof. Ed Larson and Julie Warazel in the preparation of Aluminum Chloride. September 1977 (LOG I p. 75-85).

4.29 F.A. Clay, W.B. Harding, and C.J. Stimetz, Plating, 56, 1027-37 (1969).

4.30 American Society for Metals, Metals Handbook; Vol. 5; Surface Chemistry, Finishing and Coating, p. 604 (1982).

4.31 Rank Precision Industries Ltd., Folding Mirror Stereoscope SB/80, P.O. Box 36, Leicester House, Lee circle, Leicester, England LE19JB.

4.32 B. Hudson and M.J. McKin, "The Optimum Tilt Angle for Electron Stereo Microscopy," J. Physics E Scientific Inst. 3, 311 (1970).

4.33 J.F. Nankivell, "The Theory of Electron Stereo Microscopy," Optik 20, 171-197 (1963).

4.34 B. Edmondson and G.K. Williamson, "On the Determination of the Nature of Dislocation Loops," Phil. Mag. 9, 277 (1964).

4.35 The author wishes to acknowledge the advice of Eddy Tjhia for analysis of dislocaiton loops in aluminum.

4.36 B.L. Eyre and R. Bullough, "On the Formation of Interstitial Loops in BCC Metals," Phil. Mag. 12, 31 (1965).

4.37 G.W. Groves and M.J. Whelan, "The Determination of the Sense of the Burgers Vector of a Dislocation from its Electron Microscope Images," Phil. Mag. 7, 1603-1607 (1962).

4.38 A.J.E. Foreman, H.S. Harrach and D.K. Saldin, "The TEM Contrast of Faceted Voids," Phil. Mag. A 45 (1982) p. 625.

CHAPTER 5: RESULTS

A. Copper Ion Irradiated High Purity Aluminum

High purity aluminum samples were irradiated with copper ions at 200, 175, 150, 125, and 100°C to a nominal dose of 2 dpa at a 3 μm depth. A table of irradiated samples is shown in Table 5.1 for the copper ion irradiations of high purity aluminum. The irradiation of high purity aluminum by 14 MeV copper ions produced damage and microstructural changes. Two major results from these irradiations were a temperature effect and a copper bombarding ion effect. Dislocation density increased with decreasing temperature and the dislocation microstructure was influenced by the injected copper atoms from the irradiating copper ion beam.

In the 200°C sample, there were no dislocation loops and a few dislocation tangles. Irradiations at 200°C or 0.5 T_m produced defects which were mobile and recombined or were absorbed by rapidly climbing dislocations. The dislocation density increased with decreasing temperature from the 200°C sample to the 100°C sample.

The 175°C sample as seen in Fig. 5.1 shows a heterogeneous distribution of dislocations, dislocation loops, and faulted dislocation loops. The heterogeneous distribution of the dislocation structures is attributed to the presence of copper and the early formation of θ' structures.

The 150°C copper ion irraditated aluminum sample microstructure is shown in Fig. 5.2 and the microstructure shows long dipole loops.

TABLE 5.1. COPPER ION BOMBARDED HIGH PURITY ALUMINUM SAMPLES

Sample #	Dose (dpa)	Temperature	Comments
1-1-50	2	200	Clean foil, some disl. networks
1-2-51	2	175	Some tracks, faulted loops
1-3-52	2	150	Large long dipole loops
1-4-53	2	125	Distinct tracks and disl. groups
2-2-56	2	175	End of ion range, theta precip.
2-5-59	2	125	Dense conc. of disl. and loops
2-7-61	2	100	Dense conc. of disl. and loops

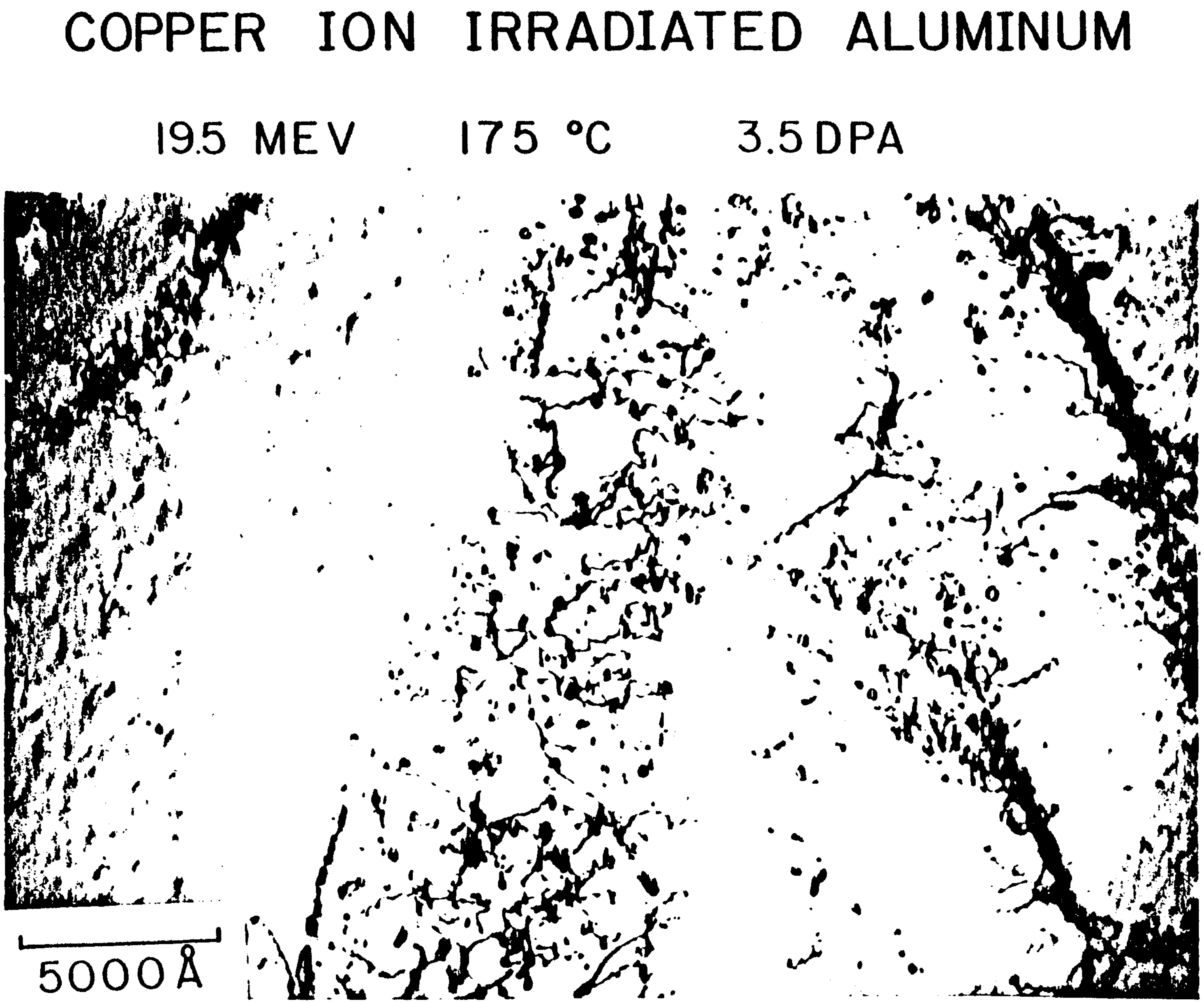

Figure 5.1 A copper ion irradiated sample shows a heterogenous distribution of dislocations, dislocation loops, and faulted dislocation loops. The heterogenous distribution of the dislocation structures is attributed to the presence of copper and the early formation of theta prime structures.

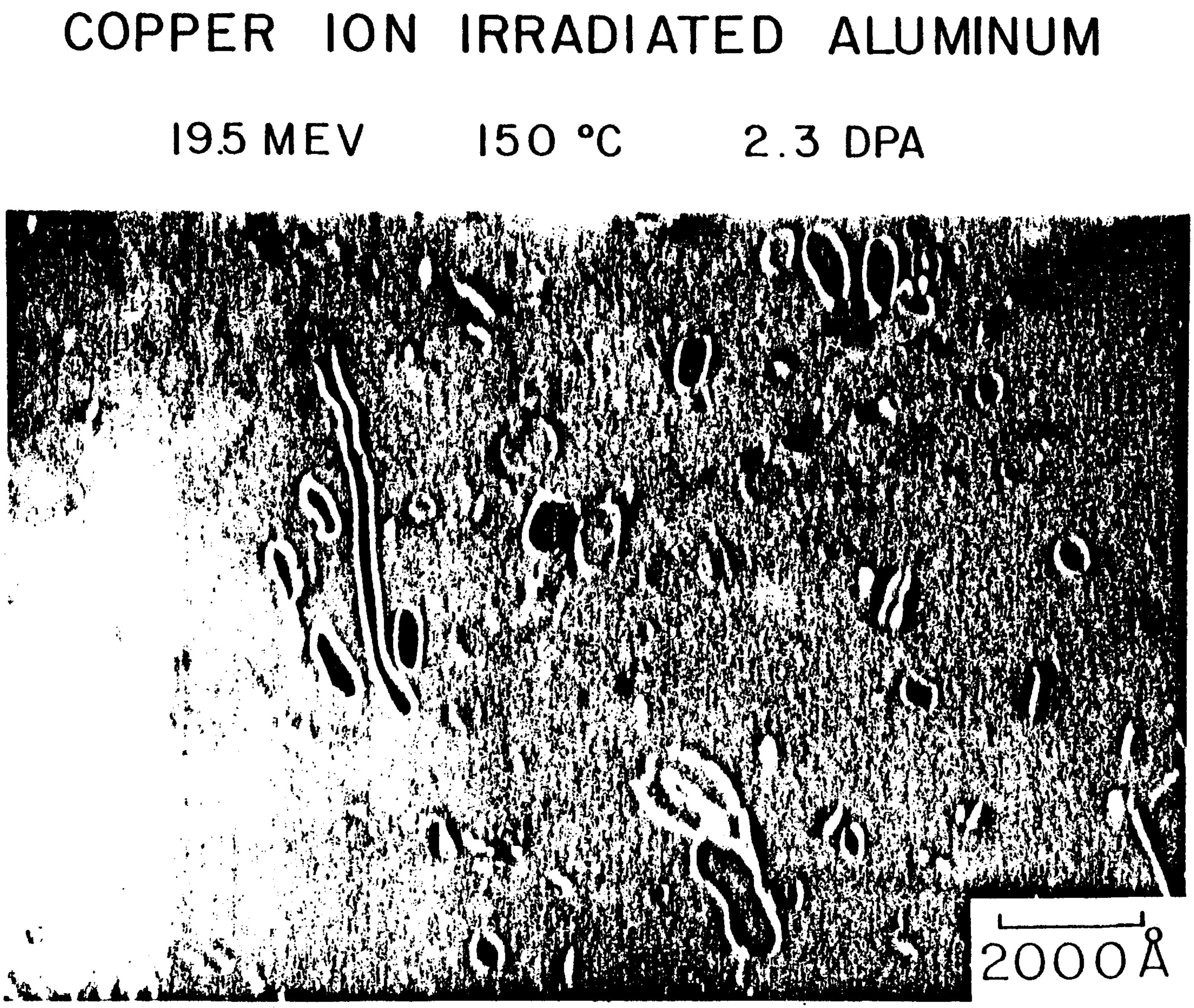

Figure 5.2 A copper ion irraditated aluminum sample microstructure shows long dipole loops. These long dipole loops are attributed to a combined effect of the copper irradiation and foil deformation.

These long dipole loops are believed to be a combined artifact of the copper irradiation and foil deformation since similar dipole structures are observed in aluminum ion irraditated aluminum as discussed in Section B.

A micrograph from a 100°C copper ion irradiated sample is shown in Fig. 5.3 and illustrates the increase in the dislocation density. The loops analyzed in this sample were essentially all vacancy type. The number of loops as a function of temperature and two representive histograms of the loop size distribution are shown in Fig. 5.4.

The end of range of the copper ions was examined and a representive micrograph of the aluminum microstructure is shown in Fig. 5.5. This sample was irradiated to 2 dpa at 3 μm and a total of 5.7×10^{15} copper atoms were injected into the normal distribution. The copper concentration in the full width at half maximum (FWHM) is 5.7×10^{19} copper atoms per cm^3 or one copper atom for every 1060 aluminum atoms. The atom percentage is 0.09% or 942 at.ppm copper in aluminum. The phase diagram for copper in aluminum shows the copper should be insoluble in aluminum at these temperatures and concentrations, and precipitates should remain stable if formed. The initial injected ion distribution is degraded by copper diffusion but a factor of 9 reduction is required to establish the solubility of copper in aluminum which is unlikely.(5.1)

Copper in aluminum precipitates into a two phase structure as seen from the phase diagram in Fig. 5.6 of aluminum and copper. The two phases are an aluminum fcc matrix and a Al_2-Cu platelet~~te~~ pre-

DISLOCATIONS AND LOOPS IN COPPER ION BOMBARDED ALUMINUM

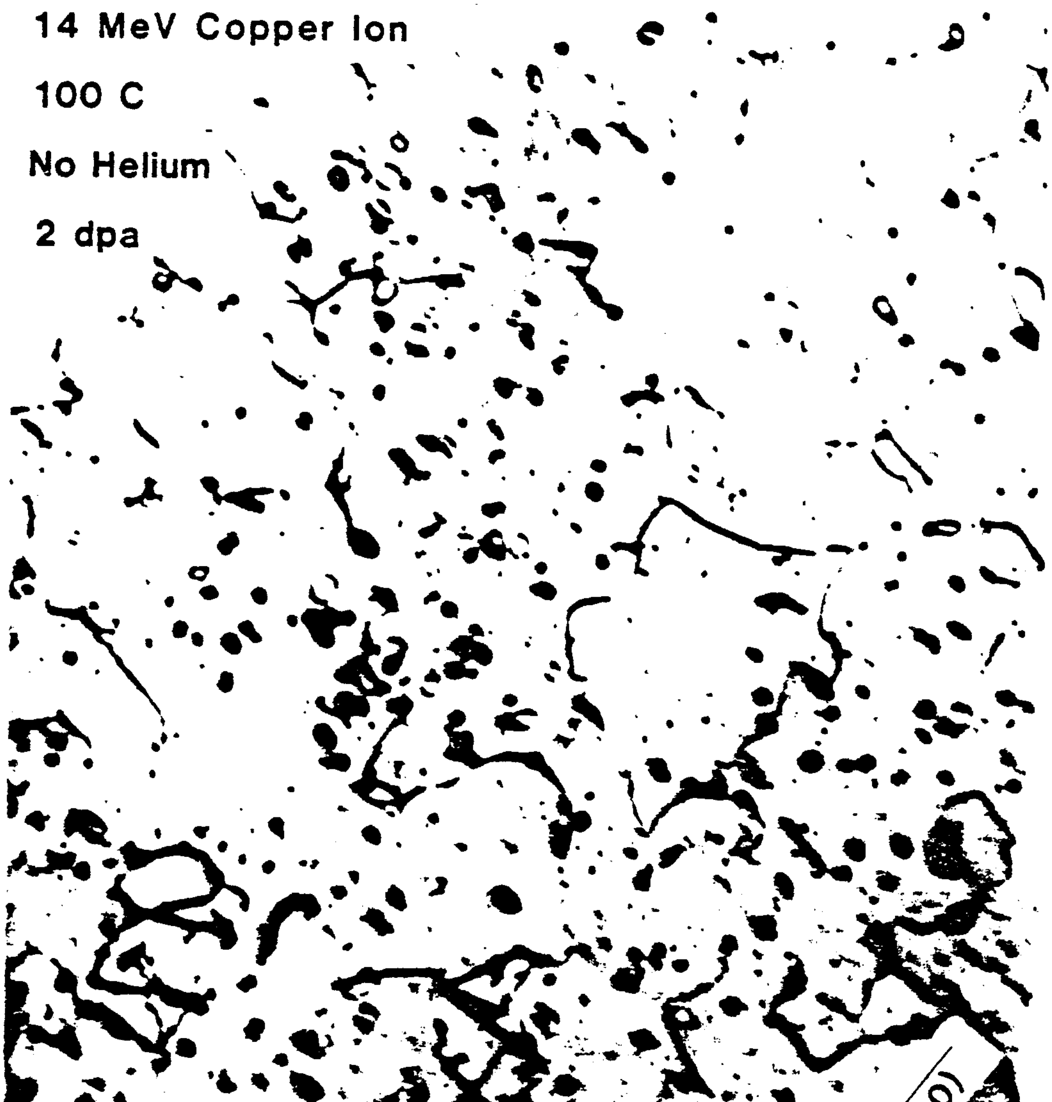

Figure 5.3 A micrograph of copper ion irradiated aluminum at 100 C illustrates the increase in the dislocation density. The loops analyzed in this sample were essentially all vacancy type.

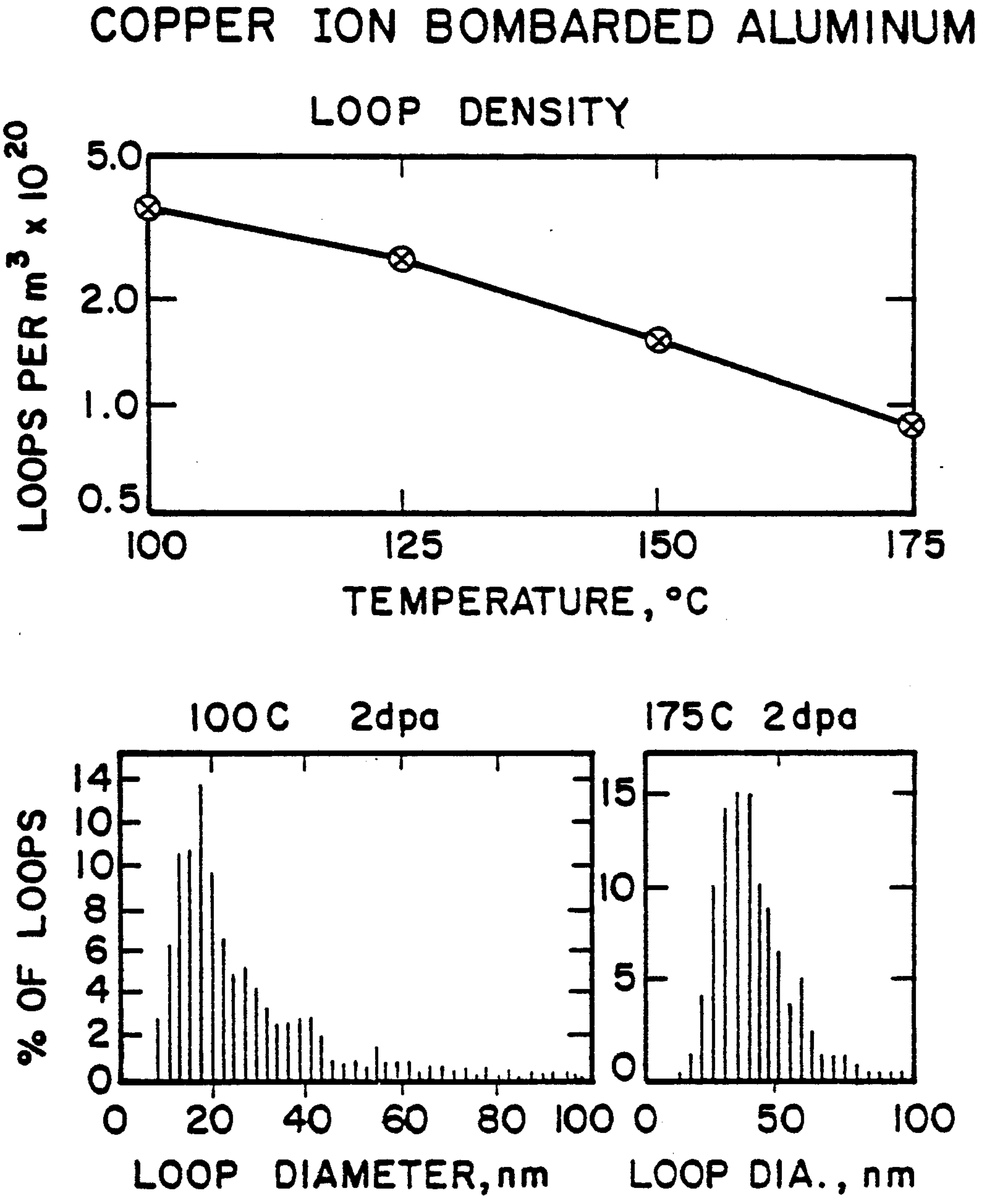

Fig. 5.4. Two representative histograms of the number of loops as a function of loop diameter for two temperatures.

Figure 5.5 The end of range of the copper ions in aluminum shows structures resembling theta prime precipitates in aluminum-copper. An inset diffraction pattern shows no streaking and a 100 orientation for the precipitation.

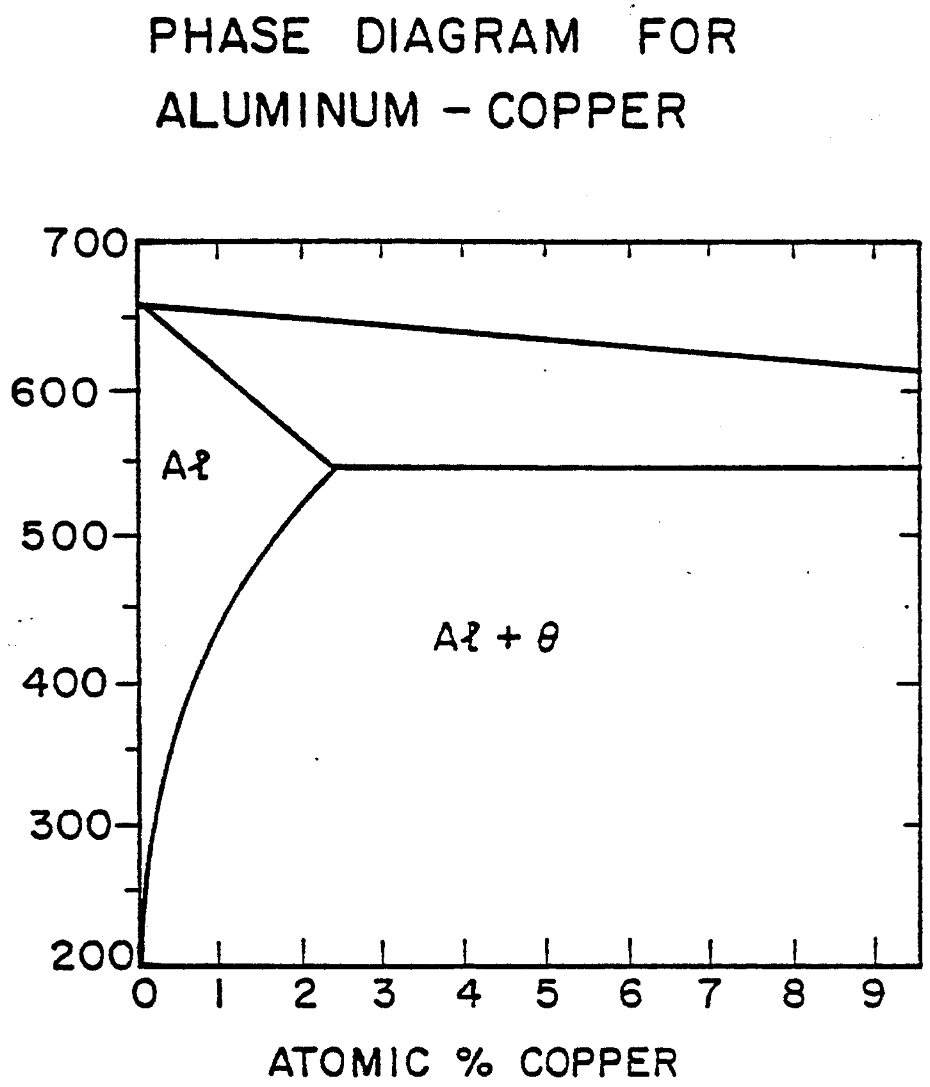

Figure 5.6 Aluminum-Copper phase diagram shows the two phase theta region where the injected copper will precipitate out of the aluminum matrix into a Al -Cu platelette precipitate aligned in <100> crystal plane.

cipitate that is aligned in <100> crystal plane. This θ phase is observed in aluminum-copper alloys where the concentration of copper is nominally 1% to 4% by weight. (A 4 wt.% copper alloy is 1.7 at.%.) The θ precipitate is a two-dimensional structure since the plate thickness is very small being only a few atom layers thick.

Efforts to identify the chemical composition of the microstructural defects that appear as platelet type precipitates was not successful and the interference of θ precipitation was made by comparison with a known aluminum-copper alloy. An analysis of the irradiated zone of the bombarded aluminum samples in scanning transmission electron microscopy (STEM) and observing the emitted x-rays from the fluorescence of the sample from the incident electron beam could not detect a significant amount of copper in the defect structures. The transmission electron microscope column and sample stage contain copper and a small number of x-rays from the column and sample stage are always present. The concentration of copper detected was the same as the background source of copper arising from x-rays coming from copper associated with the structure of the microscope column and microscope stage. The background was reduced by using a beryllium sample holder but the level of copper detected could not be attributed to the irradiated zone.

The interaction of a thin plate with the transmission electron beam produces a modification of the diffraction effects observed. θ precipitates or flat two-dimensional structures cause streaking of the diffraction pattern in the diffraction net perpendicular to the directions of the precipitate plane.(5.3) A micrograph shown in Fig. 5.5 of aluminum irradiated with copper ions contains two-dimensional microstructural defects that resemble θ precipitates. The corresponding diffraction pattern show no evidence of diffraction spot streaking indicating the structures do not have a well ordered structure. The effect of streaking also influnces the dark field appearance of the precipitates by enhancing the dark field intensity. The precipitates appear much brighter in dark field when the appropriate diffraction vector is selected and the images are free of other strongly diffracting sources present in bright field. The dark field observations of the copper ion irradiated aluminum could not identify the precipitates by dark field enhancement.

An alloy of aluminum and 3 wt.% of copper as seen in Fig. 5.7(5.4) shows an example of θ precipitates. This alloy was aged at 175°C for 2 weeks to grow the θ precipitates. The similarity between this known aluminum copper alloy was used to establish the identity of the precipitates in the copper ion bombarded aluminum.

The appearance of the microstructures only in the copper ion irradiated aluminum suggest by their shape and size to be θ precipitates that occur in aluminum copper alloys. Three approaches of characteristic x-ray emmission, diffraction net streaking, and dark field enhancement used to identify the precipitates as copper enriched zones were unsuccessful. Identification of the precipitates as copper θ' was not possible but their absence in aluminum ion irradiated aluminum suggests that copper is involved in the formation

THETA PRECIPITATES IN AL-CU ALLOY

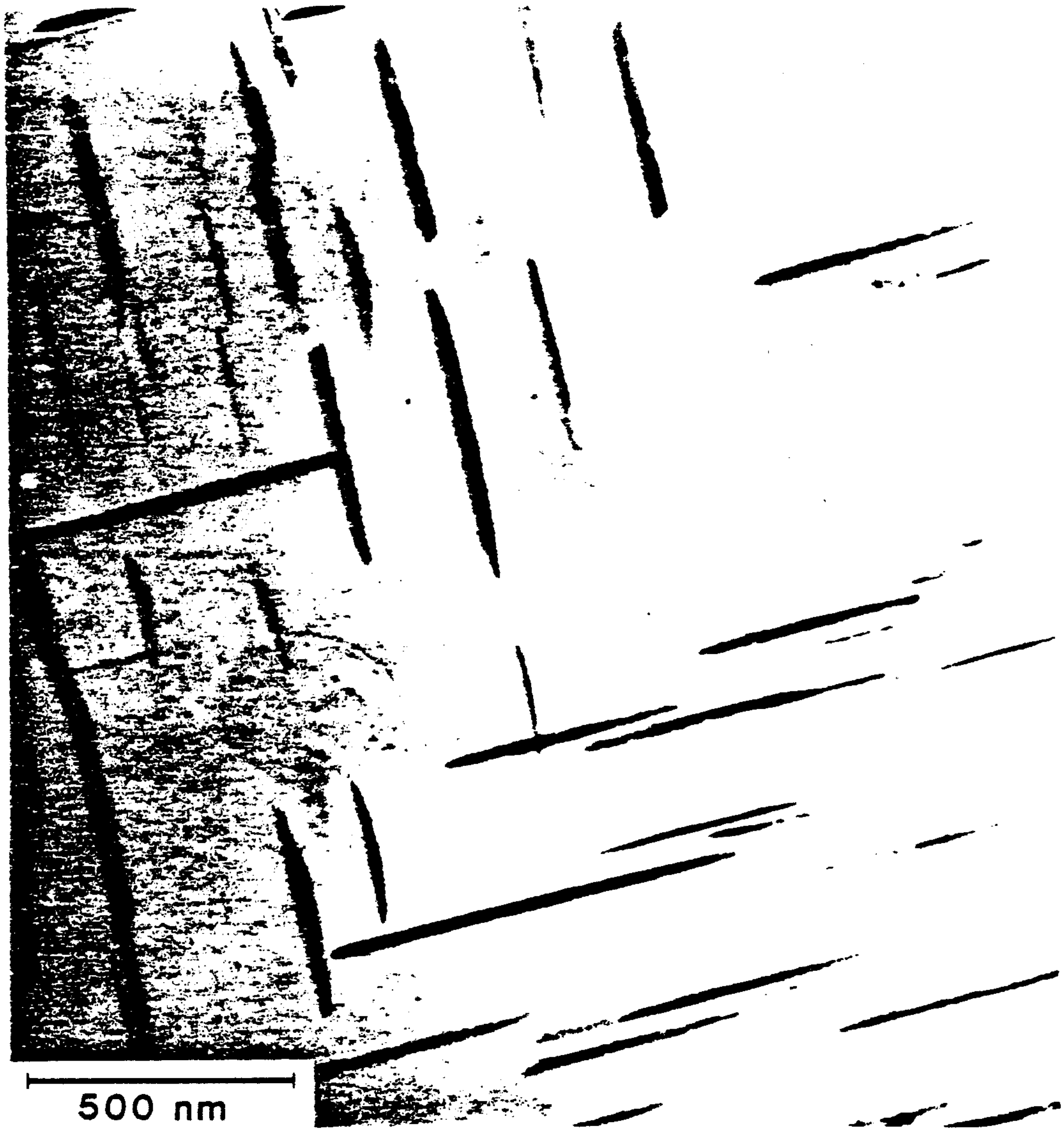

Figure 5.7 An alloy of aluminum and 3 weight percent of copper shows theta precipitation. This alloy was aged at 175 degrees C for 2 weeks to grow the theta precipitates. (Ref 5.4)

of the precipitates and the precipitate resemblance to θ precipitates indicates that they are θ precipitates.

The major difference between aluminum ion irradiated aluminum and copper ion irradiated aluminum is that the irradiation enhances the formation of these θ precipitates from copper ion deposition at a very low concentration of copper. The copper ions come to rest in the aluminum at 5 μm in a normal distribution with a FWHM of 0.75 μm and the foils were examined at 3 μm which is separated by 2 μm from the peak of the deposited ion region. The appearance of elongated microstructures in the irradiated zone removed from the deposited copper ions suggests that the copper ions are mobile and a very small number of copper atoms are needed to enhance the formation of microstructural defects. The high purity aluminum contains less that 1 at.ppm metallic impurities as shown in Table 4.1 and the injected copper ion contribution to this amount is 950 at.ppm.

Irradiations of aluminum with aluminum ions did not show the two-dimensional pseudo θ precipitates but they did contain significant concentrations of heterogeneous microstructural defect clusters and arrangements. A discussion of the aluminum ion irradiations appears in section B (Aluminum Ion Irradiation). A micrograph of aluminum ion bombarded aluminum (Fig. 5.8) and copper ion bombarded aluminum (Fig. 5.3) demonstrate the effect of copper ions. The difference is actually greater than shown since the aluminum ion irradiation was done at twice the damage level of 4 dpa than the 2 dpa

HETEROGENEOUS DISLOCATION DISTRIBUTIONS IN ALUMINUM ION BOMBARDED ALUMINUM

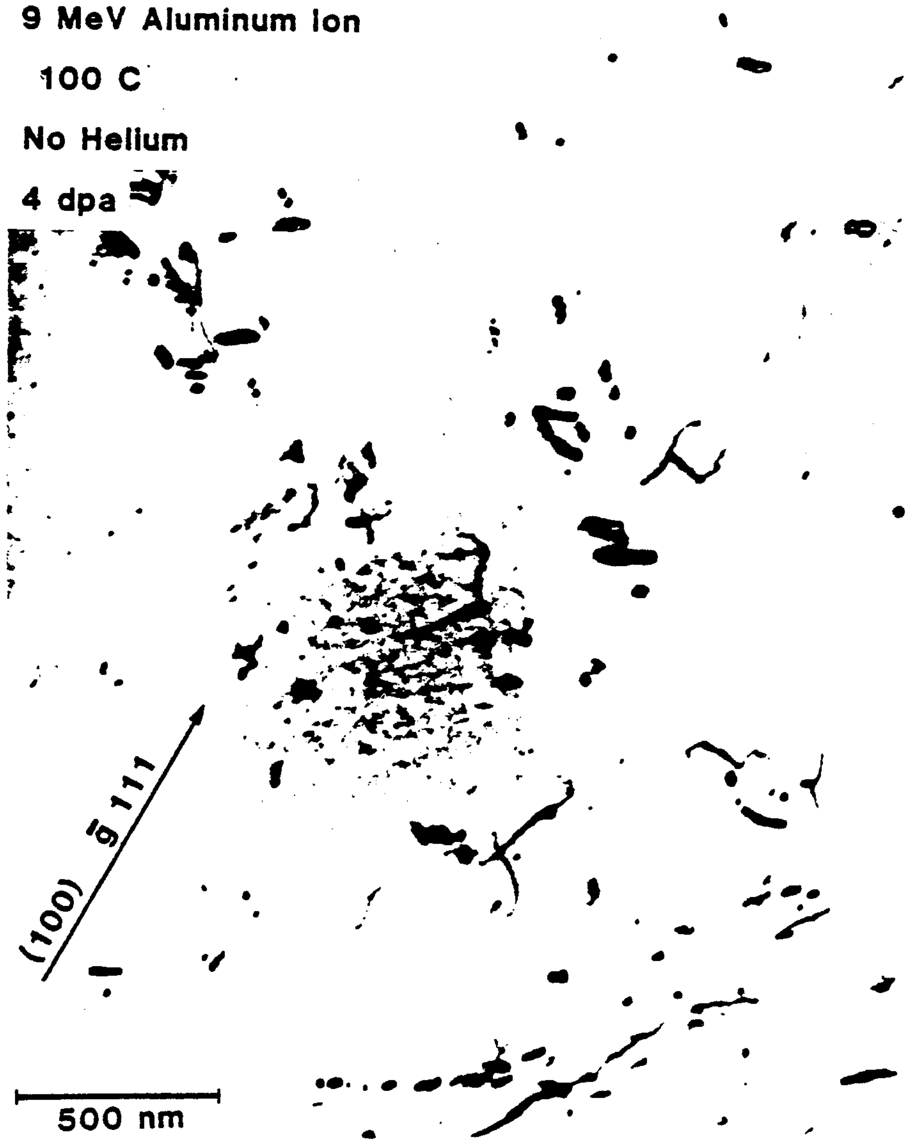

Figure 5.8 Loops in aluminum ion bombarded aluminum were distributed heterogeneously as lines of loops, clusters of loops and loop prisms.

damage level for the copper ion irradiation. The presence of copper is the primary reason for the difference.

Copper ion irradiation of aluminum presents the metal with a new environment that is energy intensive. The addition of energy to the material does not appear entirely as heat but as other energy sources that have high temperature and high pressure analogies. One source of this energy appears as an enhanced vancancy concentration in addition to and well in excess of the existing thermal vacancy concentraton. The vacancies are known to enhance diffusion and hence they can affect the formation of defect microstructures by solute drag mechansims. The ion beam production of vacancies and interstitials can alter the equilibrium state of the material as discussed by Potter.(5.5) From these considerations, the microstructural precipitates are believed to be a radiation enhanced θ phase of aluminum and copper where the copper concentration is very small. The identification of these microstructural artifacts as true θ structures could not be accomplished with present analyzing equipment.

It is from the comparison between aluminum ion irradiations and copper ion irradiations and with a known aluminum copper alloy that the defect structures that appear from the copper ion irradiation are identified as θ precipitates. The concentration of θ precipitates increases toward the deposited copper ion region and resemble the θ precipitates in aluminum copper in appearance. The concentration of copper in the analyzed foil was less than 0.1 at.% and too low to be detected.

B. Aluminum Ion Irradiated Aluminum Without Helium

B.1 Results Overview

The copper ion bombarded aluminum consistently exhibited extensive heterogeneous distributions of dislocations and dislocation loops. A new aluminum ion beam was developed and used to bombard the aluminum samples, eliminating the impurity effects of injected copper ions by using injected aluminum ions or "self ions." Samples of aluminum were annealed and outgassed and then bombarded with aluminum ions at temperatures ranging from 150°C to 50°C with most of the irradiations occuring at 100°C. Table 5.2 is a summary of the aluminum samples bombarded with aluminum ions.

B.2 Dislocations, Dislocation Loops and Dipole Loops

In all of the aluminum samples analyzed, the dislocation loops that formed were essentially all vacancy loops with a burgers vector of <110>. There were no faulted loops or frank loops with a burgers vector of <111> observed in the aluminum ion bombarded samples. The dislocations were "shear loops" or a mixed dislocation loop consisting of part edge and part screw dislocation. This type of loop is commonly called a prismatic loop since the burgers vector and the glide plane define a glide cylinder in which the loop moves. Shear loops do not have a fixed loop plane normal and the dislocation loops observed had loop plane normals that were generally in the <111> directions.

The loops were distributed in a heterogeneous manner as shown in Fig. 5.8, but the degree of heterogeneity was less than that of the

TABLE 5.2. ALUMINUM ION BOMBARDED HIGH PURITY ALUMINUM SAMPLES

Sample #	Dose (dpa)	Temp. °C	Comments
3-8-71	4	100	Vacancy loops and no voids
6-1-87	6	100	Disl. and loops, no voids
6-2-88	2	100	Very few disl. and loops, no voids
6-5-91	0.6	100	Dislocation loops, no voids
6-7-93	2	75	Dislocation loops, no voids
9-2-102	20	100	Dislocations and loops, no voids
10-3-108	20	50	Dislocations and loops, no voids

copper ion irradiations. The reduction in heterogeneity was to shorten long lines of dislocation loops to occasional short lines of loops, however, the density of the loops was reduced from the copper ion irradiations and in some samples, very little damage could be seen. The loops often occured in clusters or groups and within the group there was often a dislocation associated with the group. The association of a dislocation with a grouping of loops has been made in other irradiations of aluminum by Risbet and Murgoa.(5.6) A line dislocation in the presence of interstitials would climb by absorption of point defects on the edge components of line dislocations. As the dislocation climbs, segments of the dislocation could become pinned by trace impurities and pinch off a hole in the interstitial plane of the climbing dislocation. This would produce a vacancy type loop from the hole in the interstitial half-plane of the climbing edge dislocation. This climbing mechanism is illustrated schematically in Fig. 5.9 and may be seen in Fig. 5.10. The dislocation and the loops around it have the same burgers vector and loops can be observed pinching off from a single dislocation in Fig. 5.10.

A related mechanism that has been postulated for the vacancy loop formation involves a climbing dislocation that leaves an interstitial sheet behind containing a relatively high concentration of impurities. This contaminated sheet would provide a number of pinning sites that could retard the dislocation loop from moving. In the aluminum irradiated by Risbet and Murgoa,(5.6) the observed effect of loop association with a line dislocation was higher in ma-

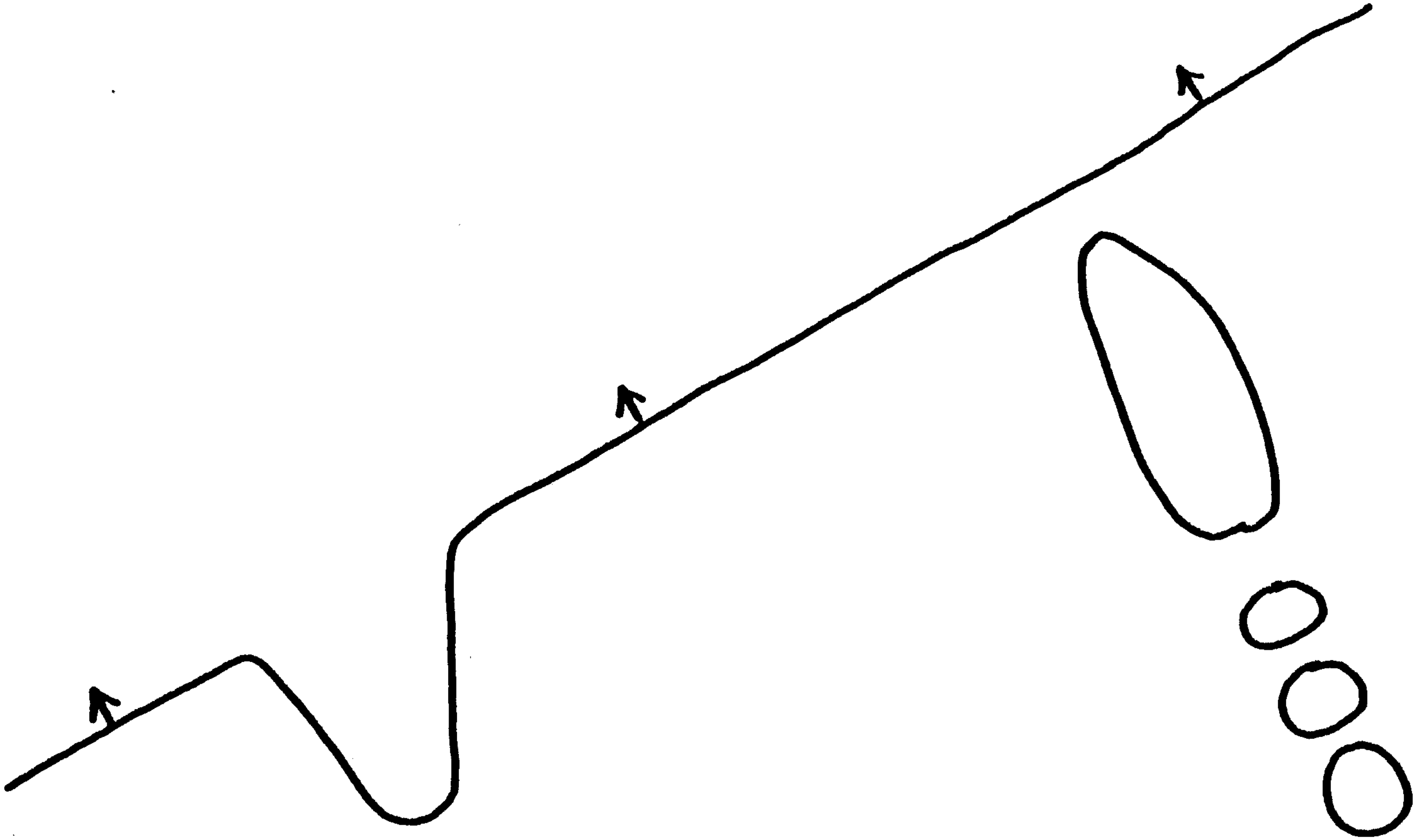

Figure 5.9 A loop producing mechanism resulting from climbing dislocations. A line dislocation absorbs interstitials and climbs. Segments of the climbing dislocation pinch off as a hole or vacancy loop in the intersitial plane of the climbing dislocation.

CLIMBING DISLOCATION IN ALUMINUM

ION BOMBARDED ALUMINUM

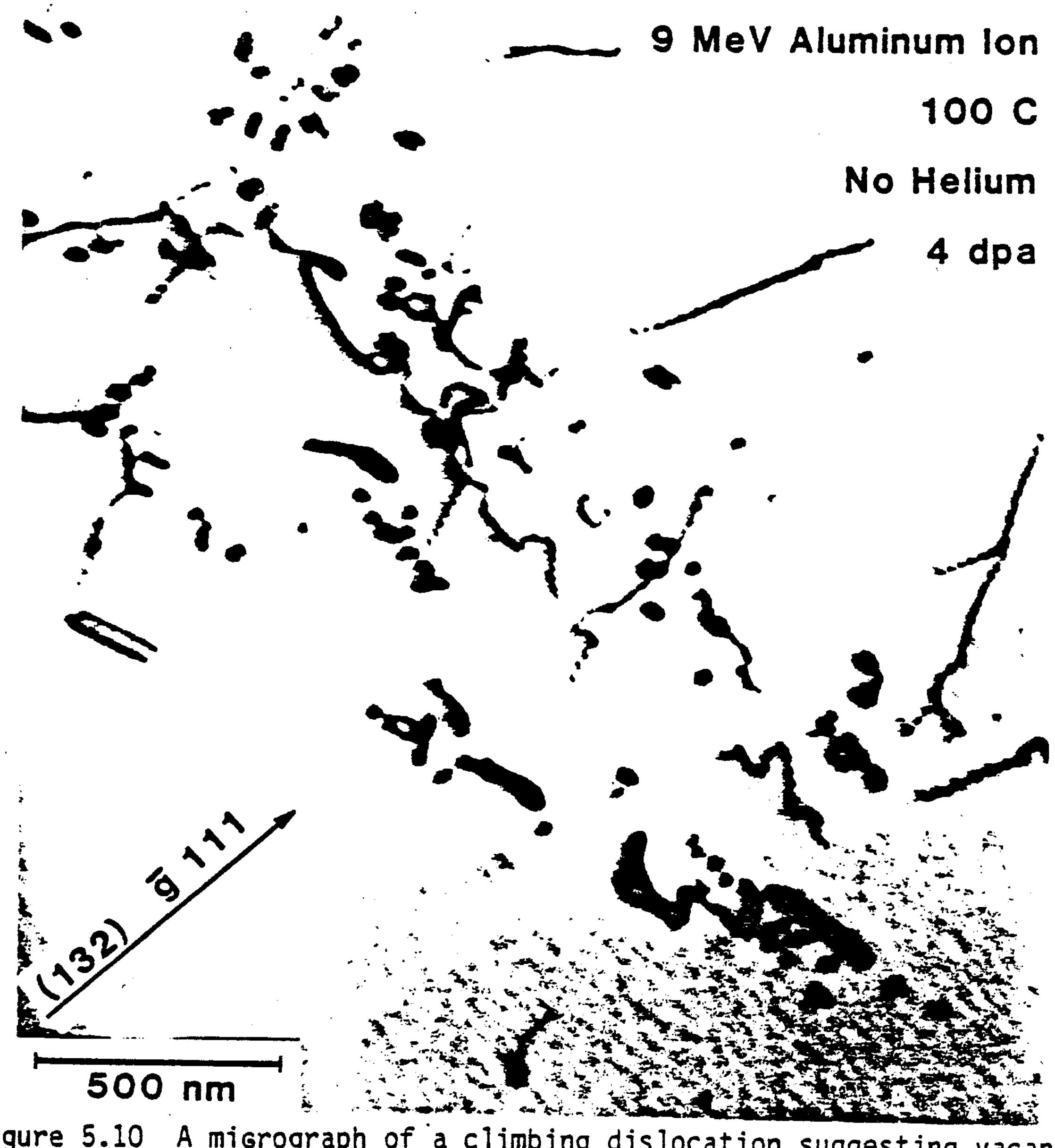

Figure 5.10 A micrograph of a climbing dislocation suggesting vacancy loop formation from the pinning of holes in the interstitial sheet. The line dislocation and the loops all have the same burgers vector and the loops are vacancy in nature.

terials with greater amounts of impurities. The impurity sheet left behind by the climbing dislocation could capture gliding dislocation loops and those loops formed by pinching off from the climbing dislocation.

While neither of the two proposed mechanisisms can be proven from the micrographs from the aluminum ion irradiations, the aluminum material was also irradiated in an EM-7 high voltage microscope at 1 MV to produce damage and observe the irradiation effects on dislocations and dislocation loops. The electron irradiation produced small dislocation loops of Burgers vector <111> that were always faulted. The loops would grow and often a shearing of the <111> loop to a <110> loop would occur, and the glissle loop would immediately glide to the foil surface. A few of the <110> loops remained in the foil after shearing from the <111> type to the <110>. In the case of a line dislocation, the dislocation would show evidence of climb but not in the form described above to produce pinching-off of dislocation loops. The line dislocation terminated on both sides of the TEM foil and during the electron bombardment, the dislocation curved smoothly and evenly as it climbed, with the midpoint of the dislocation line climbing the greater distance and the dislocation end points pinned by the TEM foil surfaces. Copper ion irradiations show large numbers of dislocation loops which supports the impurity assumption but electron irradiations do not show such a process occurring. In the case of electron irradiations, the thin foils and high displacement rate may result in higher <111> loop nucleation and growth than climbing dislocations.

There are two possible reasons for the observed behavior differing from the aluminum ion irradiations. First, the ion irradiations are performed in a thick foil where surface effects are reduced when compared to the electron irradiation. Secondly, the electron irradiation produces Frenkel pairs rather than cascades and a cascade localized near a climbing edge dislocation could produce local concentration gradients of vacancies and interstitials to provide the pinching off of dislocation loops from a climbing dislocation.

There is another mechanism that is less dramatic or interesting but is indirectly observed. The preparation of a TEM foil often concentrates residual stresses which can cause local bending or tearing of the thin foil as described in Chapter 4. The very unstable nature of Frank loops observed in the electron irradiations could account for the absence of Frank loops in the high purity aluminum. The Frank loops were observed in the copper ion irradiations and the copper ions diffusing into the observation zone could stabilize the Frank loops and resist their shearing to <110> loops in the foil preparation process. Not only are there forces from the concentration of stress, but the formation of two surfaces also has an effect as shown by Ham(5.7) in which less than one third of the dislocations remained in aluminum after preparing a thin foil.

Some of the TEM foils were produced with little bending or tearing and these foils were very flat and contained larger concentrations of dislocation loops, but the heterogeneous distribution of the loops still existed in the foil. The foils that were not flat and had been bent by the concentration of compressive stresses contained much lower concentrations of dislocation loops. The loops were also very heterogeneous and as shown in Fig. 5.11 associated with line dislocations. The mechanisim believed to be operating in making these loops heterogeneous is one of dislocation attraction to line dislocations and mutual interactions between dislocation loops. The purity of the aluminum provided few pinning sites for stabilizing dislocation loops and the effect of surfaces and concentration of residual stresses during foil preparation produces loop movement. Those energy configurations of dislocation tangles and mutual loop interaction that produce stable configurations of loops would more frequently remain than individual loops.

Deformation of samples during foil preparation from residual stresses was also indicated by the formation of loop dipoles as observed in Fig. 5.12 for pure aluminum with and without helium. A shear loop can cross slip and form a dipole and the aligned nature of the dipoles in Figs. 5.12(a) and (b) suggests a common source of formation from cross slip as would be caused by mechanical deformation. A dislocation dipole of vacancy type would be formed from the cross slip of a vacancy loop while the formation of a vacancy loop dipole from precipitation of vacancies could be more unfavorable due to pre-

HETEROGENEOUS LOOPS IN A DEFORMED FOIL

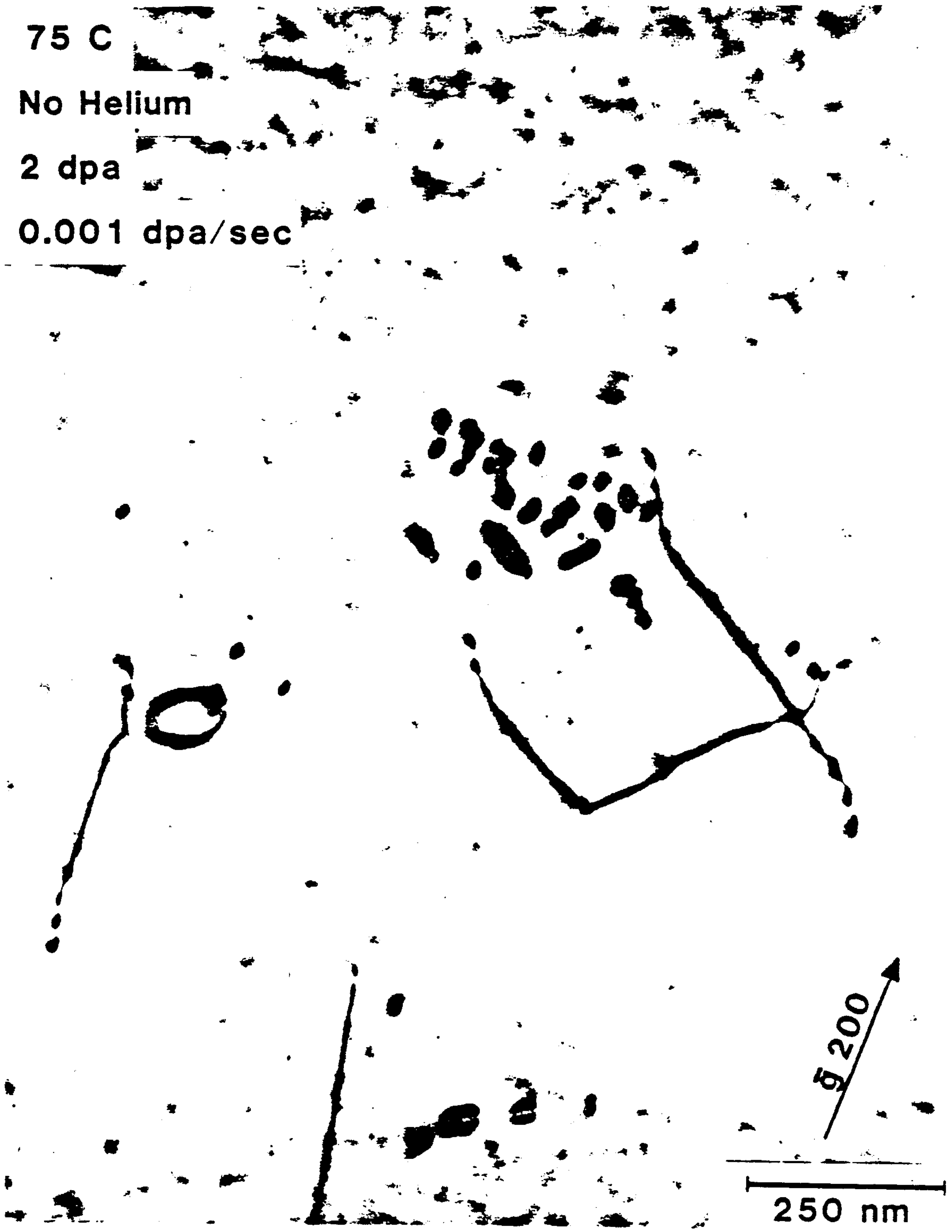

Figure 5.11 Hetergeneous loop clumping with line dislocations is shown and believed to be influenced by foil deformation. The line dislocations provide resistance to loop movement by force field interaction and impurity atom concentrations.

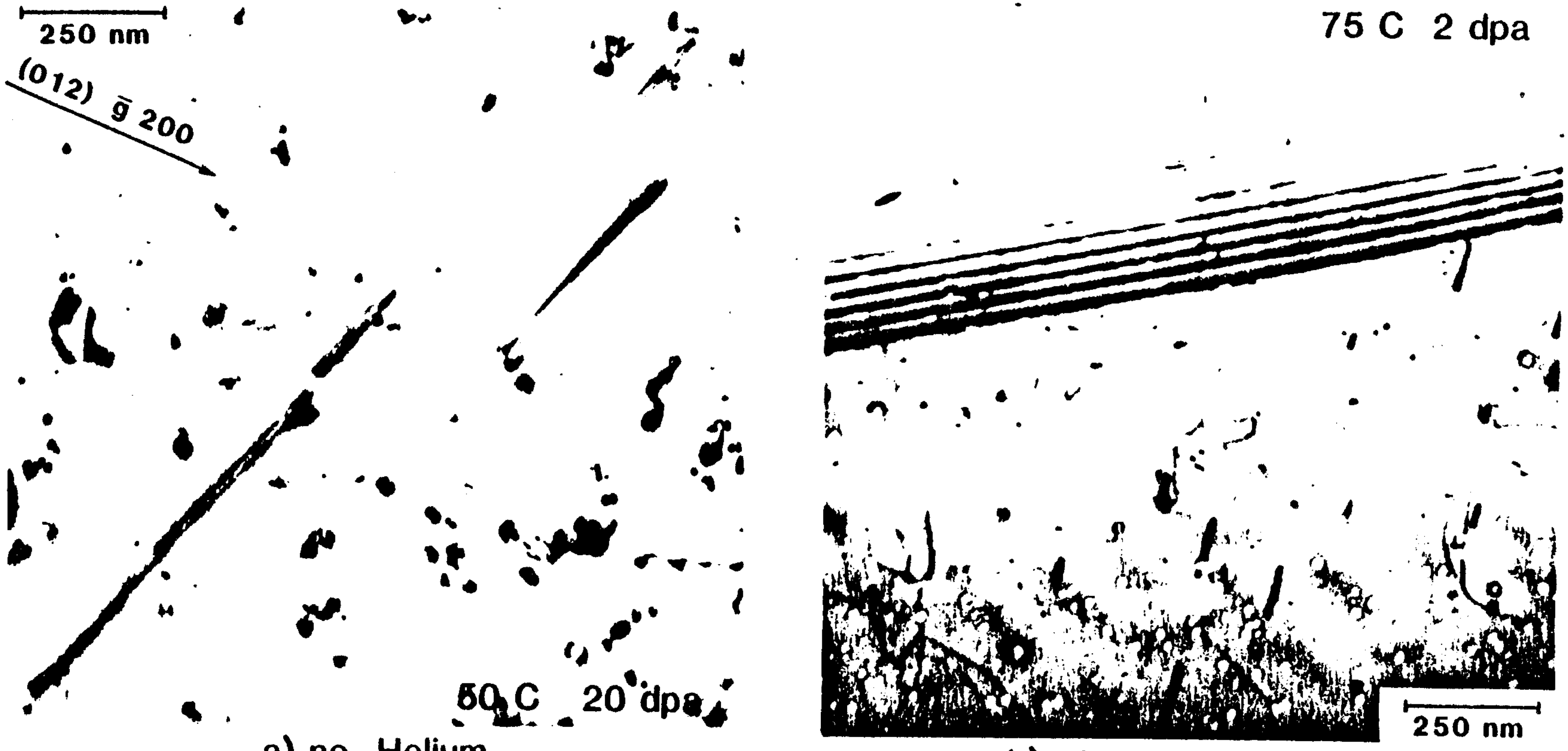

DIPOLE LOOPS IN SELF ION BOMBARDED ALUMINUM

a) no Helium

b) 1 at.ppm Helium

Figure 5.12 Dipole loops were formed in aluminum samples from mechanical deformation during foil preparation from residual stresses in self ion bombarded aluminium with and without helium. The aligned dipole loops suggest a common source of formation from cross slip as would be caused by mechanical deformation. A grain boundary is shown in b) from the extinction contours.

ferred interstitial absorption and higher geometrical energy requirements for dipole loops. The formation of a vacancy dipole offers a source for the observed short strings of loops where the dipole could pinch off and form a series of smaller dislocation loops either from irradiation produced point defects or from thermal vacancy concentrations at or near room temperature in aluminum. A dipole loop can reduce its energy by producing a number of smaller circular loops and create the sequence of heterogeneous loops frequently observed in the ion irradiated aluminum as in Fig. 5.8. It must be stressed that none of these mechanisms could be observed in electron irradiation of aluminum and there are other possible ways the loops could form into the heterogeneous distributions observed.

Electron irradiations of high purity aluminum did not clarify the loop formation process but demonstrated that the two microstructures were quite different in appearance and probably different in formation. The electron irradiations did show that the shear <110> loops are very mobile and the climb of line dislocations in electron irradiations is much slower than the growth of dislocations loops.

Dislocation loops observed in ion irradiated aluminum were always shear loops and the line dislocations also were predominately screw in character. The climb of a shear or screw dislocation line will produce a dislocation helix and these formations were not observed in both electron irradiations and ion irradiations. The helixes are observed in quenched aluminum(5.8) and neutron irradiated aluminum(5.9) at temperatures where only interstitials are mobile. In the case of the quenched aluminum, the dislocations absorb vacancies and climb in a curving manner, wrapping around themselves. No discussion of the manner behind the formation of dislocation helixes in low temperature neutron irradiation has been found but the effect could be the same for a low temperature irradiation where only the interstitials are mobile. In this case, the absorption of the interstitials would produce a helix with the opposite pitch. In ion and electron irradiations of aluminum, no dislocation helixes like those observed in quenched materials or neutron irradiated materials were observed, suggesting that a mix of interstitials and vacancies are arriving at the dislocation.

A phenomen of oscillating loops was observed in aluminum ion bombarded samples. A small loop of type <110> would oscillate or vibrate erratically at a frequency or rate higher than perceptible by the human eye. The vibration was very erratic and the amplitude or distance of movement could be 1 to 20 times the loop diameter. Two sets of micrographs shown in Figs. 5.13 and 5.14 show two different loops showing movement. A time exposure shown in Fig. 5.13 was able to capture the loop in motion and shows the loop as fuzzy or smeared in appearance. A sequence of two micrographs shown in Fig. 5.14 also shows a loop that has moved from position A to position B. The time needed to make this movement is imperceptible or too short to be measured and furthermore, the loop movement was erratic could not be predicted.

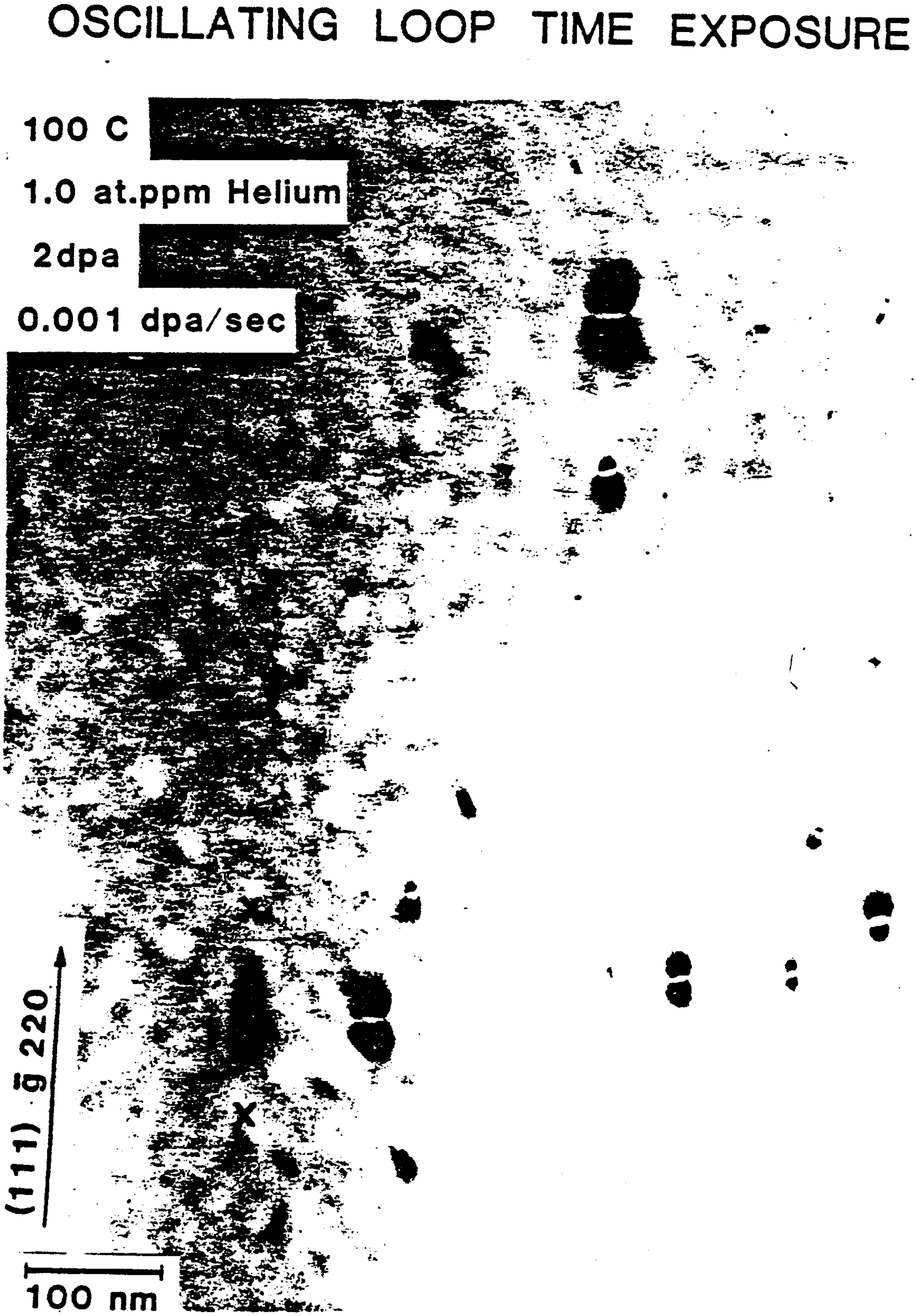

Figure 5.13 A rapidly vibrating loop is shown as a blurred image between the 'x' marks in this micrograph. The exposure time was 15 seconds.

OSCILLATING LOOPS IN ALUMINUM

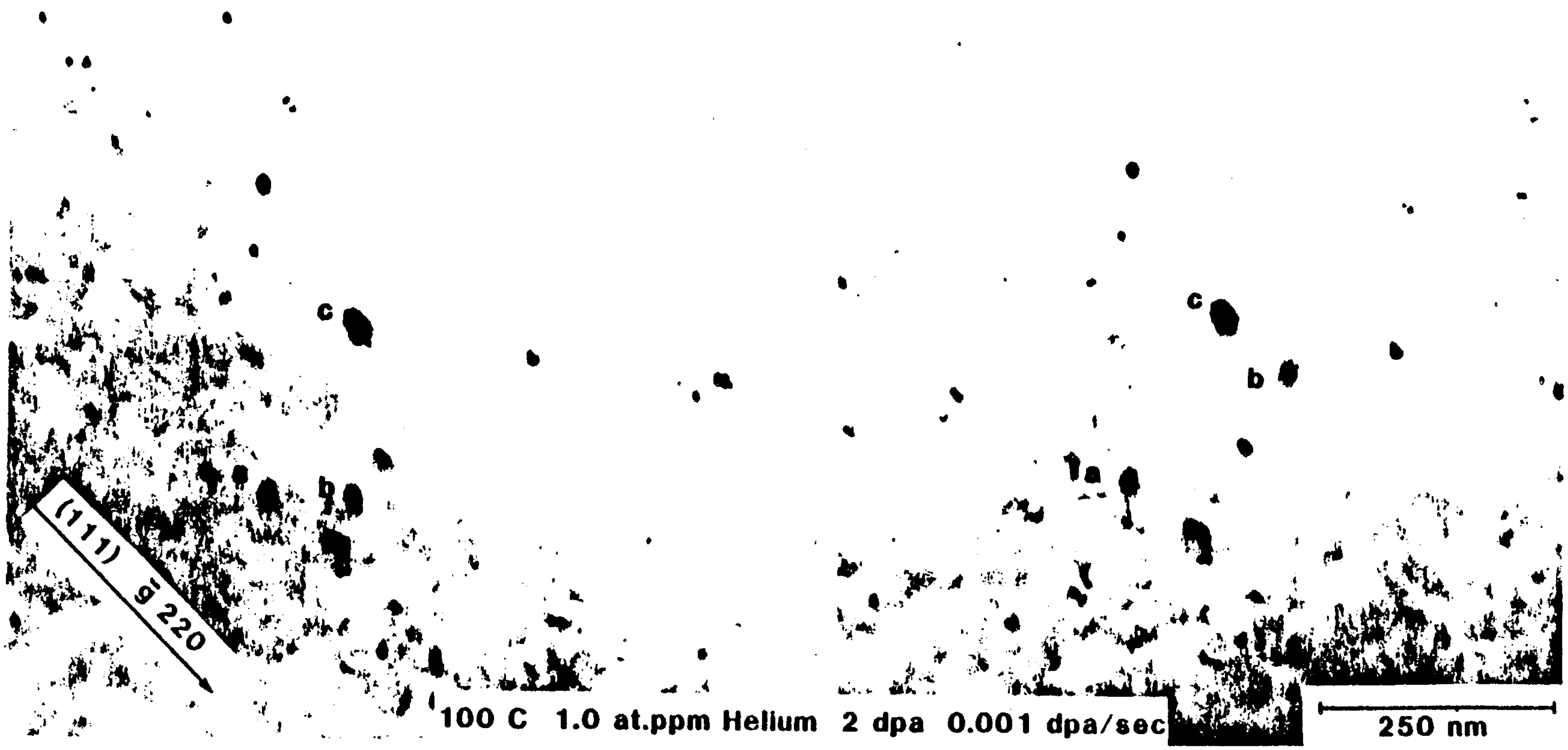

Figure 5.14 A two picture sequence showing dislocation loop movement from position A to B. The loop would move from position A to B and then move back to A.

Motion of glissle dislocation loops requires a stress field and motion between two or more stable points implies a stress field possessing minium points. In addition, the presence or intensity of the electron beam influences the motion of the loop by increasing the intensity of the vibrations when the electron beam is focused or near crossover. Two possible sources for the varying stress field involving the electron beam are temperature gradients from the electron beam heating and a surface contanimation stress.

The electron beam heating would be expected to reach steady state rather quickly and the composition of the electron beam would be reasonably stable. Beam heating temperature gradients that could change so rapidly in the microscope are unlikely while surface contamination from residual pump oils could produce a continously changing stress field.

Residual pump oils are known to produce contamination in the electron microscope as described by Pashley.(5.10) Energy from the electron beam produces cross-linking or polymerization of the hydrocarbon molecules at the periphery of the electron beam. Hydrocarbon chain molecules can be visioned as tumbling along the TEM foil surface until they interact with the electron beam where they are ionized and made chemically active and then reacting with the foil surface or other molecular debris on the TEM foil surface. The effect is to form a contamination halo or ring on both the top and bottom surfaces of the TEM foil and such a contamination halo can be seen in Fig. 5.15 where the beam was exposed for 30 minutes. As the

TEM BEAM CONTAMINATION HALO

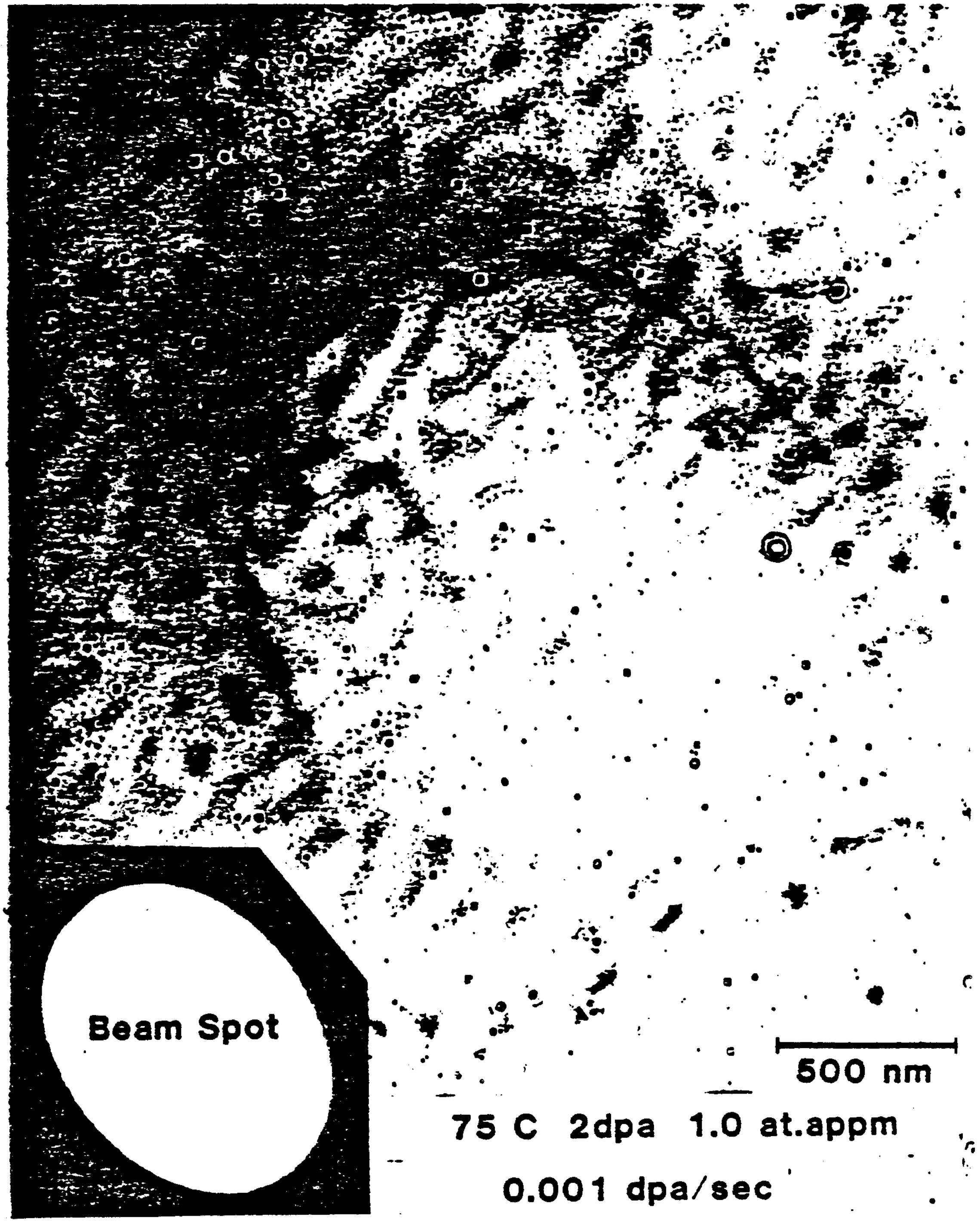

Figure 5.15 A contamination ring in the TEM is indicated by the darker elliptical ring. Hydrocarbon molecules interact with the edge of the electron beam, ionizing molecules, and building a ring of linked hydrocarbons at the periphery of the electron beam. An inset shows the electron beam spot.

halo grows by addition of hydrocarbon molecules, the contamination ring may develop stress arising from cross-linking of the hydrocarbon oils and contract, providing a compressive stress in the inside of the ring and a tensile stress on the outside foil material. A contracting ring would create a series of hills and valleys in the foil contained in the interior of the ring. The stress would build until, at some point along the ring, the stress relaxes with respect to the foil, altering the configuration of the stresses internal to the ring. It is the continual building of the contamination ring and its relaxation or slipping that is believed to be responsible for the oscillating loops. The contamination ring could also be influenced by the foil temperature gradients changing the stress within the ring as a function of temperature.

B.3 No Void Formation

Finally, there were no voids formed in high purity aluminum containing no helium. The aluminum was annealed at 0.8 T_m for one hour at less than 2×10^{-8} torr to outgass the material and produce a large grain size. The aluminum bombarded with aluminum ions to doses of 20 dpa produced dislocation loops and tangles but not any voids as can be seen in Fig. 5.16. The role of gases in metals for nucleating voids would appear to be dominate for the case of ion irradiated aluminum. The effect of homogeneous nucleation or spike nucleation alone is not sufficient to overcome the void nucleation barrier at the dose rates used in this experiment. The effect of helium on void formation is described in the next section.

VOID FORMATION IN ALUMINUM

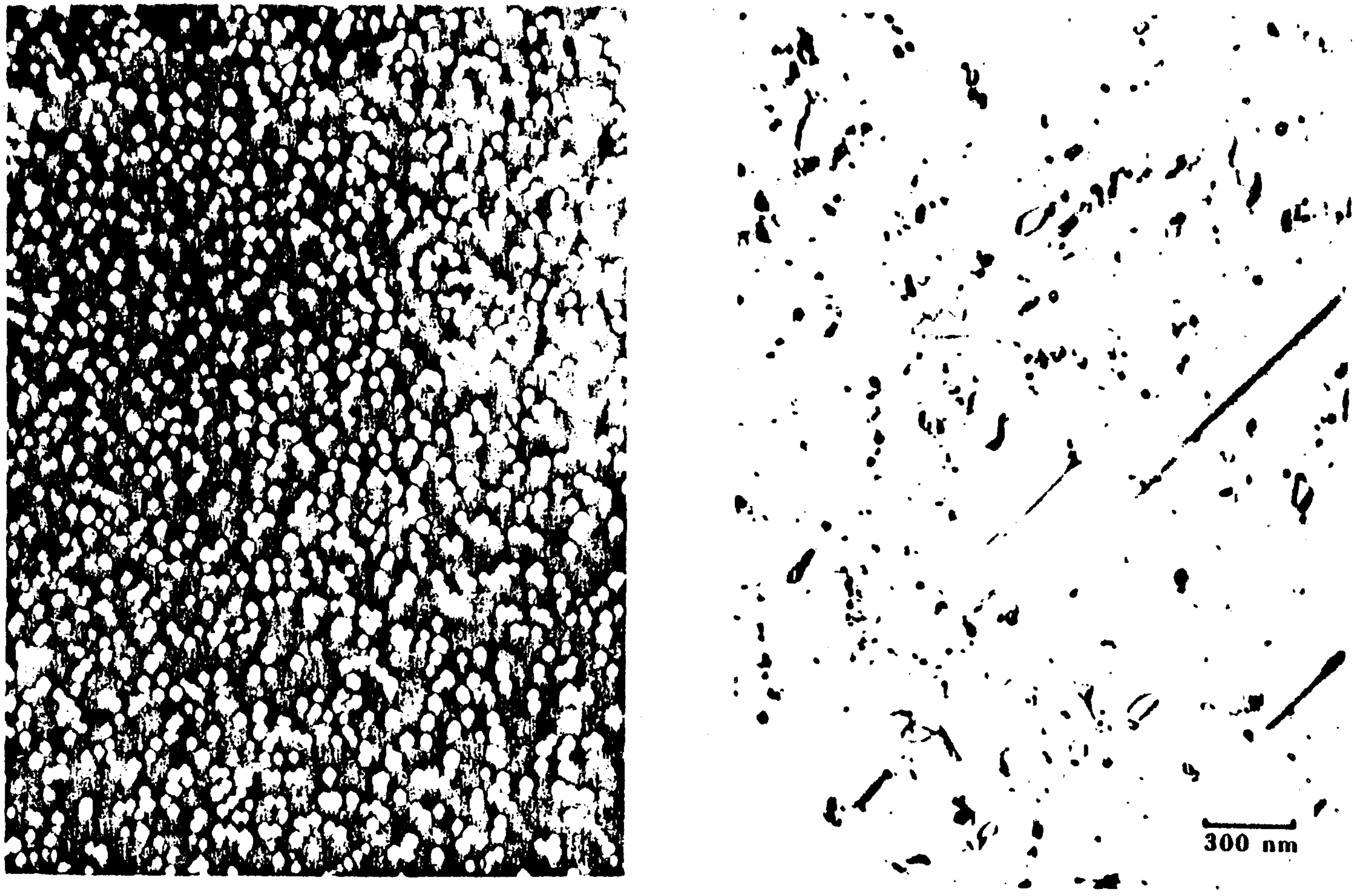

WITH 0.1 at.ppm HELIUM

WITHOUT HELIUM

50 C 20 dpa

Figure 5.16 The effect of helium at 50C and 20dpa. The 20 dpa 0.1 appm helium sample contained 2.5 percent swelling while the helium free sample did not contain any voids.

C. Aluminum Ion Irradiation of Aluminum Containing Helium

C.1 Effect of Helium

Aluminum samples preinjected with helium were irradiated with aluminum ions to doses ranging from 0.2 dpa to more than 20 dpa over a temperature span of 25°C to 150°C. The aluminum samples irradiated are shown in Table 5.3. The major effect of helium was to induce void formation in aluminum as is shown in Fig. 5.16 where two samples of aluminum, one containing 0.1 appm of helium, were bombarded to 20 dpa at 50°C. The helium was preinjected as described in Chapter 4 and this helium is necessary for void formation. All of the aluminum samples bombarded with aluminum ions that formed voids contained helium gas while none of the helium free aluminum samples formed voids.

Experiments were conducted in a matrix consisting of temperature and dose parameters as shown in Fig. 5.17. The purpose of the array was to investigate the effects of temperature and fluence and to obtain an overview of aluminum ion damage as a function of dpa damage, temperature and helium concentration. A dose of 2 dpa was chosen to be the reference dpa value from the observation from computer simulation of point defect saturation in damage at 0.17 dpa(3.24,3.28) and from experimental irradiation time requirements. The value of 2 dpa was also in the middle of the log of the chosen dose scan. The choice of the matrix temperature of 100°C for the dose or fluence scan was from the observation from theory that the peak swelling

TABLE 5.3. ALUMINUM SAMPLES CONTAINING HELIUM BOMBARDED WITH ALUMINUM IONS

Sample #	Dose (dpa)	Temp. °C	He appm	Comments
4-1-72	2	150	5	Aspect ratio voids.
5-4-82	2	125	0.5	Truncated voids.
6-4-90	2	100	0.1	Few scattered voids.
6-6-92	0.6	100	1	Very few voids near g.b.
6-8-94	2	75	10	Voids and dislocations.
7-1-95	26	100	10	Large voids near grain b.
7-2-96	6	100	1	Few voids near grain b.
8-1-98	6	100	10	Homogeneous void distribution.
8-2-99	6	100	0.1	Scattered voids and loops.
8-3-100	20	100	0.1	No loops. Few large voids.
8-4-101	20	100	10	No voids. Sub grain b.
9-3-103	6	25	10	Homo. Voids and loops.
9-4-104	6	25	10	Homo. Voids and loops.
9-7-105	6	50	0.1	Homo. Voids and loops.
10-1-106	2	125	1	Homo. Voids with truncation.
10-2-107	2	50	1	Small homo. voids.
10-4-109	20	50	0.1	Void stringers no void latt.

TEMPERATURE and DOSE MATRIX for ALUMINUM IRRADIATIONS

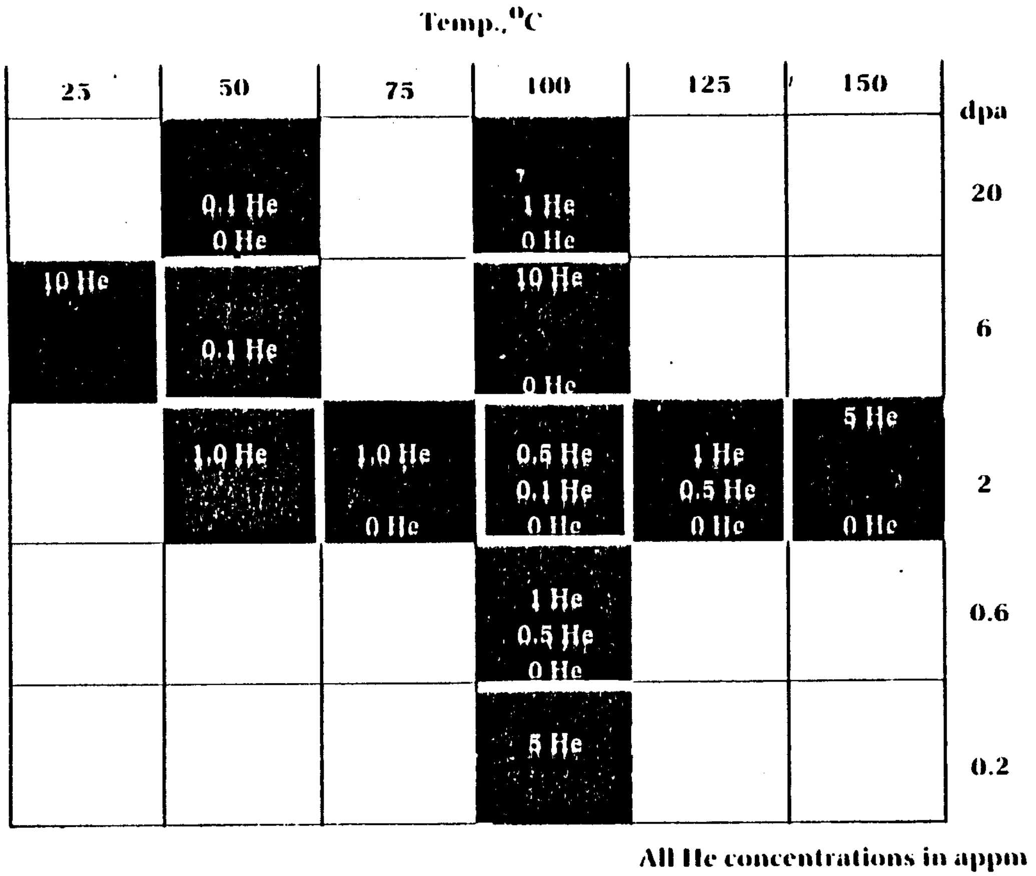

Temp., °C

dpa	25	50	75	100	125	150
20		0.1 He 0 He		1 He 0 He		
6	10 He	0.1 He		10 He 0 He		
2		1.0 He	1.0 He 0 He	0.5 He 0.1 He 0 He	1 He 0.5 He 0 He	5 He 0 He
0.6				1 He 0.5 He 0 He		
0.2				5 He		

All He concentrations in appm

Figure 5.17 The irradiation matrix for radiation damage studies in pure Aluminum. The matrix consists of a dpa dose scan at 100C and a temperature scan at 2 dpa. Additional areas were required to investigate interesting behavior.

would occur at 0.4 T_m and 100°C was near the upper limit of the cold stage temperature controller.

C.2 Effect of Temperature on Void Formation

Voids formed in ion irradiated aluminum containing helium at all the temperatures investigated. The temperature range was from 25°C to 150°C or 0.32 T_m to 0.45 T_m, which covers the general void formation temperature range. While visible voids formed at all temperatures, there were samples where the formation of voids was much more prevalent than in other samples. This was characterized by the scattered positions of the voids or clumping of the voids in some regions while other regions were completely devoided.

The temperature of 0.4 T_m or 100°C was particularly difficult to produce homogeneous concentrations of voids. Unfortunately for the dose or fluence scan, this temperature was used to study the effect of fluence on void formation and a significant number of bombarded samples were expended at this temperature. Theory predicts that 100°C or 0.4 T_m is the peak of the swelling temperature and the experimental data for aluminum indicates that void swelling is difficult to get at 100°C. The problem lies with nucleation since the voids that did form grew in size but there were very few of them, and the void formation was always near grain boundaries or dislocation tangles as shown in Fig. 5.18. The sample shown in Fig. 5.18 was bombarded to 26 dpa and contained 1.0 appm of helium but voids would only form near the grain boundary. Voids never were observed on the grain boundary and a denuded zone of 30 to 50 nm was typical for

DISTRIBUTION OF CAVITIES

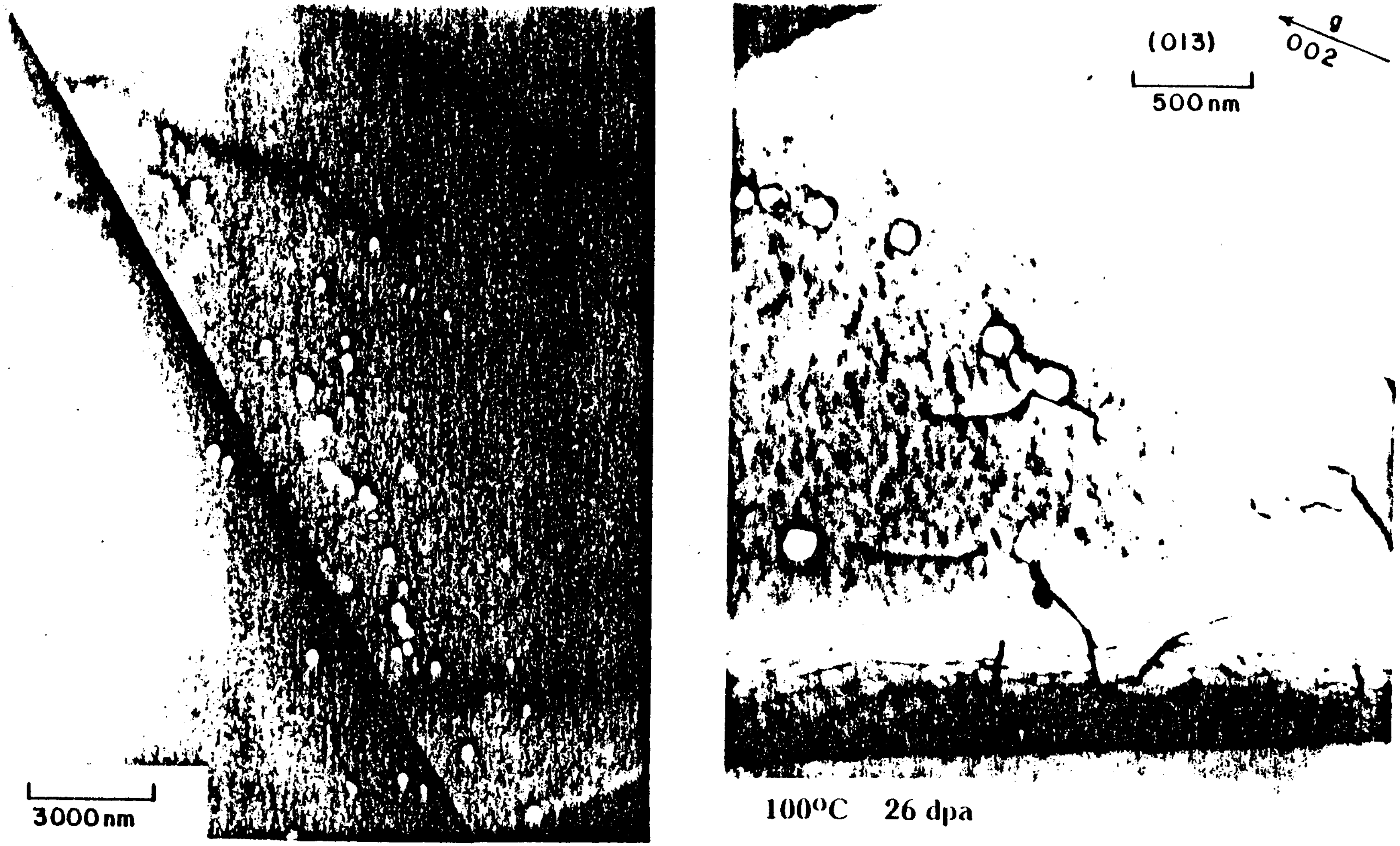

GRAIN BOUNDARY and CAVITIES

DISLOCATIONS and CAVITIES

Figure 5.18 A micrograph showing the heterogeneous nature of the void distribution with respect to the grain boundary in the bombarded material. The voids also show a 30 to 50 nm denuded zone next to the grain boundary when the grain boundary is tilted to edge on.

voids near the grain boundary. The voids are located within 4 μm of the grain boundary which is more than the amount of material removed from the surface, so the effect of the grain boundary as a major sink which operates over the extremely long distance of 4 μm is unlikely because the presence of the surface would have induced void formation just as the grain boundary did.

Another major factor in the void nucleation is the displacement rate and the actual displacement rates have been included with each of the tables for the irradiation summaries. The dpa rate for most of the 100°C irradiations was lower than the typical 1×10^{-3} dpa/sec but there were some bombardments at or near the 1×10^{-3} rate and voids were observed in aluminum at 125 and 150°C at even lower dpa rates. The dpa rate is important and efforts were made to keep the dpa rate between experimental runs constant but the major point is that temperature and dpa rate are similar in their effect on vacancy supersaturation. If the dpa rate was too low at 100°C then a lower dpa rate at a higher temperature would be even less likely to show void formation, however, the irradiations at 125°C show homogeneous void concentrations and the voids formed at 150°C were more homogeneous than those formed at 100°C. So the dpa rate was sufficient at 100°C to form voids but only in the areas where nucleation was enhanced.

The major effect of temperature on void formation was the effect of temperature on void concentration or number density (N_v). The void number density decreased with increasing temperature, following the qualitative predictions of void nucleation theory. The void number densities are shown at a constant dose of 2 dpa at temperatures of 50, 75, and 125°C in Fig. 5.19. The void number density at 50°C was 1.2×10^{21} per m^3 and decreased to 5.1×10^{18} at 125°C. A plot of the log of the number density at 2, 6 and 20 dpa is shown in Fig. 5.20 where the dpa level is indicated by the legend markers. The number density shows a strong dependence on the temperature and a much weaker dependence on dpa level, indicating that nucleation occurs early in the irradiation and turns off. Bombarding the sample to higher dpa levels increases the size of the voids but has little effect on the number density.

Since the void number density is a strong function of temperature and the total swelling is the product of the number density and void size, it was not surprising to see that void diameter was influenced by the bombardment temperature in the reciprocal manner of the number density. As the number density decreased with increasing temperature, the void diameter increased with increasing temperature, which tends to conserve the number of vacancies available for swelling. A plot of the void diameter as a function of temperature is shown in Fig. 5.21 at a dpa dose of 2 dpa. Unlike the number density, the void diameter is also a function of dose and the dependence on temperature depended on the nucleation number density and the total number of vacancies produced.

The voids observed in aluminum are characteristically octahedral in shape, following the minimization of surface energy on the eight

EFFECT OF TEMPERATURE ON VOID FORMATION IN ALUMINUM ION BOMBARDED ALUMINUM

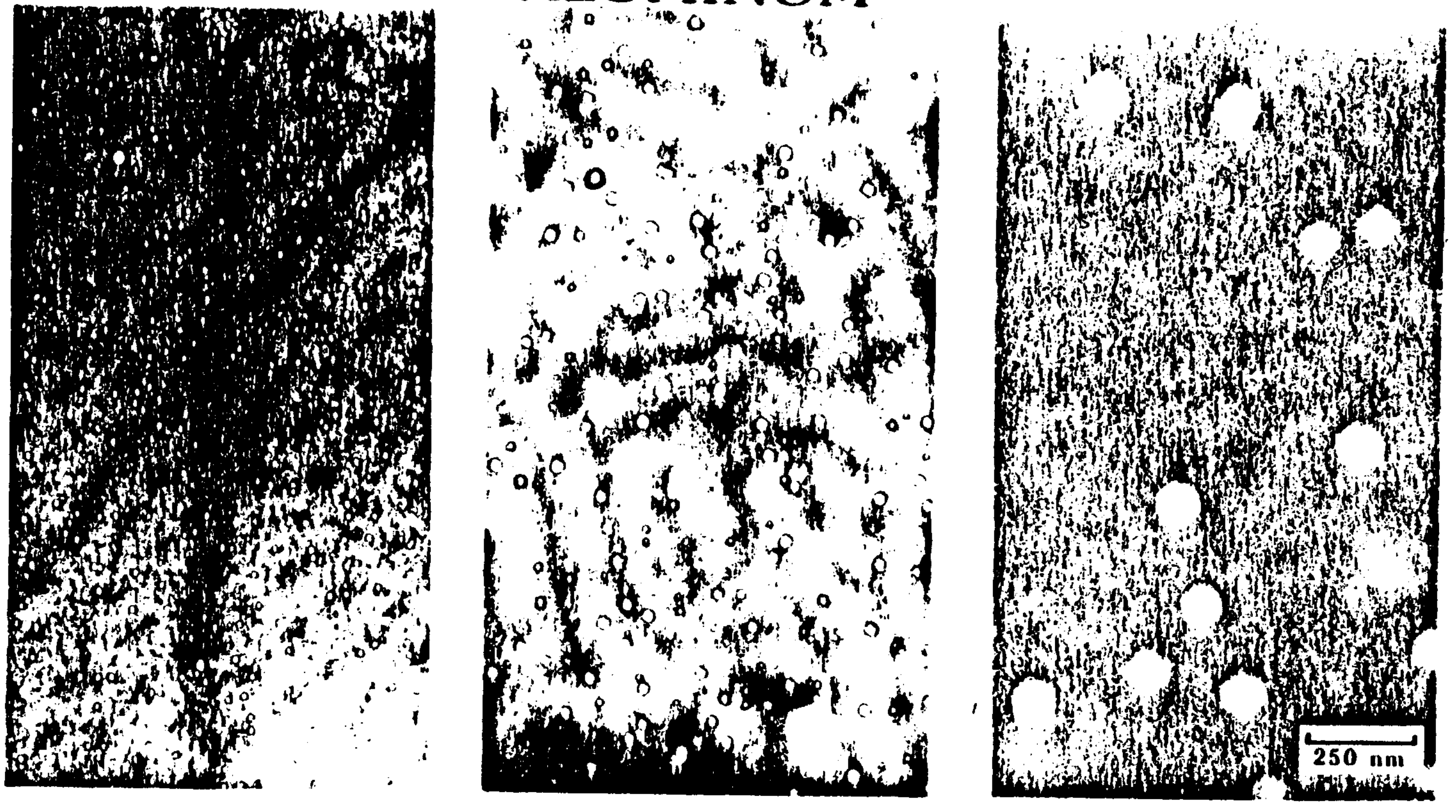

50°C 2 dpa at 75°C 125°C

.001 dpa/s 1.0 at.ppm He

Figure 5.19 A series of three micrographs showing the variation in void size and number density as a function of temperature at a constant dpa dose of 2 dpa. The foil thickness was 200 nm for 50 and 75 C and more than 600 nm for the 125 C foil.

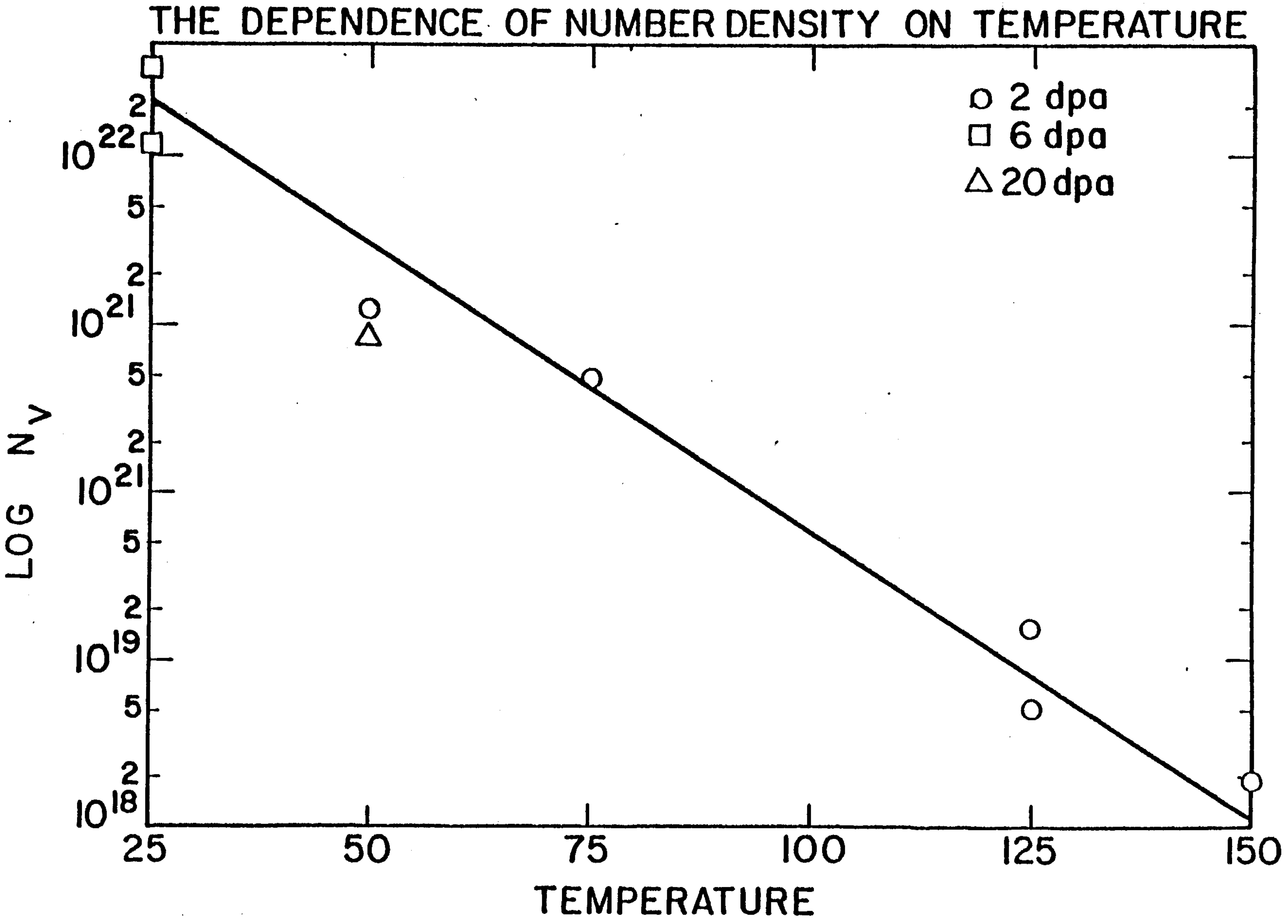

Figure 5.20 The temperature effect on the void number density in aluminum containing helium is shown for 2, 6 and 20 dpa. The number density is insensitive to the dose level but a strong function of the

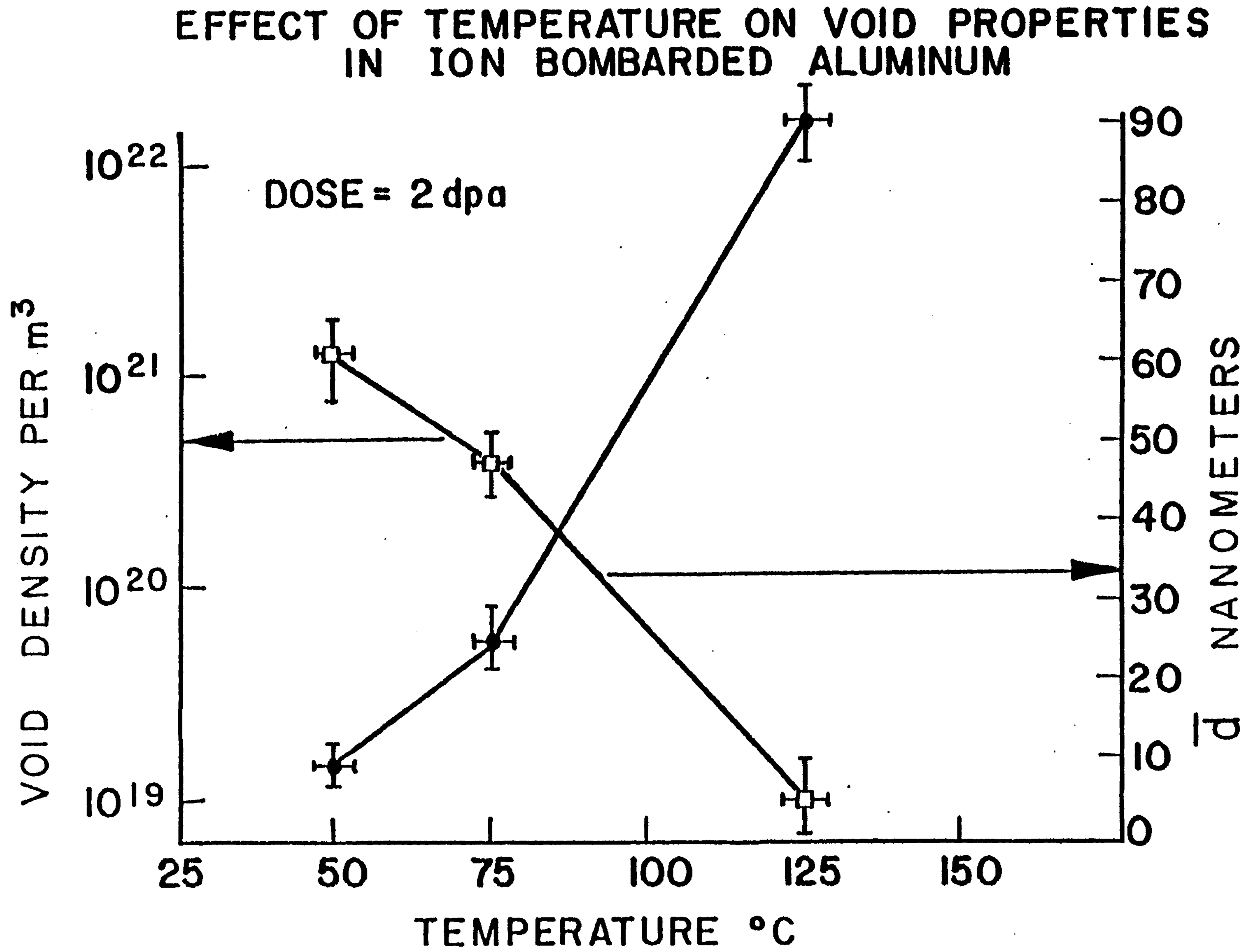

Figure 5.21 The temperature effect of radiation damage is shown by decreasing the void number density Nv and increasing the void diameter ⟨d⟩ as the temperature increases. The nucleation theories and previous results in other materials exhibit this qualitative trend.

(111) planes in the face centered cubic (FCC) metal system. The octahedron has more surface area than a sphere of equivalent volume and voids of octahedral shape would like to reduce their surface energy by becoming spherical. Rounding of the octahedral voids appears as truncation of the void and is temperature sensitive. No truncation was seen in samples irradiated below 75°C and nearly all voids at 125°C were truncated. The rounding of voids is evident in the 125°C temperature micrograph in Fig. 5.19 where the round voids should appear square. A high magnification micrograph, shown in Fig. 5.22, of a single void taken as to enhance the visibility of the internal surface shows the truncation of the octahedral ends as (100) planes and the octahedral edges (110) planes. This same form of truncation was also observed by Risbet(5.11) but the temperature of those neutron irradiations was between 130°C and 220°C.

At 150°C the truncation of the voids increased and supervoids or elongated voids formed. A supervoid is a void which is greatly exaggerated in one axial direction, forming a tube with one-half of an octahedral void face at each end. The octahedral void elongated in [112] and [100] directions in two different observations as seen in Fig. 5.23. The [112] direction is bounded by (111) and (110) planes while the [100] direction is bounded by (110) planes. Both directions are schematically illustrated in Fig. 23 for the (112) and (100) projections. Risbet(2.40) identified elongation directions [112] and [110] in high purity aluminum but not in the [100] directions. The elongation direction in high purity aluminum was not

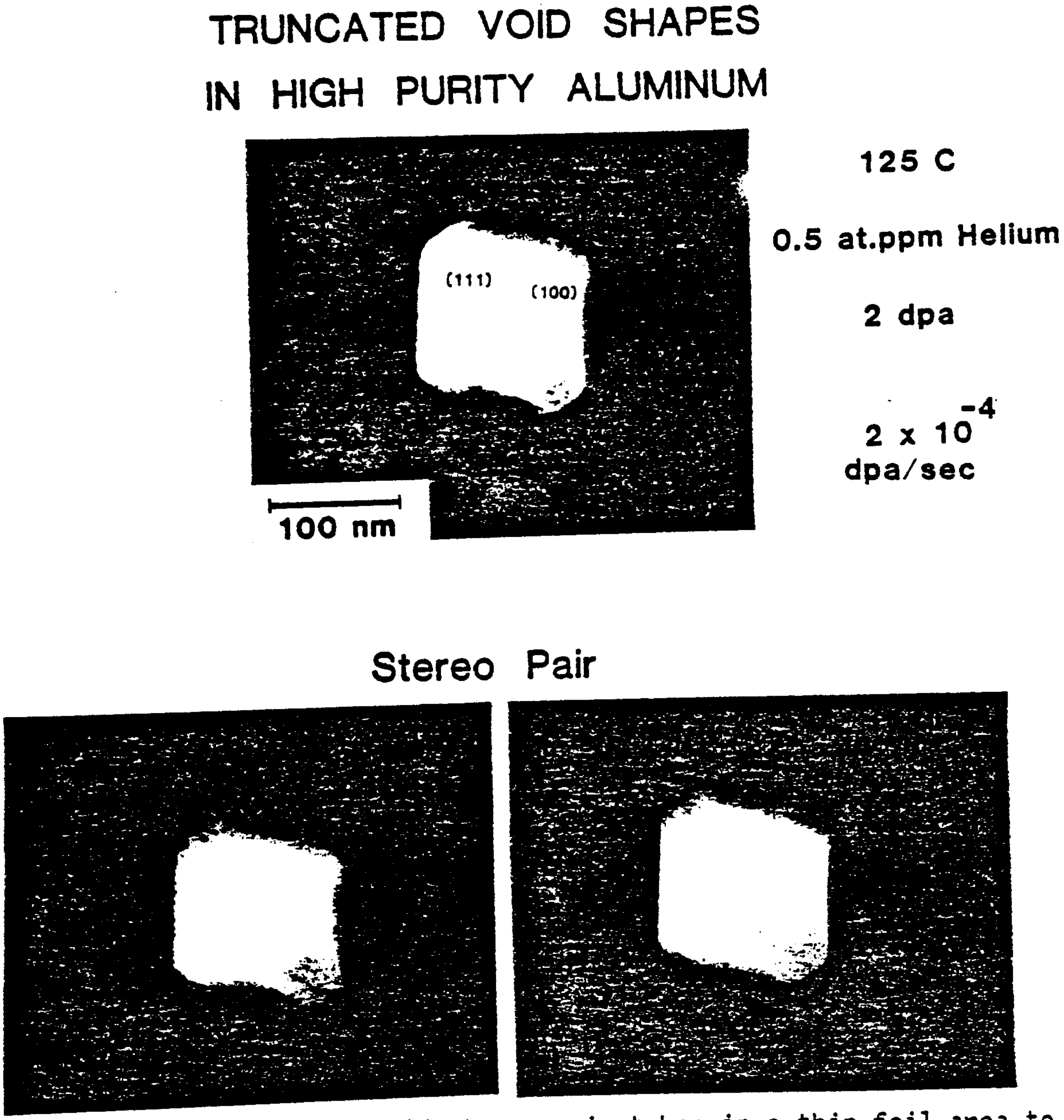

Figure 5.22 A truncated void stereo pair taken in a thin foil area to enhance the imaging of internal surfaces. The octahedral planes are (111) with the corner truncation planar to (100) and the octahedral edges corresponding to (110) planes.

VOID MORPHOLOGY AND SUPERVOIDS IN HIGH PURITY ALUMINUM

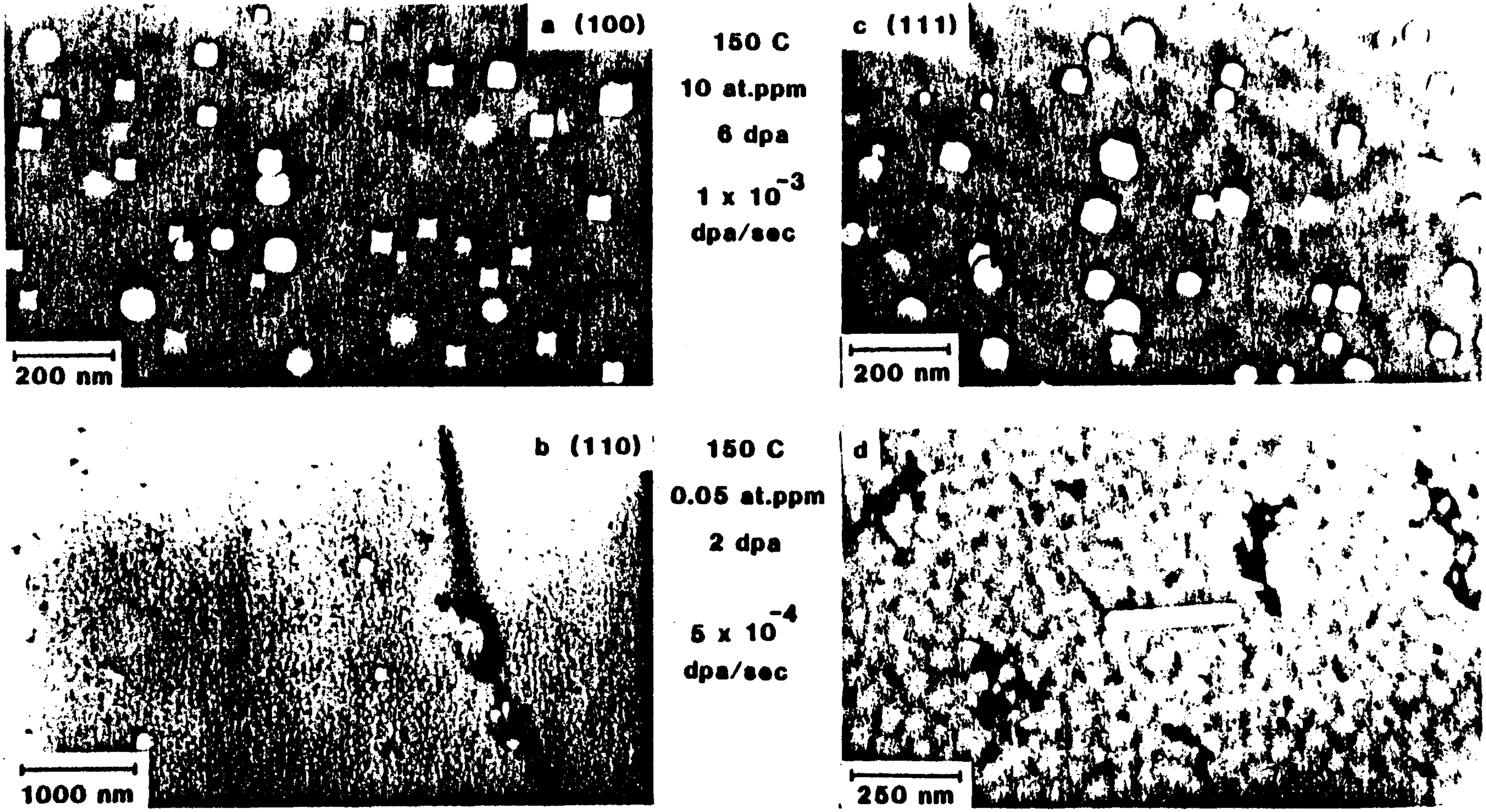

Figure 5.23 Elongated voids or Supervoids are shown for three beam directions ⟨100⟩, ⟨111⟩, and ⟨110⟩ with the ⟨100⟩ and ⟨112⟩ elongation directions indicated. The (100) foil also shows the void truncation traces (100) for the rounded voids.

restricted to a single family of directions but occurred for several different directions.

Elongation or supervoids have been associated with impurities[(2.22)] reducing the surface energy and assisting void growth. The elongation effect appeared at temperatures > 125°C and no precipitate or impurity effect could be identified, but the elongation was more prevalent in material that had not been surface polished after cold rolling and impurities from rolling may have been present. Supervoids have been observed in many neutron and ion irradiations of various levels of purity, and from the ultra-pure state of the aluminum it is difficult to establish a preciptate that can modify the end surface energy and make it grow. All of the samples that contained elongated voids had heterogeneous concentrations of voids and no estimates of the number density were made.

Void swelling has a moderate temperature effect from the bombardment studies and the swelling is plotted on a linear plot with temperature. The swelling is lower at 25°C and 150°C, and is greatly depressed at 100°C as well. The peak swelling temperature should occur at 0.4 T_m or 100°C in aluminum but very little swelling was observed. The 100°C sample was heavily investigated for the effect of dose on void size at 100°C and although there were voids in essentially all of the samples, the void population was quite small and always associated with grain boundaries or dislocation tangles. The swelling as a function of temperature is shown in Fig. 5.24 for the temperature range of 50°C to 150°C as open circles for the standard 2

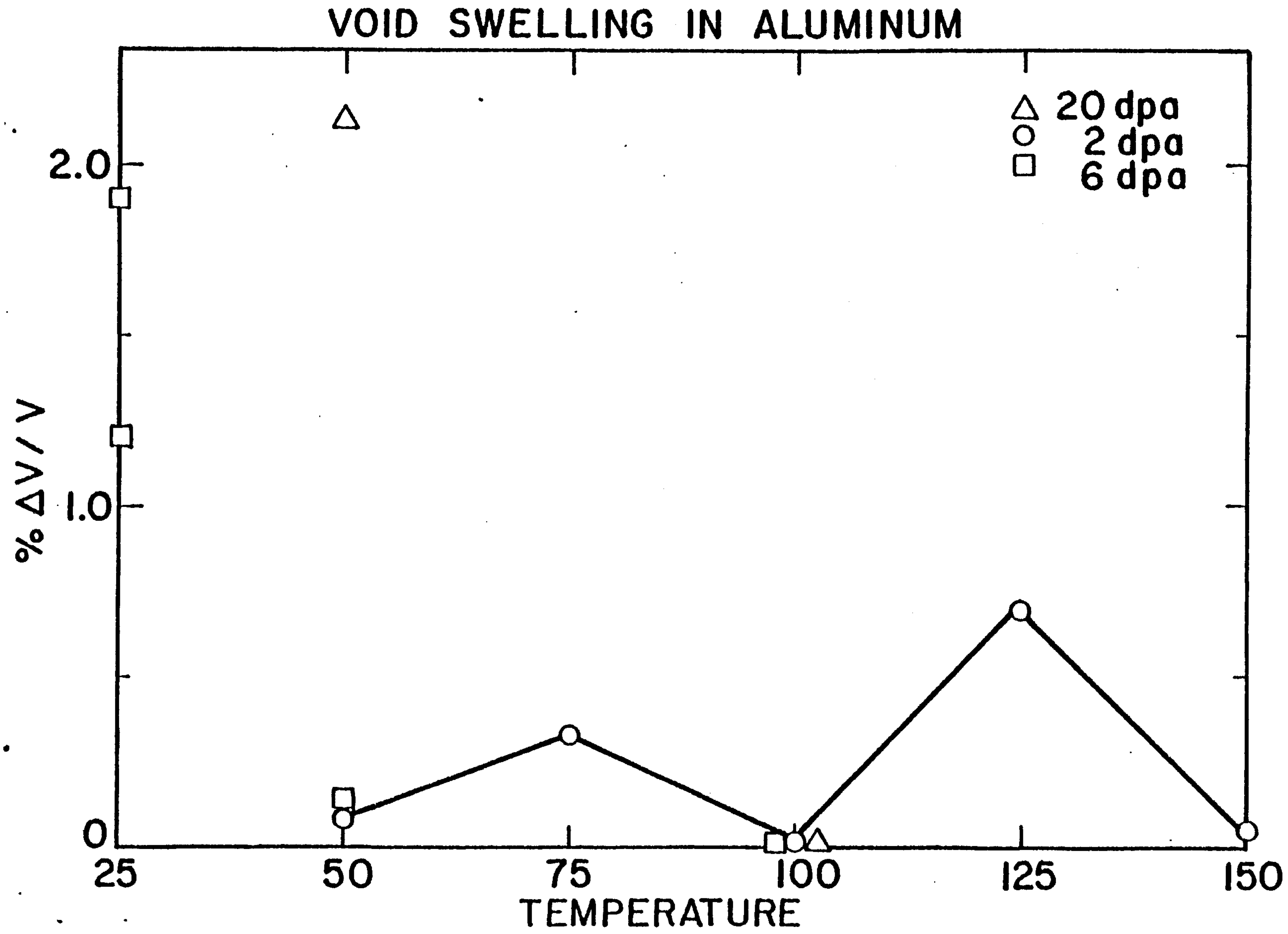

Figure 5.24 The temperature effect on void swelling in aluminum. A general suppression of swelling at 100C was consistently observed in all the samples bombarded at 100C. No explanation for the suppression of swelling at 100C is available at this time from theories or

dpa and other doses of 6 to 20 dpa are shown as squares and triangles.

C.3 Effect of Dose on Void Formation in Aluminum

The void swelling process in ion bombarded aluminum may be catagorized into three distinct time periods. First is an incubation time where nucleation is suppressed by transient microstructural evolution until the buildup of a vacancy supersaturation is sufficient to start the second phase of void nucleation. In the second phase, void nucleation increases with vacancy supersaturation, until the newly created voids become strong enough as a vacancy sink to reduce the vacancy supersaturation and end void nucleation, whereupon the third and final regime of void growth is entered. Void growth continues as long as vacancies are produced and a bias toward interstitials exists providing an excess of vacancies for the continued growth of voids.

Irradiations at 100°C did not produce homogeneous concentrations of voids so a number of bombardments at 50°C were done to assess the effect of dose level on the void formation. The number density decreased with fluence for this temperature where the displacement rates are comparable but the number density for the 5 dpa sample was much lower than either of the 2 dpa samples and 20 dpa samples. There are two factors that can account for the difference, dpa rate and helium concentration.

The lower displacement rate of the 5 dpa sample could have reduced the supersaturation level and produced the order of magnitude decrease in the nucleation number density observed in that sample. The effect of helium concentration also must be considered since the 2 dpa sample contains 1.0 appm of helium which is 10 times the amount in each of the 5 and 20 dpa samples. The most important factor was that the void concentrations in the 2 and 20 dpa samples was homogeneous while the 5 dpa sample contained scattered areas of voids. This difference suggested the 5 dpa sample nucleated voids heterogeneously suppressing the void number density for this sample. As a final point, the 5 dpa sample was the last sample irradiated in that particular "run." Since all of the samples share the same temperature, this sample had been held at 100°C for more than 7 hours and the 0.1 at.ppm of helium may have been significantly redistributed. Not only was the post-irradiation temperature important with regard to microstructure annealing, but the preirradiation temperature may have been important for the helium gas distribution as well.

The void size distribution for a number of samples is shown in Fig. 5.25 and shows the distribution of voids dispersed about an average size. The narrow distribution of void sizes in the 20 dpa historgram suggests that the void number density appeared to have reduced with fluence. A reduction in number density with dose requires a damage model in which a given number density is nucleated until the vacancy supersaturation ceased. A metal preinjected with helium would present a constant level of helium for nucleation while a neutron irradiation or dual beam irradiation has a time-dependent helium concentration. Time dependence of the helium will further

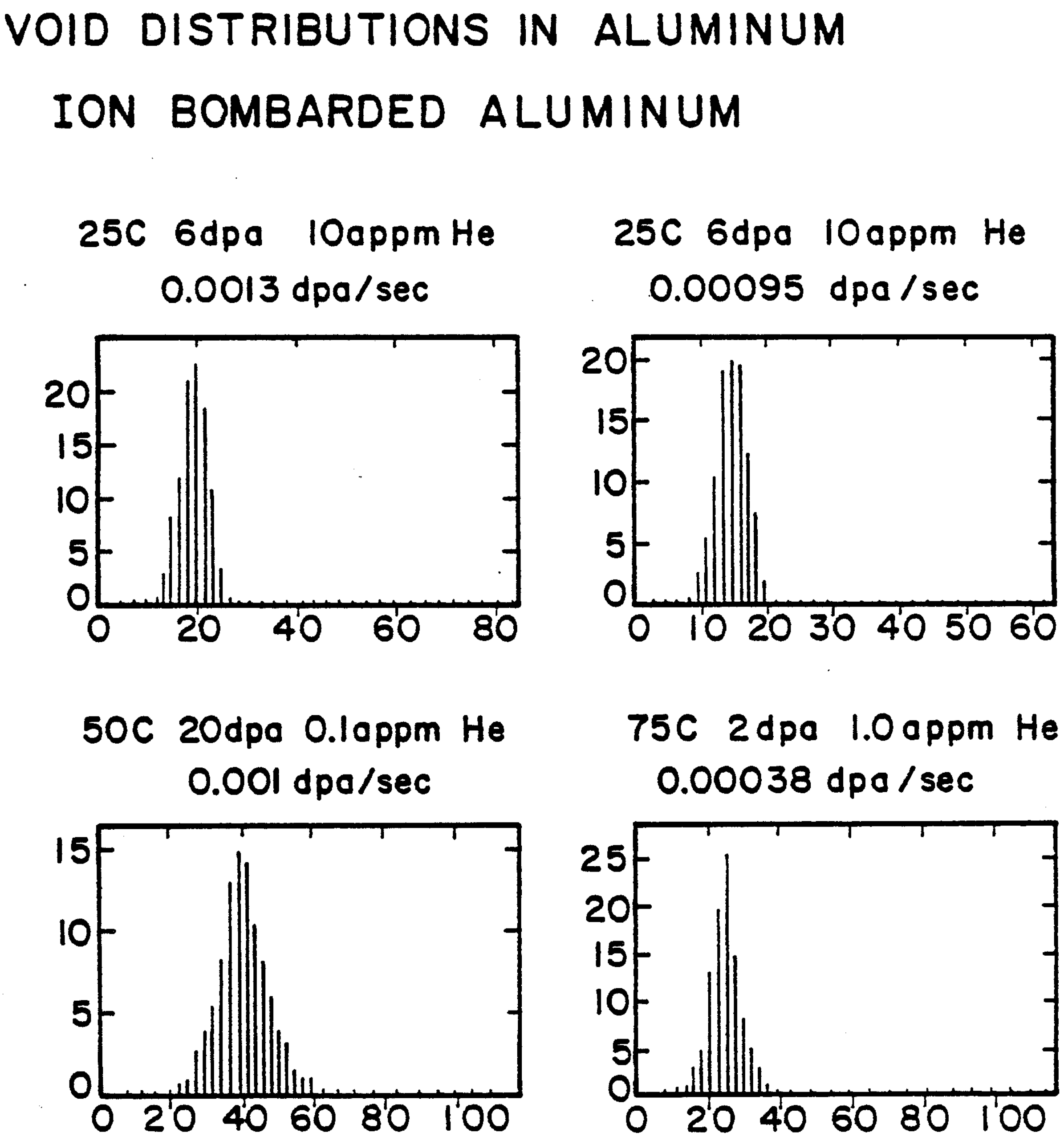

Fig. 5.25. Void histograms for several different temperatures showing the size distribution of the voids observed in aluminum ion bombarded aluminum containing helium.

complicate the void nucleation process but for preinjection, the population of voids would grow in size and some voids would be more favorably positioned and grow faster and at the expense of a less favorably placed void. Smaller voids emit vacancies at a higher rate than larger voids and the smaller voids will disappear if they receive a smaller percentage of the vacancies than larger voids. The declining nature of the void population is likened to a positive feedback loop where the stablizing effect of negative feedback is absent, the large voids are more likely to survive than the smaller voids and hence the smaller voids below a critical radius disappear.

The void size distribution for the ion bombarded aluminum was plotted as a function of temperature in Fig. 5.21 and as a function of dose at 100°C in Fig. 5.26. The 100°C irradiations produced heterogeneous concentrations of voids near grain boundaries and although the number density calculations were statistically insignificant, the void diameter was measured and a cube relationship with respect to the dpa dose was found. Average void sizes for four different fluences are listed in Table 5.4 and a plot of the number of vacancies, or atomic volume of the average void size, and the dose is shown in Fig. 5.26. The void volume was calculated as a spherical cavity where the number of lattice sites is $N = V/\omega$, ω is $((0.405)^3)/4$, and $V = 1.05\langle d\rangle^3$ for spherical cavities. A comparison with the fluence scan at 50°C shows the constant number density assumption used for calculating the void growth is valid for the 100°C irradiations. The voids are at fairly low densities around the

TABLE 5.4

Void Distribution Spreading in Aluminum with Dose

Dose (dpa)	Diameter (nm)	Width (FWHM) nm	Source
0.15	21	8.4	Packan
0.22	24	8.8	Packan
1.1	30	18.0	Packan
2.2	38	19.0	Packan
22.	50	36.0	Packan
0.4	20	11.	Adda
1.5	48	26.	Adda
3.2 Al^+	26	11.	Engman
8.0 Al^+	38	25.	Engman
16. Al^+	45	26.	Engman
2. Al^+	10	5.	This Study
20. Al^+	40	20.	This Study

CAVITY DIAMETER and CAVITY VOLUME

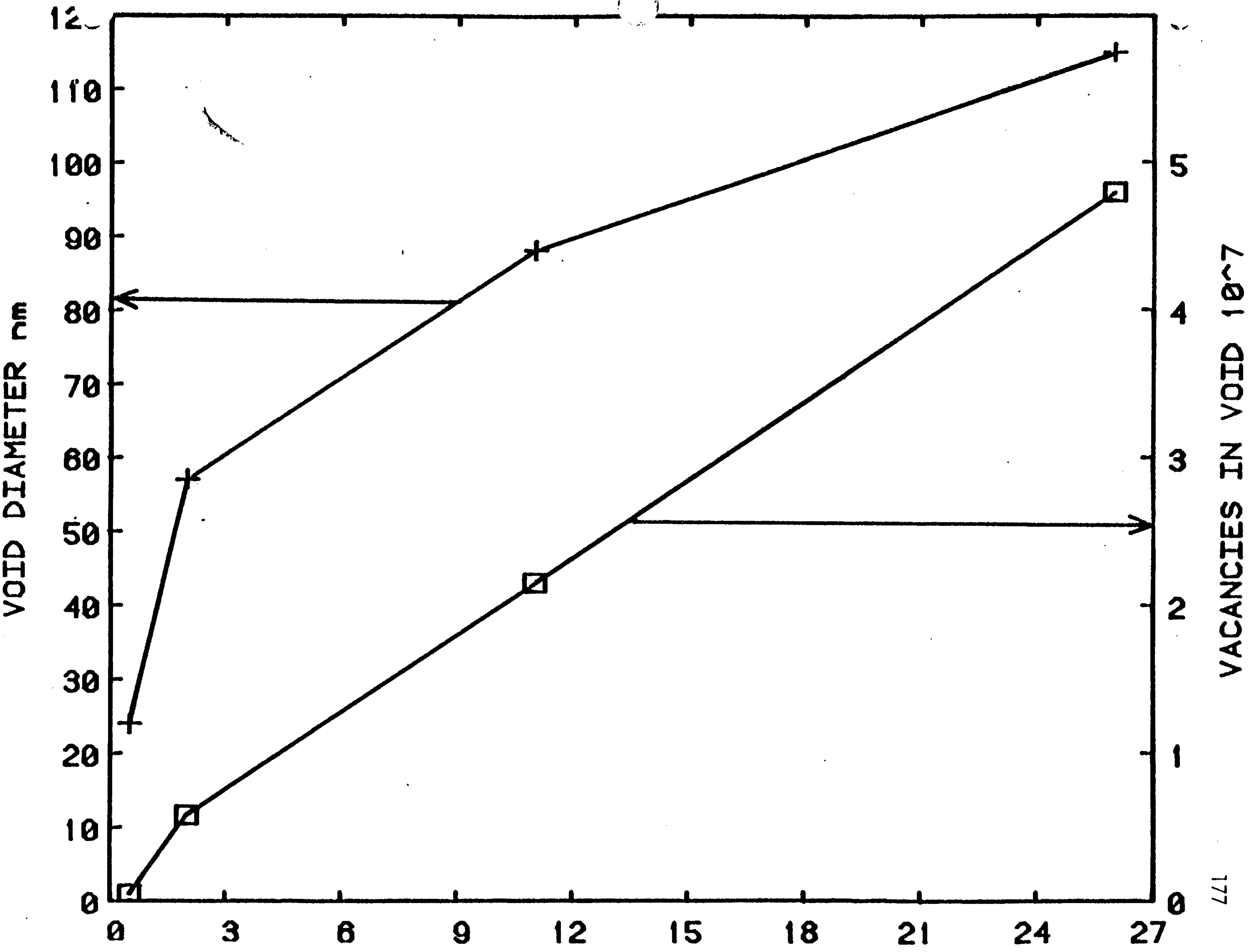

Figure 5.26 The void size and void volume as a function of dpa dose. The void size is indicated by the cross (+) symbol and the void volume by an open square. The void volume was calculated by assuming a

grain boundaries and the number of voids would be more stable than for a sample containing a higher number density where the shadowing of smaller voids would assist in their disappearance. The constant number density of voids at 100°C and the linear increase in volume provides linear swelling in aluminum at 100°C.

The growth of voids in a homogeneous distribution decreases the actual number density through elimination of smaller voids and increases the distribution width of the voids. The distribution of voids at 2 dpa and 20 dpa is shown in Fig. 5.25 where the average void diameter increased from 10 nm to 40 nm, the number density decreased for the 20 dpa sample from 12×10^{20} to 8.4×10^{20} voids/m^3. The broadening of the void distribution was observed in aluminum by Adda, et al.(2.33) and Stiegler(5.11) (using Packans's data). Adda and Stiegler reported an increase in void size distribution in high purity aluminum irradiated with neutrons. The full width at half maximum (FWHM) of the Adda aluminum, Packan(2.25) aluminum, and the ion irradiated aluminum from Engman(1.27) and this study is shown in Table 5.4.

C.4 Special Effects and Unusual Observations

A number of unexpected effects or special effects were observed in the aluminum bombarded aluminum experiments. The majority of samples containing homogeneous concentrations of voids also had voids aligned in long lines in some regions of the foils. Void redistribution from the homogeneous void distribution occurred during foil final thinning stress concentration and the formation of dipole loops and heterogeneous concentrations of dislocation loops were observed as well. Also, grain boundary motion and new void nucleation behind the advancing grain boundary were observed.

The long strings of voids were observed in most of the samples containing homogeneous concentrations of voids and are called void stringers or void walls. Void stringers as shown in Fig. 5.27 have a resemblence to line dislocations and it is postulated that helium gas atoms were trapped on a dislocation line and voids nucleated from these sources of helium gas. One half of Fig. 5.27 was imaged for dislocations and a line dislocation connecting a string of voids was not observed. The absence of such a connecting dislocation or parent dislocation after a total dose of several dpa is not suprising since the original dislocations would be extensively modified by climb from the interstitial and vacancy point defect flux and by damage from cascades.

Stiegler(5.11,5.12) reported void walls, or two-dimensional structures of voids in aluminum irradiated with neutrons while the void stringers observed in this study are distinctly one-dimensional lines as viewed from stereo microscopy and occur in "tangles" much like dislocation tangles. Turnbull(5.13) reported void strings in nuclear fuel materials and suggested the void strings were nucleated from the high concentration of vacancies in the collision cascade or fission track. The aluminum samples shown in Fig. 5.27 have their foil plane perpendicular to the bombarding ion beam and "ion tracks" or collision paths would appear on end from the foil plane normal.

VOID STRINGERS IN ALUMINUM

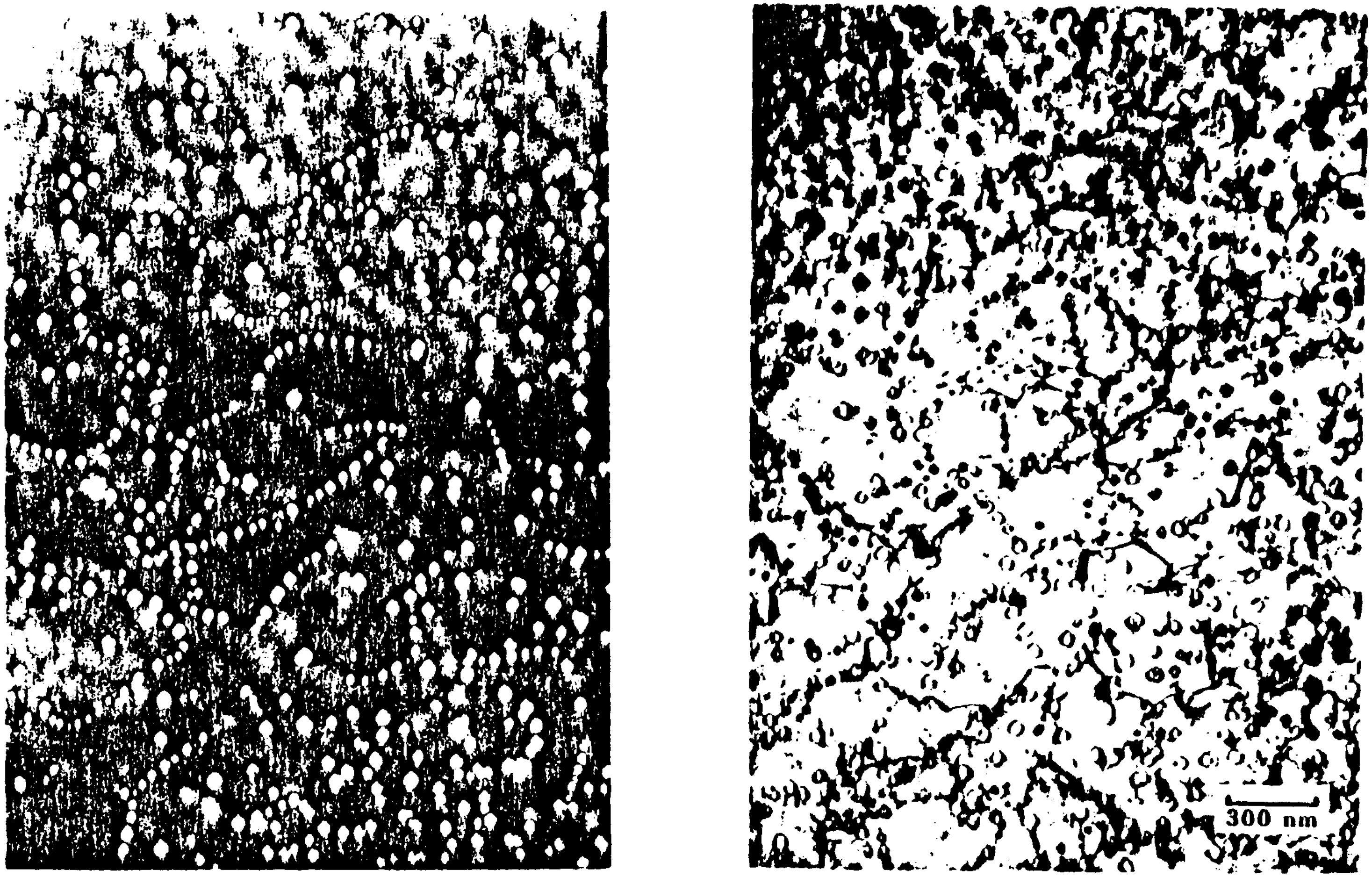

LOW CONTRAST

50°C 20 dpa

DISLOCATIONS IMAGED

0.1 at.ppm He

Figure 5.27 Void stringers in aluminum containing helium are shown for two different areas of a 20 dpa sample bombarded at 50C and containing 0.1 at.ppm of helium. The voids are imaged with low contrast and high contrast to image the dislocations. The dislocations are not aligned with the void stringers.

In addition, the void strings were curved and not straight lines as they would be for fission fragment tracks or heavy ions.

Two samples of aluminum containing 10 at.ppm of helium were bombarded with aluminum ions at 25°C to investigate the effect of pre-irradiation temperature on the formation of voids in aluminum. Two of the samples were identical except for their temperature history. The first sample was irradiated at 25°C and then all samples were heated to 100°C for about 7 hours and 50°C for 2 hours while other samples were irradiated, and finally returned to 25°C. The second matching sample had the same temperature history but was not irradiated until after the temperature cycle. The samples were nearly identical in void size, number density, and swelling but the formation of void stringers exisited only in the sample bombarded after the temperature excursion to 100°C. The first sample has a homogeneous concentration of voids with no observed stringers while the sample bombarded after the high temperature irradiations contained stringers. This observation supports the premise of mobile helium being trapped at dislocations and when the bombardment commenced, the trapped helium formed void stringers. All of the samples were at the same temperature during an irradiation and the experimental sequence of sample bombardments was to start with the highest temperature samples first and descend in temperature. The reason for descending in temperature was to eliminate or reduce the temperature annealing of the microstructures formed but the temperature history before the start of the irradiation was more important for the formation of void stringers than the temperature annealing of the microstructures. In fact, the number density and swelling of the sample bombarded before the temperature cycle to 100°C were higher than for the sample bombarded after the temperature cycle which indicated the loss of mobile helium to sinks reduced the swelling.

Void nucleation was influenced by grain boundaries by both suppressing void nucleation near the grain boundary (denuded boundaries) and assisting nucleation up to 4 μm away from the boundary. Voids formed at 100°C only in the vicinity of the grain boundary in those samples containing helium as discussed earlier. The formation of a denuded zone 20 to 40 nm wide is common in void containing materials and is due to the suppression of the point defect concentrations, with the grain boundary acting as a strong point defect sink, absorbing both vacancies and interstitials. Voids on the edge of the denuded zone appear larger than the average void size in the grain interior due to the smaller number of voids leading to fewer sinks for vacancies in the denuded region. In Fig. 5.28, three grain boundaries are seen and along boundary "A", larger voids in the edge of the denuded zone can be seen. The grain boundary at "B" and "C" in Fig. 5.28 moved in the direction of "A" during the bombardment where the denuded zone is larger on the receding side and smaller on the advancing side. The volume behind the receding grain boundary had a number of small voids which indicated void nucleation occurred as the boundary receded. Helium gas is required for nucleation and was present in material where a grain boundary has passed through.

MOVING GRAIN BOUNDARY IN ALUMINUM

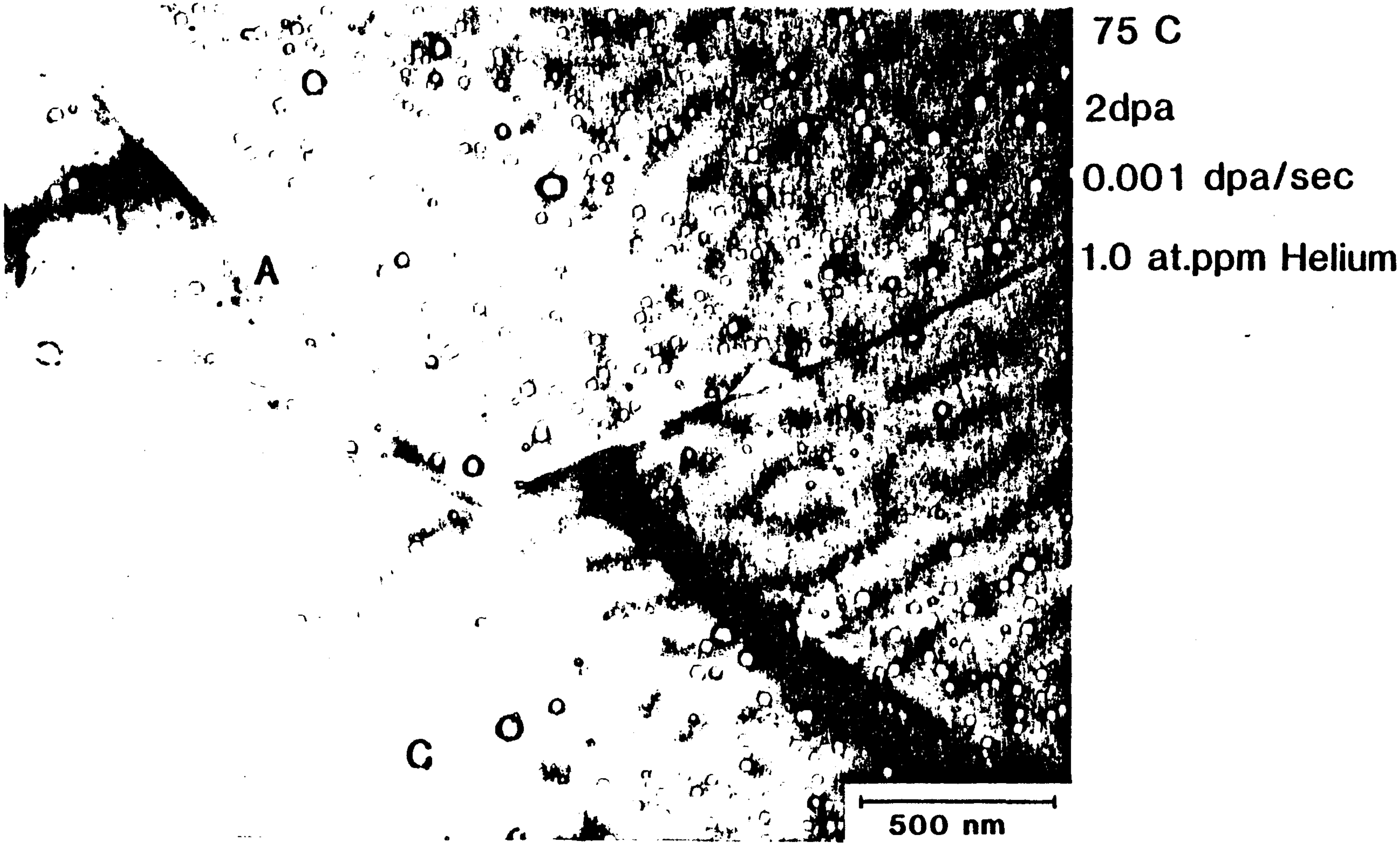

Figure 5.28 A triple grain micrograph of aluminum. The grain boundary at 'A' was stable and did not move while the boundaries at 'B' and 'C' were moving during the aluminum ion bombardment. New voids nucleated in the clean area behind the advancing grain boundary. Surface spalling from electropolishing produced "void like" images that have dark halos.

The helium gas was not absorbed by the grain boundary or was knocked into resolution by displacements near the grain boundary. Another possibility was that helium trapped by the growing voids was resolutioned from existing voids and was sufficiently mobile to assist new void nucleation.

Loop dipoles formed in aluminum containing voids as seen in Fig. 5.12. These loop dipoles are believed to be from foil stress concentration as discussed in Section B on dipole formation in pure aluminum containing helium. The stress concentration of bending forces could cause the shear loops to cross-slip and form the long loop dipoles as observed. All of the loop dipoles appear with the same elongation direction which would be expected for a stress induced cross-slip.

C.5 Comparison with Other Studies

A significant number of neutron studies have been completed using fast neutrons ($E > 0.1$ MeV) to irradiate pure aluminum and aluminum alloys. Two of the neutron studies by Packan and Risbet were thesis studies. The first, by Packan, used high purity aluminum irradiated with fast neutrons to study the influence of the accumulated dose on void formation. Ion irradiations from this study used the same material as used by Packan. The second, by Risbet, used pure aluminum and various alloys of aluminum containing trace amounts of alloy elements to several wt.% of alloy elements to study the influence of dose, temperature, and alloy elements on microstructural development. Both of these fluence studies produce the same result for high purity aluminum. The ion irradiations from this ion bombardment study are also plotted with the neutron data for comparison.

A plot of the neutron data for void swelling as a function of dpa dose and percent swelling is shown in Fig. 5.29 where the temperature dependence of swelling has been ignored. The majority of the data was performed in research type reactors at 55°C and a general observation shows the swelling of aluminum to be about 0.3% volume swelling per dpa. High purity aluminum used by Packan and Risbet show very similar results and the ion bombardments performed in this study compare reasonably well with the neutron data when normalized to dpa equivalents. Alloys of aluminum or the trace impurities in aluminum alter the sensitivity of swelling in aluminum by decreasing the swelling.

In comparison to neutron studies of swelling in stainless steel, the swelling sensitivity for the stainless steel alloys is bracketed by an upper limit of 1% volume swelling per dpa.(5.14) The effects of impurities and alloys in stainless steel studies was to suppress swelling or to produce an incubation dose for which little or no swelling is seen. As the irradiation progresses, the effect of the alloying agent responsible for the incubation was negated and the material begins to swell at the 1% per dpa rate. A similar case may be developed from an inspection of the log-log curve for swelling in aluminum where the upper limit of swelling is determined by the pure aluminum materials and the alloys of the aluminum have less commercial purity aluminum where the swelling was 0.15% for 10 dpa and

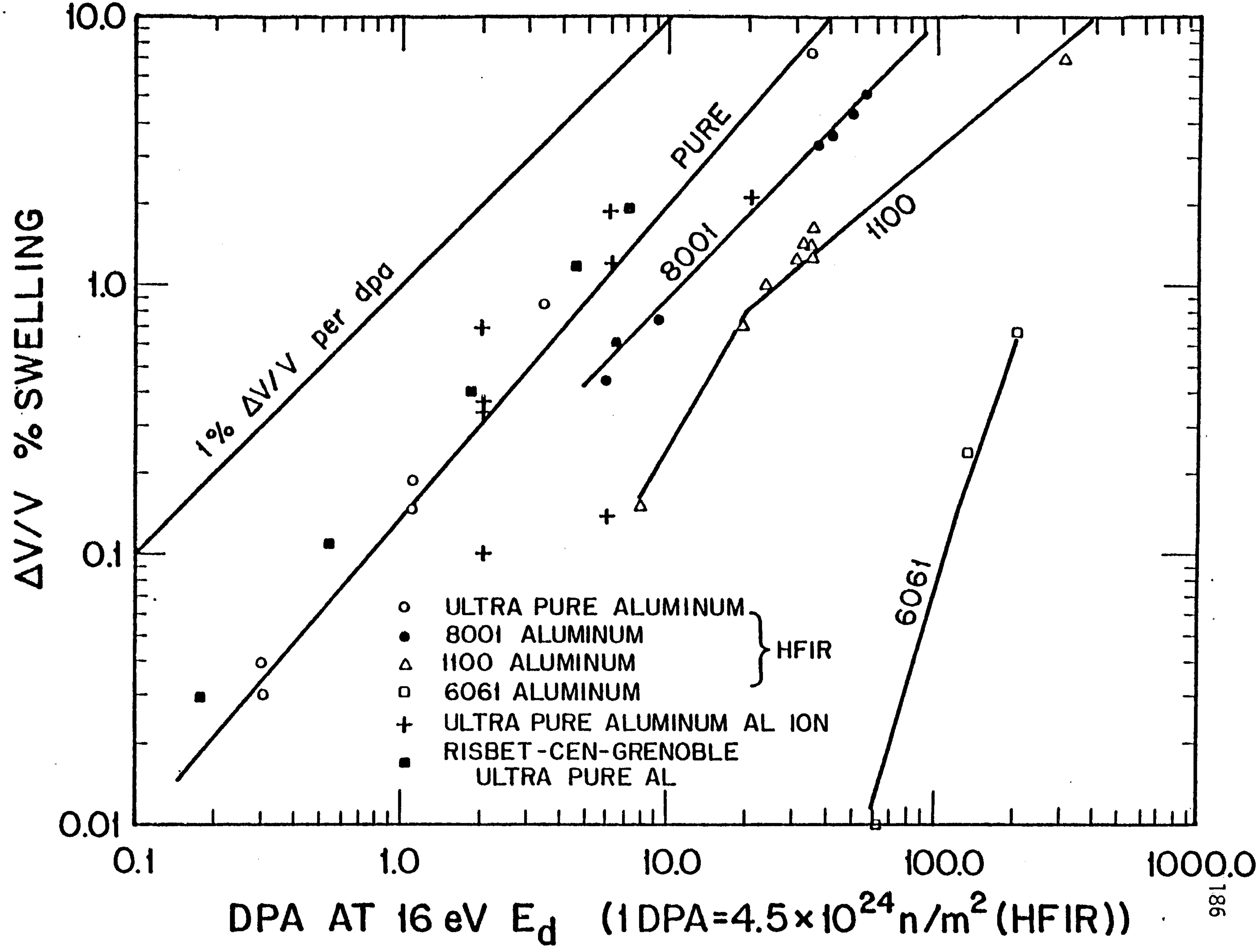

Fig. 5.29. A collection of dose studies of neutron irradiated aluminum showing the swelling and dose relationship. Several different temperatures are plotted with no correction for these different temperatures. The results from this study are included for comparison.

increased to 0.7% at 20 dpa. The rate of swelling then slowed to 7% for a total dose of 300 dpa showing a transition point at the 20 to 30 dpa region.

An age hardened alloy, 6061, shows the most resistance to void swelling when irradiated with neutrons with swelling of 0.7% after a total fluence of more than 200 dpa while having the steepest rate of swelling which would equal the commerical purity swelling at 400 dpa. These curves show impurities added to aluminum decrease the overall swelling in aluminum and with the exception of the 8001 alloy, the more impurity addition, the lower the swelling. Alloys of aluminum containing nickel swell at greater rates than commercial purity but still swell less than high purity aluminum.

A plot of the 1% swelling rate per dpa is included with the graph which is typical for stainless steels and note that aluminum alloys are typically an order of magnitude more resistant to swelling than stainless steels. Aluminum is more resistant to swelling than stainless steel but aluminum lacks high temperature properties which preclude its application in many cases.

While a number of neutron irradiated aluminum studies exist, only a few ion bombarded aluminum studies can be found. Experiments that covered a range of dpa displacements are plotted in Fig. 5.30 including this study. Temperature as a parameter is ignored in these plots and adds to the scatter in the data. Two values are plotted for the aluminum ion irradiations by Engman(5.15) using the displacement energy of 25 eV as used by Engman and 16 eV as for the rest of

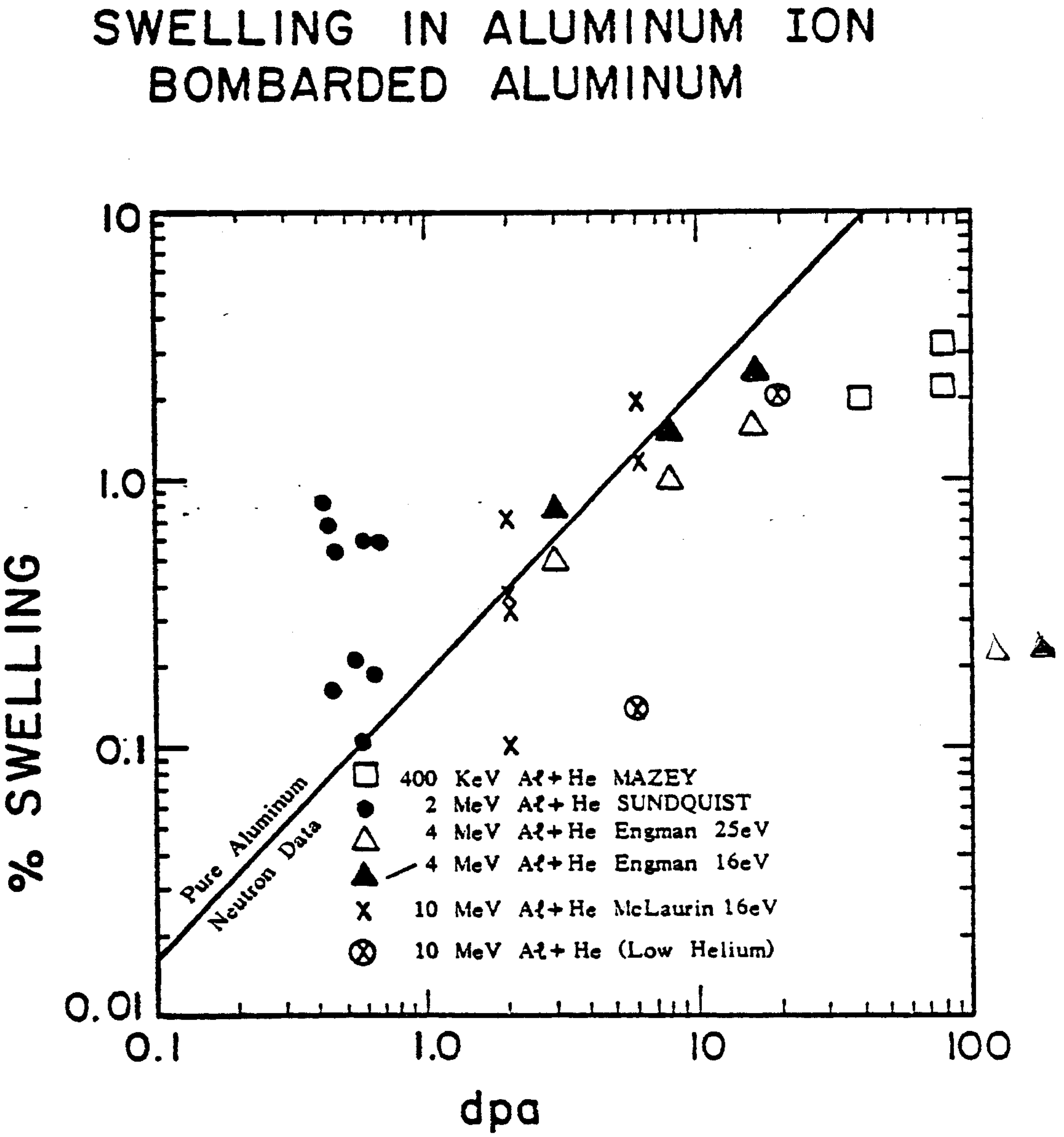

Fig. 5.30. A collection of dose studies of ion irradiated aluminum showing the dose and swelling relationship. No temperature corrections of dose rate effects have been added. The neutron swelling line is included for comparison.

the data. Ion bombardment experiments show more scatter and less of a straight log-log dependence on dpa level. The solid line indicates the pure aluminum neutron irradiated data and the data from this study and the 16 eV Engman data lie relatively close to the neutron data. Sundquist performed aluminum ion bombardments at low dose levels and low bombarding ion energy which may be responsible for the increased swelling above the neutron base line. On the other side, Mazey et al. used lower energy aluminum ions to produce higher levels of damage and obtained lower levels of swelling than the neutron base line data shows. Two of the data points used in this stydy had very low levels of helium and this may be a factor in reducing the overall swelling.

In general, the ion bombardments in this study agree with the swelling observations of both aluminum ion bombardments and neutron irradiations. The agreement is better with neutron data than it is with the aluminum ion bombardment data. Neutron data shows less scatter than the equivalent aluminum ion bombardment data and it may be the lack of precise ion data measurements that affect the ion bombardment results than a fundamental radiation damage effect.

REFERENCES FOR CHAPTER 5

5.1 J.B. Whitley, *Depth Dependent Damage in Heavy - Ion Irradiated Nickel*, Phd. Thesis University of Wisconsin (1978), p. 165-175.

5.2 ASM Committee on Material Composition and Phase Diagrams, *Phase Diagrams of Binary Alloy Systems*, Vol. 9, p. 259. (The concentration was extended by $C = C_o \exp(-H_s/kT)$ and fitting to the data from the diagram. $C_o = 6.7\ 10^{-20}$ J, $H_s = 9.6\ 10^6$ at.ppm)

5.3 Peter Wilkes, *Solid State Theory in Metallurgy*, Cambridge University Press (1973), London, p. 229.

5.4 R.A. Dodd, personal communication (June 1982).

5.5 D.I. Potter, "Ion-Bombardment-Induced Instabilities in Ordered Precipitates", in Phase Stability During Irradiation, eds. Holland, Mansur, and Potter, American Institute of Mining, Metallurgical, and Petroleum Engineers (1981), p. 537.

5.6 A. Risbet and V. Levy, "Origin of Vacancy Loops Observed in Pure and Impure Aluminum Irradiated by Fast Neutrons," Phil. Mag. *31* (May 1975) pp. 975-983 (French).

5.7 R.K. Ham, "On the Loss of Dislocations During the Preparation of a Thin Film," Phil. Mag. *7* (1962) p. 1177.

5.8 K.H. Westmacott, R.S. Barnes, D. Hull and R.E. Smallman, "Vacancy Trapping in Quenched Aluminum Alloys," Phil. Mag. *6* (1961) pp. 929-935.

5.9 K.S. Liu, O. Kawano and Y. Murakami, "Structural Changes in Age-Hardenable Aluminum Alloys Induced by Low Temperature Neutron Irradiation," Rad. Eff. *15* (1972) pp. 37-49.

5.10 D.W. Pashley and A.E.B. Presland, "The Movement of Dislocations During the Observation of Metal Films Inside an Electron Microscope," Phil. Mag. *7* (1962) p. 1407.

5.11 J.O. Stiegler, "Void Formation in Neutron-Irradiated Metals," in *Radiation Induced Voids in Metals*, p. 318, op.cit. Ref. 1.6.

5.12 J.O. Stiegler, "High-Fluence Neutron-Irradiation Damage in Aluminum," IAEA-SM-120/F-5, (1970) p. 219.

5.13 J.A. Turnbull, J. Nucl. Mat. *38*, p. 206.

CHAPTER 6: SUMMARY OF RADIATION DAMAGE IN HIGH PURITY ALUMINUM

The primary objectives for this study were:

(1) to confirm and extend the previous results of self ion damage in aluminum to higher doses, broader temperature range, and helium concentrations;

(2) to study the effect of a copper ion beam on high purity aluminum;

(3) to verify the requirement of helium for void formation in high purity aluminum.

Two parts of this thesis project were to design and build an irradiation sample holder for maintaining a constant temperature by heating or cooling and assemble electropolishing equipment for sample preparation. Experiments conducted on this equipment lead to the following observations and conclusions.

(1) A copper ion beam produces heterogeneous dislocation loops and <100> orientated θ-like precipitates.

(2) All dislocation loops analyzed in aluminum irradiated with copper ions or aluminum ions were essentially all vacancy.

(3) Dislocation movement is present in aluminum during TEM analysis.

(4) Foil preparation after ion bombardment and prior to TEM analysis modifies the existing microstructure.

(5) Void and dislocation formation in aluminum is often heterogeneous for aluminum ion irradiations.

(6) Hetergeneous concentrations of voids are common in aluminum and appear as void stringers.

(7) Helium is required to form voids in high purity aluminum.

(8) Helium concentration is not a major factor on void formation in concentations of 0.1 to 10 at.ppm.

(9) The swelling of aluminum at 100°C is very low.

(10) The temperature effect of swelling in aluminum shows the number density to decrease with increasing temperature and the void size to increase with increasing temperature which follows the conventional void nucleation and growth theories.

(11) Temperatures in the range of 125°C to 150°C produced void truncation and elongated or supervoids.

(12) This study shows swelling values that agree with other self-ion bombardment experiments, although the ion data is very scattered when compared to the neutron data.

(13) Ion induced swelling of aluminum compares with neutron irradiated swelling for pure aluminum.

(14) The swelling rate of aluminum as a function of dpa dose for all temperatures is one-third the swelling rate of stainless steels for the same dpa dose.

(15) Electron irradiations of aluminum do not produce the same types of damage microstructures as observed in ion irradiations.